# Rapid Disease Monitoring with Resistive-Pulse Sensing in Nanopipettes

by

Lauren Matthews

A thesis submitted to the University of Birmingham for the degree of

Doctor of Philosophy

School of Chemistry

College of Engineering and Physical Sciences

University of Birmingham

December 2024

# ABSTRACT

Periodontitis, also known as gum disease, is a common inflammatory condition that affects the supporting tissues of the teeth. Without treatment, irreversible damage and tooth loss can occur. The disease can also have a larger impact beyond oral health, such as increasing certain cancer risks and reported links to diabetes. Current diagnostic techniques are qualitative and retrospective, unable to identify biomarkers from the underlying disease processes. There is a growing need for a rapid, quantitative, multiplexed and non-invasive method for effective diagnosis and disease monitoring. One such approach is resistive pulse sensing with nanopores, a single molecule technique with low sample volume requirements. Combined with DNA carriers, containing probe molecules which introduce chemical specificity for target analytes, protein detection and identification is possible. However, analysing complex translocation events requires optimised data analysis workflows, and an understanding of nanopipette transport properties.

In this thesis, sources of noise interference were identified and mitigated in the nanopore set-up, to enable high bandwidth measurements at 100 kHz and above. The effect of the optimisation process was assessed using the root-mean-squared (RMS) noise and the power spectral density of the signal, with alternative equipment and grounding points evaluated. Replacing mains power equipment with battery-powered alternatives, alongside filtering the mains power were unavoidable, were found to be the most effective strategies for reducing noise. Overall, measurement bandwidth was increased from 10 kHz to 100 kHz, with an 82% reduction in RMS noise observed.

The integration of antibodies with DNA carrier structure using the sterically controlled nuclease enhanced DNA assembly method was investigated, to allow for multiplexed assay with greater target analyte applicability. The impact of DNA conjugation to antibodies was determined with a titration enzyme-linked immunosorbent assay method, with only a small decrease in binding ability observed. A 3kbp antibody-DNA conjugate was synthesised, and the structure confirmed with gel electrophoresis imaging. However, attempts to isolate the structure and maintain antibody functionality were unsuccessful.

To aid with interpretation of DNA carrier translocation and assess the suitability of current data analysis methods for high bandwidth measurements, a reference dataset of 4 kbp dsDNA translocation was established. Noise and translocation events were able to be separated temporally, despite low signal-to-noise ratio, and event clustering algorithms distinguished linear and folded DNA conformations. Translocation was seen in both forward and reverse directions, with characteristics following the expected trends, explained by established theoretical models in the literature.

Finally, the focus of this thesis shifted to chemical analysis of the interior sensing region of nanopipettes. A sample preparation method was developed by improving the electrical conductivity with carbon coating, allowing for high resolution imaging with scanning electron microscopy. The interior surface of the nanopipette channel was successfully exposed with focused ion beam milling. Model systems, modified quartz slides, were tested with energy dispersive X-ray spectroscopy (EDX), time-of-flight secondary ion mass spectrometry (ToF-SIMS) and Auger electron spectroscopy (AES), before applying these methods to nanopipette samples. For chemical analysis of nanopipettes, monolayer detection is below the limit of detection for EDX, whilst ToF-SIMS lacked the necessary lateral resolution. AES showed the most promise owing to excellent lateral and depth resolution, but further sample preparation was found to be necessary for charge mitigation purposes.

# ACKNOWLEDGMENTS

There are many people I must thank, professionally and personally, for their immense help in completing this work.

First, I owe much thanks to my supervisors, Prof. Tim Albrecht, Dr. Melissa Grant and Dr.-Ing Vasile-Dan Hodoroaba, for all their guidance and support throughout this project, of which I am extremely grateful.

Many thanks, also, to the different research groups I have found myself in, including the Albrecht Group, BAM Division 6.1, and BAM Division 5.1. Of my BAM colleagues, I am particularly indebted to Leonardo Agudo-Jacome, René Hesse, Mario Sahre, Robert Schusterbauer and Thorid Lange, for sharing their expertise and assisting with my experimental work.

I am also grateful to Oliver Irving and Nashwa Awais, for their support as patient office mates and sincere friends. Thanks to Oliver, my lab-buddy, for cheering me up. And thanks to Nashwa, my procrastination partner, for stressing me out. Without their help, this thesis would never have been finished.

Lastly, I'd like to mention my friends and family for their endless support and encouragement throughout. I couldn't have done this without my mam, Annette, and my stepdad, Paul, who saw this work started but did not get to see it finished. This is dedicated to them.

# CONTENTS

# LIST OF ILLUSTRATIONS

# LIST OF TABLES

# LIST OF EQUATIONS

2.1 $$I_{RMS} = \sqrt{\frac{\sum_i^n (I_i - \bar{I})^2}{n}}$$

Equation for RMS noise, where $I_{RMS}$ is the noise in the current signal, $I_i$ is the current for datapoint $i$, $\bar{I}$ is the average current value and $n$ is the total number of datapoints.

3.1 $$S(L_t) = (S_{max} - S_{min}) \cdot \frac{(K_D + R_t + L_t) - \sqrt{(K_D + R_t + L_t)^2 - 4 \cdot R_t \cdot L_t}}{2 \cdot R_t} + S_{min} + B \cdot L_t$$

Correlates the ELISA signal intensity ($S(L_t)$) with the concentration of added ligand ($L_t$). The titration curve is characterised by five parameters: the dissociation constant ($K_D$), concentration of immobilised receptor ($R_t$), maximum and minimum absorbance signal ($S_{max}$ and $S_{min}$) and finally the slope of the background signal ($B$).

4.1 $$P(t) = \frac{L}{\sqrt{4Dt^3}} \cdot e^{-\frac{(L-vt)^2}{4Dt}}$$

The equation for translocation event time distribution $P(t)$, where $L$ is the contour length of the DNA, $D$ is the diffusion coefficient of DNA inside the pore channel, $v$ is speed and $t$ is time.

4.2 $$d_{pore} = \frac{4Gl + \frac{\pi}{2}GD_i}{D_i\pi g(c) - \frac{\pi}{2}G}$$

Relating conductance and pore diameter, $d_{pore}$, where $G$ is conductance of the nanopipette, $l$ the taper length, $D_i$ the inner diameter of the quartz capillary, and $g(c)$ the conductivity of the electrolyte solution.

4.3 $$J = \frac{\pi d^2 \mu}{4L_P} \cdot V_{bias} \cdot c$$

Equation for translocation frequency of events, $J$ is flux, $d$ is the pore diameter, $\mu$ the free-solution electrophoretic mobility of DNA, $L_P$ the length of the pore channel, $V_{bias}$ the applied voltage bias and $c$ the DNA concentration in solution.

4.4 $$\tau \approx \frac{L}{\mu E} \approx \frac{LL_P}{\mu V_{bias}}$$

Relationship of dwell time with bias, where $\tau$ is dwell time of long DNA, $L$ is DNA contour length, $\mu$ the electrophoretic mobility of DNA in the pore, $E$ the local electric field, $L_P$ the channel length of the pore and $V_{bias}$ the applied bias.

# LIST OF ABBREVIATIONS

| | |
|---|---|
| AD | Analogue-to-digital |
| AdoMet | S-adenosyl-L-methionine |
| AES | Auger electron spectroscopy |
| B&W | Binding and washing |
| BSE | Backscattered electron |
| DBCO | Dibenzocyclooctyne |
| DMSO | Dimethyl sulfoxide |
| dsDNA | Double-stranded DNA |
| EDX/EDS | Energy dispersive X-ray spectroscopy |
| ELISA | Enzyme linked immunosorbent assay |
| Fab | Variable region |
| Fc | Constant region |
| FFT | Fast Fourier transform |
| FIB | Focussed ion beam |
| FWHM | Full width half maximum |
| GAMM | Gibson assembly master mix |
| GCF | Gingival crevicular fluid |
| HGF | Hepatocyte growth factor |
| HPLC | High-performance liquid chromatography |
| ICR | Ion current rectification |
| kbp | Kilobasepair |
| $K_D$ | Dissociation constant |
| M.Taq1 | Methyl transferase enzyme from *Thermus Aquaticus* |
| MMP-8 | Matrix metalloproteinase-8 |
| MMP-9 | Matrix metalloproteinase-9 |
| MS | Mass spectrometry |
| MTase | methyltransferase |
| MWCO | Molecular weight cut-off |
| NHS | N-Hydroxysuccinimide |
| PBS | Phosphate buffer solution |

| | |
|---|---|
| PCR | Polymerase chain reaction |
| PE | Primary electron |
| PK | Pyruvate kinase |
| PSD | Power spectral density |
| RMS | Root-mean-squared |
| S100A8 | S100 calcium binding protein A8 |
| SAM | S-adenosyl-L-methionine |
| SCoNE | Sterically controlled nuclease enhanced |
| SE | Secondary electron |
| SEM | Scanning electron microscopy |
| SNR | Signal-to-noise ratio |
| ssDNA | Single-stranded DNA |
| TE | Tris-EDTA |
| TEM | Transmission electron microscopy |
| ToF-SIMS | Time-of-flight secondary ion mass spectrometry |
| α1-AGP | Alpha-1 acid glycoprotein |

# 1 INTRODUCTION

## CONTENTS

# 1.1 INTRODUCTION

## 1.1.1 PERIODONTITIS

Periodontitis, more commonly known as gum disease, is an inflammatory condition that affects the periodontium, the tissues which support and anchor teeth. This disease initially presents as milder gingivitis, as plaque on the teeth accumulates and causes the gums to become inflamed. If left untreated, the disease progresses to affect deeper periodontal structures, leading to tissue degradation, tooth mobility, and eventual tooth loss.[1–3] There is evidence that periodontitis has a broader impact on the overall health of patients, as bacteria from diseased sites enter the blood stream, causing low levels of inflammation which can spread throughout the body.[3] This can lead to increased risks of developing or exacerbating serious diseases, such as diabetes,[4–6] cardiovascular disease,[6,7] and rheumatoid arthritis.[8–10] Suspected interactions have also been reported with over 50 conditions, including Alzheimer's disease[11] and certain cancers,[12,13] owing to the systemic inflammatory burden of severe periodontitis.[3] Gingivitis and early periodontitis are often asymptomatic, with a positive diagnosis and treatment issued only after significant tissue damage has occurred. The irreversible nature of this damage, alongside the additional health risks, highlights the need for early and accurate diagnostic methods.

Standard clinical diagnostic methods include periodontal probing and radiographic imaging. Both techniques have inherent limitations.[1,14,15] Probing depth measurements of the gums are quick, cheap and simple, but are subject to clinician discretion and lack reproducibility. X-ray scans are largely retrospective; they are used to identify irreversible damage to the bone structure, neglecting information from the soft tissues. This technique, therefore, fails to provide insights into the underlying biochemical changes and ongoing inflammatory processes at the active disease sites. Additionally, as a tool for disease monitoring, X-ray scans are limited by radiation safety guidelines. To improve diagnostic and disease monitoring capabilities, a minimally invasive diagnostic technique utilising biomarker detection is necessary.

**Biomarkers in Periodontitis: Gingival Crevicular Fluid as a Diagnostic Medium**

Molecular biomarkers are biological molecules (such as proteins, nucleic acids, or metabolites) found in blood, saliva, other body fluids or tissues, that can be measured objectively to identify pathological processes. Gingival crevicular fluid (GCF) accumulates in the periodontal pocket, between the gums and teeth, and is an easily accessible source of these biomarkers for

periodontitis (Figure 1.1). Proteomic and metabolomic analysis of GCF has identified a wide range of possible biomarkers, such as pro-inflammatory cytokines, enzymes and microbial metabolites.[16–18] The molecular composition of GCF has been found to vary over the course of disease progression.[19] Therefore, accurate analysis of GCF in periodontitis patients could allow for early diagnosis, in addition to monitoring of disease progression and treatment response.

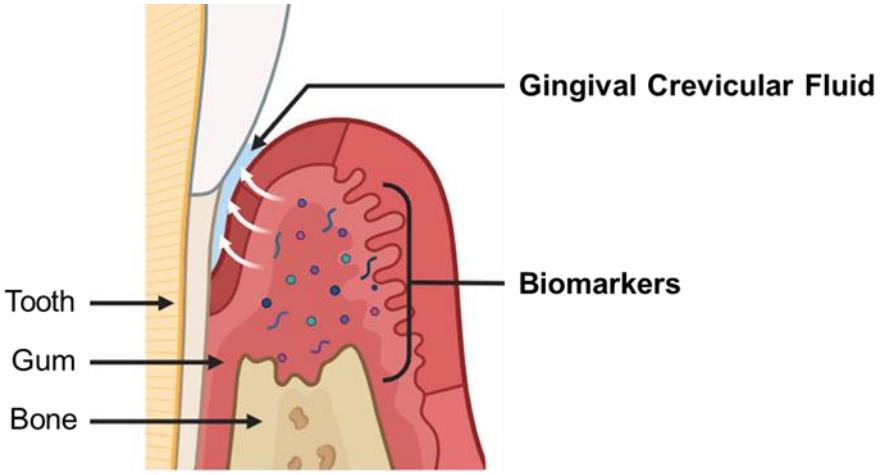


*Figure 1.1: Illustration of the source of gingival crevicular fluid (GCF), located in the periodontal pocket and derived from the periodontal tissues. GCF is a complex mixture of biomarkers and other substances, containing serum, tissue breakdown products, inflammatory mediators, antibodies, enzymes, protein peptides and microorganisms.*[19]

Despite the potential, quantitative detection of specific and potentially low concentration biomarkers within complex biological fluids remains challenging. Conventional techniques, such as enzyme-linked immunosorbent assays (ELISAs), do provide the necessary sensitivity and specificity, but are severely limited in clinical applications due to their time-intensive workflows, substantial sample volume requirements, and limited capacity for multiplexed analysis. ELISA requires multiple wells for multiplexed analysis with 100 µL of prepared sample required per well; the available sample volume of GCF is well below this (typically a few microlitres per hour),[19] and sample dilution to increase volume would reduce the necessary sensitivity. Nanotechnologies and single-molecule techniques are being investigated as alternatives, aiming to provide high-throughput, multiplexed assay with minimal sample requirements.[21]

### 1.1.2 Nanopores and Resistive Pulse Sensing

Applying a voltage bias across two electrodes in an electrolyte solution causes an ion current to flow. This leads to potential drops and localised electric fields within the setup. A nanopore has a pore diameter typically between 1 – 100 nm. When such a nanopore is placed between the two electrodes, it restricts the ion flow, causing the electric field lines to converge near the pore. This intense electric field can drive charged analytes in solution through the nanopore. As the analyte excludes volume, and hence ions, a detectable modulation of the ionic current results. This is termed a translocation event, and forms the basis of resistive pulse sensing.[22]

The charged analytes of most interest to the bioanalytical community are biomolecules. Already, the nanopore sensing technique has demonstrated its ability for diagnostic applications and genomic studies,[23–25] having been successfully applied in commercially available genome sequencing devices.[26] They are used to analyse a wide array of biomolecules, such as RNA,[27–29] proteins,[30–33] nanoparticles,[34–36] and DNA nanostructures.[37,38]

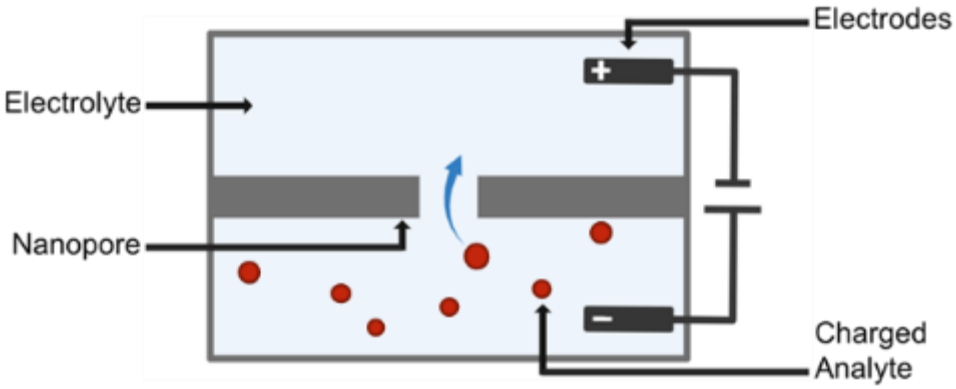


*Figure 1.2: Diagram of a nanopore sensor, not including the detection and measurement equipment.*

**Classes of Nanopores**

Different applications of nanopore sensing require different types of nanopore, depending on the analyte, medium and intended longevity. Nanopores can be tailored to their intended applications with unique characteristics, fabrication methods and materials compositions. The three classes of nanopore that will be discussed here are biological nanopores, solid-state (or chip-based) nanopores, and nanopipettes (Figure 1.3).

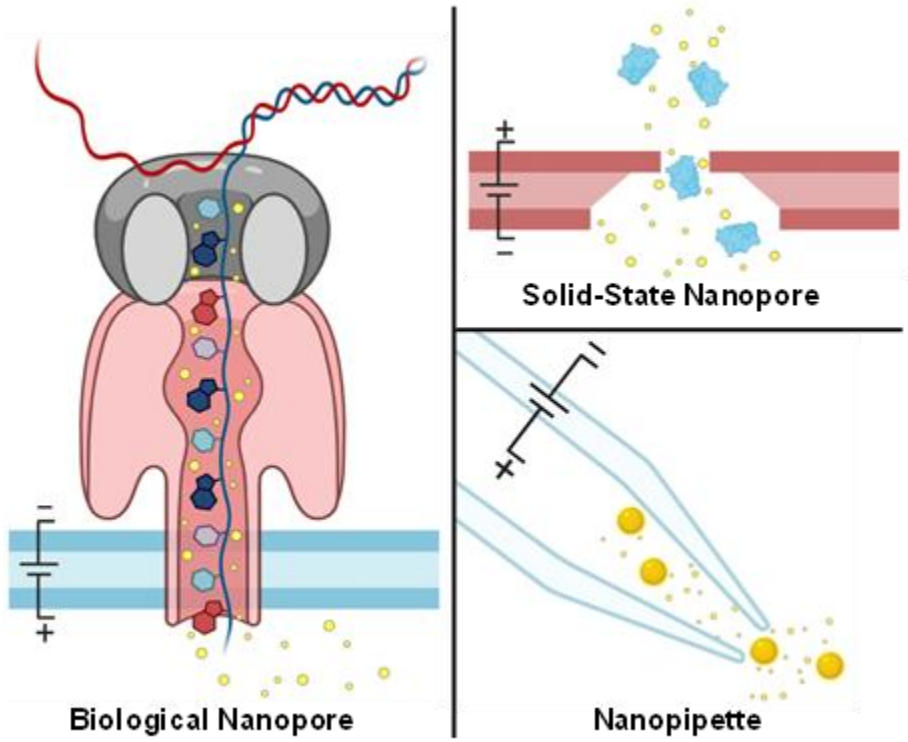


*Figure 1.3: Illustration of each of the three classes of nanopore: a biological nanopore contained in a lipid bilayer, a solid-state nanopore drilled into a silicon chip substrate, and a glass nanopipette.*

**Biological Nanopores**

Biological nanopores have precise physical dimensions, with pore sizes typically between 1 – 4 nm. This is both an advantage and disadvantage, as it restricts applicability to a range of analytes. Controlling the number and position of these pores in lipid bilayers can also be difficult.[39,40]

Biological nanopores are typically formed by self-assembling proteins that embed into lipid bilayers. They form highly reproducible structures, demonstrating excellent stability over a range of experimental conditions. These nanopores typically have the lowest levels of intrinsic noise, as the lipid bilayer capacitance is usually low. This allows for highly sensitive, high bandwidth measurements. Biological nanopores can also be further modified, with site-specific mutagenesis. This introduces additional functional features, such as molecular binding sites, or mechanisms to exert greater control over analyte translocation.[39,41]

An example of a well-studied biological nanopore is α-hemolysin, which has a pore diameter of 1.4 nm at its narrowest point. Nanopores of such small dimensions can be difficult to fabricate with other classes of nanopore. Translocation studies of single-stranded DNA (ssDNA) with α-hemolysin have been reported, but larger analytes such as double-stranded DNA (dsDNA) cannot translocate, having a diameter of approximately 2 nm.[42,43]

**Solid-State Nanopores**

Solid-state (or chip-based) nanopores are fabricated from inorganic or polymeric materials. Silicon nitride is commonly used for the pore membrane, owing to its high resistivity, thermal stability, mechanical robustness, and excellent dielectric properties.[22] These nanopores are more adaptable and can be tuned for a broad range of experimental conditions. The nanopore membranes are usually supported silicon, glass or Pyrex substrates.[44–46]

Whilst the intrinsic noise of these nanopores is typically higher than their biological counterparts, hybrid solid-state structures have reduced device capacitance to below 1 pF.[45] Stacking silicon nitride substrates with glass membranes, for instance, reduces capacitance and enables high-bandwidth measurements.[44,47]

Solid-state nanopores have greater flexibility, as techniques with nanoscale precision, such as transmission electron microscopy (TEM) and focused ion beam (FIB) milling, are used for fabrication. These methods are used to drill holes into the membranes, producing pore diameters below 10 nm.[48] However, these techniques require clean-room facilities and have limited scalability.[48,49]

**Nanopipettes**

Nanopipettes are fabricated with laser-assisted mechanical pulling of quartz or borosilicate capillaries, typically yielding pore sizes between 5 – 50 nm. These materials offer favourable wetting properties and excellent dielectric characteristics. In comparison to the other classes of nanopores discussed, nanopipettes require little in the way of equipment or expertise to produce. Their fabrication methods are relatively inexpensive and straightforward.[22]

However, it is inherently difficult to precisely control the pore size and channel length of nanopipettes. These properties are important, as they define the sensing region and determine the transport properties of analytes in nanopipettes. Furthermore, reproducibility is challenging

for sub-20 nm pipettes. To achieve smaller pore diameters, there is a compromise between pore size and taper length, which can affect the spatiotemporal resolution of the sensor.

Nanopipettes are often utilised for rapid and precise biochemical sensing. However, these applications require highly selective and sensitive detection of analytes in complex media and environments. To address this, chemical functionalisation of the nanopipette surface has been explored, as a way to enhance the intrinsic capabilities of the sensor.

### 1.1.3 Chemical Modification of Nanopipettes

Functionalisation has been used to tune nanopipettes for biosensing and ion-transport studies. Chemical modifications can introduce specificity and selectivity for target analytes, from small molecules[50–52] to more complex biomolecules, such as proteins.[53,54] More complex modifications can be achieved by attaching target-specific probes to the inner surface, such as aptamers.[51–53,55] Aptamers are oligonucleotides that fold into structures with high specificity for target proteins, and can remain stable in a range of non-biological conditions. Such probes can undergo conformational changes upon specific binding to target analytes, resulting in detectable and distinguishable changes to the ion current.

Simple chemical functionalisation of nanopipettes utilised chemical conjugation with surface hydroxyl groups. Silanisation reactions can introduce functional groups suitable for further reactions, such as amine or carboxyl groups, to which aptamer probes can be covalently attached. For example, modification with dopamine-specific aptamers has achieved sensitive detection in the nanomolar to picomolar range through ion current rectification (ICR) mechanisms.[51]

At low electrolyte concentrations, nanopipettes can exhibit ICR. This is a non-linear response to an applied symmetric voltage, owing to the asymmetric geometry of the nanopipette channel. Changes in the ICR response are indicative of changes in surface charge, a result of successful functionalisation. ICR is used in the literature to confirm the outcome of functionalisation reactions. For example, aptamers were attached to nanopipettes, using silanisation to first introduce amine functional groups, followed by thiol-maleimide click chemistry of the thiolated aptamers. ICR measurements were successfully used to characterise changes in nanopipette response at each stage.[57]

As the complexity of surface modifications increase, so too does the challenge of characterising the inner surface of the non-conductive substrates. Electron microscopy techniques, such as SEM and TEM, can be used for characterisation of nanopipette geometry, but struggle to achieve the necessary resolution to image ultra-small nanopipettes (with pore diameters below 20 nm).[58] Detailed chemical characterisation is currently out of reach, but will be necessary to ensure reproducible sensor performance.

Nanopipettes functionalised with aptamers combine nanoscale confinement with chemical specificity, allowing for selective and sensitive detection of neurotransmitters, such as dopamine and serotonin. They demonstrate good performance in complex biological environments associated with neuroscience applications and diagnostics.[53–55] In addition, a study by Denuga *et al.* demonstrated the reusability of these sensors. When washed with hot deionised water, the initial probe-only state of the nanopipette was restored and verified with ICR.[56] However, when sensing in complex media, functionalised nanopipettes can be prone to biofouling and irreversible binding, limiting some sensors to single-use applications.[55] Furthermore, using a single nanopipette in ICR measurements limits detection to a single-target.

For many diagnostic applications, detection of multiple target analytes is required. To achieve multiplexed assay whilst maintaining chemical specificity requires more than chemical functionalisation of the nanopipette surface. In addition, detecting and identifying an array of biomarkers remains difficult, as they can be similarly sized, globular proteins.[59–61] Resistive pulse sensing of proteins with nanopipettes does not provide the necessary chemical information. As such, an alternative approach to introduce chemical selectivity before translocation is necessary.

### 1.1.4 Multiplexed Assays with DNA Carriers

Instead of functionalising the sensor, some studies have focussed on functionalising the analyte. Using DNA carriers, analyte targets can be selectively bound and identified within complex mixtures.[30,33,62–64] Engineered DNA nanostructures are designed and synthesised to include probe molecules or specific binding sites, and they act to ‘carry’ the target analytes through the nanopore, allowing for multiplexed detection.[33,62]

Bell and Keyser have previously demonstrated the potential for multiplexed assay of various proteins with this approach.[30,33,62] They designed a library of DNA carriers, each with an

analyte-specific binding site and an identification barcode. The barcodes were composed of hairpin junctions distributed along the DNA strand, with the presence or absence of a hairpin representing a binary '1' or '0', respectively. Nanopore analysis enabled the accurate decoding of these barcodes with 94% accuracy, once unsuitable translocation events (such as folded DNA) were filtered from the data. Each barcode corresponded to a unique binding site further along the carrier, enabling analyte identification and chemical selectivity. Using this system, the authors detected four different antibodies by their interaction with antigens conjugated to the DNA carriers. The nanopore technique discerned bound versus unbound probes with over 90% efficiency.[33]

At sub-saturation concentrations of the target analyte, the proportion of bound signals ('positives') provides a quantitative measure of analyte concentration. Kong et al. explored this by incubating selectively-binding DNA carriers with varying concentrations of target proteins.[61] Using biotin-streptavidin and digoxigenin-antidigoxigenin pairings, binding curves were constructed for analyte concentrations ranging from 0–5.6 nM and 0–31 nM, respectively. The resulting nanopore data closely matched theoretical predictions based on dissociation constants derived from standard assay methods.[62]

The molecular weight difference between the bound and unbound states significantly influences detection accuracy.[62] When recording the 'height' of translocation events relative to the open channel current, antidigoxigenin (150 kDa) produced a larger signal-to-noise ratio (SNR) when bound to its target, and hence a 'taller' translocation event, than streptavidin (52.8 kDa). This improved SNR facilitated higher detection efficiency. However, false positives were observed in both cases. The authors suggested that shortening the DNA carriers or increasing their rigidity could reduce the occurrence of folded translocations and lower the number of false positives.[62]

Biotin-streptavidin interactions are frequently studied in nanopore experiments due to their strong non-covalent binding under a wide range of conditions, including high-salt environments.[30,62,65,66] To enhance SNR and slow analyte translocation, experiments often use 4 M LiCl.[67,68] However, these high-salt conditions, while improving resolution, can destabilise specific biomolecular interactions and promote protein unfolding. Reducing salt concentrations may stabilise binding but introduces a trade-off by decreasing sensing resolution.

### 1.1.5 Design and Synthesis of DNA Carriers

While nanopores are relatively low-cost to produce, the cost of synthesising specifically engineered DNA carriers increases significantly, especially when designing DNA strands base-pair by base-pair.[30,62,69] For multiplexed sensing, costs increase with the number of target analytes, as typically one carrier is required for each analyte.[30,33,62,69] However, DNA carriers capable of incorporating multiple analyte probes can be synthesised using established DNA engineering methods.

Probe placement along the DNA strand is critical for distinguishing signals. Studies of resistive-pulse sensing resolution suggest spatial uncertainties of 130–330 base pairs, assuming constant DNA velocity during translocation.[70] However, long DNA molecules translocate at variable speeds, with speed increasing as translocation progresses.[71] As such, spatial uncertainties near the molecule's entry point are estimated at 200 bp, decreasing to approximately 90 bp beyond the midpoint of the DNA strand.[70] Resolving features as distinct peaks may require spacing of probes over 200 bp apart, depending on the nanopore's sensing region.[71]

DNA strands translocate with equal probability of either end entering the pore first.[22] As such, distinguishing probe orientation is necessary for carriers containing multiple different probe molecules. Hairpin structures, which generate large, distinct signal peaks, can be used to determine the orientation of the DNA carrier.[30,33] Alternatively, spatial patterns in probe arrangement could provide this information. For carriers with identical probes, distinguishing the specific probes (and hence the target analyte) on the DNA strand is more important than orientation. Features such as 3-bit barcodes using hairpins or differently sized proteins can help with identification.[30,33]

Synthesis of DNA carriers typically relies on DNA self-assembly[30,33,62,69,70] or enzymatic modification,[71–74] with newer techniques like Sterically Controlled Nuclease Enhanced (SCoNE) DNA assembly [75] combining their strengths (Figure 1.4). Other approaches, such as nick translation and triple helix formation, are not as widely used within the field of nanopore sensing but can also be used to synthesise or modify DNA carriers.[76-79]

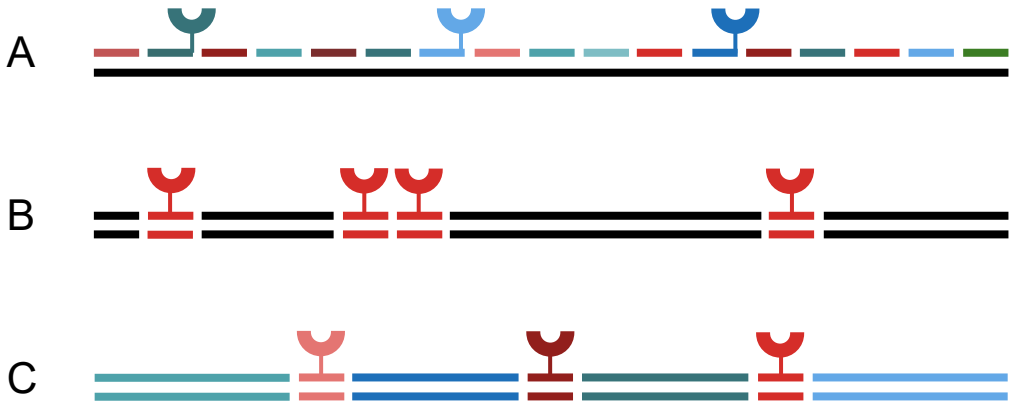


*Figure 1.4: Illustration of the DNA-probe structures that can be achieved with each assembly/modification method. A) DNA self-assembly uses linearised single-stranded DNA as a template for complimentary oligonucleotide staples, each of which can be modified to contain the desired target-probe. B) Enzymatic modification uses a methyl transferase enzyme to transfer functional groups at sequence-specific recognition sites, which can react further to incorporate a specific target-probe. C) SCoNE DNA assembly requires spacer and probe DNA strands with complementary ends, using Gibson assembly to build the full structure, with the ability to include different probe-targets in a specific and targeted manner.*

**DNA Self-Assembly**

This technique first linearises circular ssDNA with a restriction enzyme, and then uses the resulting ssDNA strand as a template. Complementary oligonucleotides bind specifically to the ssDNA strand, and as such is hybridised to dsDNA.[69,70] Oligonucleotides can be specifically designed to form overhangs,[69,70] hairpins,[30,33] or include antibody probes,[30,33] and these features can be distinguished during resistive-pulse sensing.[30,33,69,70]

With this method, multiple probes can be incorporated along the DNA strand. For example, a study demonstrated the attachment of hairpins and antigen probes to the ssDNA scaffold m13mp18. To fully hybridize the scaffold's 7228 bases, 190 designed oligonucleotides were used in excess to ensure proper positioning and assembly.[33,70]

**Enzymatic Modification**

Enzymatic modification relies on DNA methyltransferase (MTase) enzymes and the methyl donor S-adenosyl-L-methionine (AdoMet or SAM).[73] Modified AdoMet analogs can enable transfer of functional groups, such as amine, azide, or alkyne, onto DNA strands for further

chemical reactions like click chemistry.[71–74] This technique is frequently used to fluorescently label DNA at specific sites for identification.[80-82] For example, a 'DNA fluorocode' technique was developed using the MTase enzyme M.HhaI to direct fluorescent labels to specific 5'-GCGC-3' sequences, producing high-resolution, single-molecule optical maps. This approach achieved a labelling density of approximately one site every 500 base pairs and a resolution of less than 20 bases.[80]

The efficiency and versatility of fluorescent DNA labelling techniques, following enzymatic modification, have been documented in the literature.[81] Common coupling techniques include copper-catalysed azide-alkyne cycloaddition, amine-NHS ester coupling, and strain-promoted azide-alkyne cycloaddition. It was found that copper-catalysed azide-alkyne cycloaddition gave a reasonable yield but resulted in some structural DNA damage. By contrast, strain-promoted azide-alkyne cycloaddition provided the highest labelling efficiency whilst preserving DNA integrity.[81]

Enzymatic methods are particularly suited for creating DNA carriers with a single type of probe.[72–74] However, the placement of probes depends on the sequence-specific recognition sites of MTase enzymes. When using naturally occurring DNA fragments, such as m13mp18, probe placement is determined by the location of recognition sequences. If the spacings between these probe placement sites are insufficient, resistive-pulse sensing can fail to resolve them, as observed by Chen et al.[71] For precise positioning of probes, custom dsDNA scaffolds must be designed.

**SCoNE DNA Assembly**

The SCoNE DNA assembly method utilises both DNA self-assembly and enzymatic modification processes.[75] Two types of dsDNA strand are required for this technique. Probe strands are short dsDNA strands that are enzymatically modified to introduce functional groups for click-chemistry, in order to attach the probe molecules. Spacer strands are longer strands of non-functionalised dsDNA, that ensure there is enough distance between probe molecules to resolve them with nanopore sensing. Probe and spacer strands are then joined together using Gibson assembly, to build the full DNA carrier.[75]

Gibson assembly is a method that allows for the joining of multiple blunt-ended DNA fragments with overlapping 3' sequences, typically in a single reaction.[83] The method can accommodate

DNA fragments of varying lengths and sequences without the need for enzyme restriction sites. Three enzymes are utilised; 5' exonuclease, DNA polymerase and DNA ligase. The 5' exonuclease removes the 5' ends of the DNA fragments, and the overlapping 3' overhangs of adjacent DNA fragments anneal. The DNA polymerase incorporates nucleotides to fill any remaining gaps, and the DNA ligase covalently joins the fragments and seals any nicks in the DNA.[83]

This assembly method aims to address several challenges associated with synthesis of multiplexing DNA carriers. However, further method development is required to assess its applicability with a range of probe molecules.

**Additional Functionalisation Strategies**

Nick translation allows for site-specific labelling or modification of long DNA. It is an enzymatic technique and utilises DNA polymerase to simultaneously degrade and replace nucleotides at single-strand nicks.[84] If nucleotides labelled with fluorescent dyes, radioactive isotopes, or biotin are provided, these will be incorporated into the DNA and results in large, evenly labelled probes. The main limitation of this method is the requirement for DNase I to create the nicks, which can be introduced at random sites and lead to non-specific labelling.[84] An example of this technique in nanopore research involved labelling ultralong genomic DNA (>300 kbp) with fluorophores via nick translation.[76] This enabled optical detection and real-time tracking of the DNA molecules as they were stretched, captured, and threaded through nanopores for combined optical and electrical sensing.[76]

Another approach is triple helix formation, which introduces a third strand of DNA that binds to dsDNA site-specifically. This interaction occurs only at homopurine-rich target sequences, via Hoogsteen or reverse Hoogsteen hydrogen bonding (forming A-T-A or C-G-C triplets).[85] In nanopore applications, triple helix formation enables selective and reversible binding.[77-79] Triple-helix molecular switches have been used to detect specific biomarkers for Alzheimer's disease,[77] breast cancer,[78] and SARS-COV-2,[79] by generating distinct current signatures in biological nanopores. The binding of a triple helix is sensitive to pH and salt concentration, which could affect stability and performance under standard sensing conditions for solid-state nanopores.[77-79]

### 1.1.6 Analysing Translocation Events

For the full realisation of multiplexed assay, successful analysis of complex DNA carrier translocation events is necessary. For reliable data interpretation, the molecule must translocate linearly, so that the structural motifs on the DNA strand can be detected in the signal and matched to the expected structure (Figure 1.5)

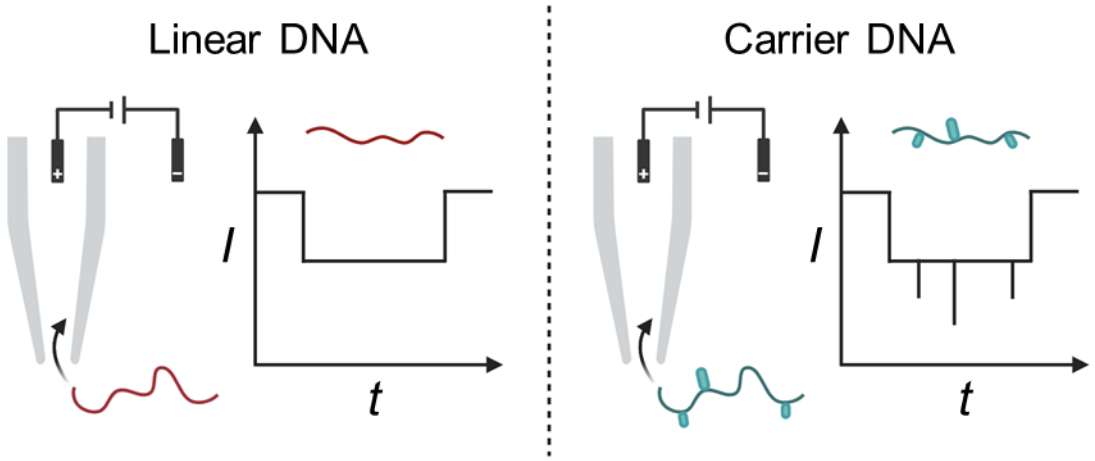


*Figure 1.5: Diagram showing the resulting I(t) traces from the translocation of linear DNA (red) and a modified DNA structure (blue).*

The raw data generated from nanopore experiments, in the form of current-time (*I(t)*) traces, requires signal processing to determine key translocation characteristics, such as current modulation ($\Delta I$), translocation time ($\tau$), event charge deficit ($q_e$) and standard deviation of the baseline signal ($\sigma$). This usually relies on custom-written software for data acquisition, instrument control, and subsequent analysis.[33,69,86]

**Translocation of Complex DNA Carriers**

A straightforward approach was demonstrated by Loh et al., whereby they first evaluated the occurrence of DNA folding or knotting during translocation of unmodified DNA strands. They reported that knotting occurred in only 3.1% of events and, therefore, did not exclude these from their analysis. However, for one DNA carrier strand studied (sample hyx1), only 2% of recorded translocation events corresponded to the carrier strand (1,166 events out of 59,964).[69]

Custom MATLAB code was used to process *I(t)* traces. After performing background correction, translocation events were identified using a 5$\sigma$ noise threshold, with event start and stop times determined by a 1$\sigma$ threshold. For each event, the median current between the relative translocation durations of 0.2 and 0.8 was set as the event current baseline. Regions surpassing

a 1.2$\Delta I_e$ cut-off were identified as subevents, with their start and stop points determined relative to the baseline. By normalising subevent characteristics against the corresponding event characteristics, the study found that normalised current modulation provided the clearest distinction between bound and unbound states.[69]

Other studies adopt a different methodology, focusing first on noise reduction and filtering to leave only full-length, unfolded DNA events for further analysis. Regions where the signal noise exceeded a defined threshold (e.g., 25 pA) were removed, followed by an event search. Nanopores the produced results with broad $\tau$ distributions were excluded, and the $q_e$ of qualifying events were calculated. Only data within a Gaussian-fitted region around the mean $q_e$ was retained, to eliminate events caused by DNA fragments. Events corresponding to folded DNA were removed by analysing the first 10% of the translocation trace. These filtering steps excluded approximately 85% of the recorded events, significantly refining the dataset for analysis.[33]

To assign barcodes and determine probe identities, these studies required further signal processing. After filtering and cropping *I(t)* traces to isolate the translocation event, baseline correction was performed. An algorithm counted the number of peaks in the trace, and cross-checked whether the result matched the expected designs of the DNA carriers. Unassigned barcodes—often arising from complex DNA folding—were either discarded or matched to the best approximation.[33]

**Challenges in Signal Analysis**

Despite extensive data acquisition, only a fraction of the data corresponds to translocation events. Further data extraction and refinement is often required, to remove anomalous results or folded DNA events. As such, the number useable translocation events remaining for analysis is usually a small percentage of the original data. Fortunately, translocation events are fast (millisecond timescales) and relatively frequent, so long data collection periods are not strictly necessary.[33] However, these studies highlight the importance of algorithms and signal processing workflows in order to extract meaningful data, which is further complicated when analysing complex signals from DNA carriers.

## 1.2 PROJECT AIMS

The goal of this project is to enable the multiplexed detection of periodontitis biomarkers for disease diagnosis and monitoring, by utilising specific DNA carriers and resistive pulse sensing (Figure 1.6). This method aims to detect a range of periodontitis biomarkers in a complex sample with high chemical selectivity, using an antibody-DNA carrier. This DNA carrier would then undergo translocation through a nanopipette, and the resistive-pulse response measured. Analysis of the translocation event traces would determine whether the biomarker targets were bound or unbound to the antibody probes. From a signal count of bound versus unbound, the concentration of biomarkers in the sample can be calculated, and a diagnosis determined. Achieving this requires addressing several technical challenges, and this work builds upon foundational developments within the Albrecht Group.

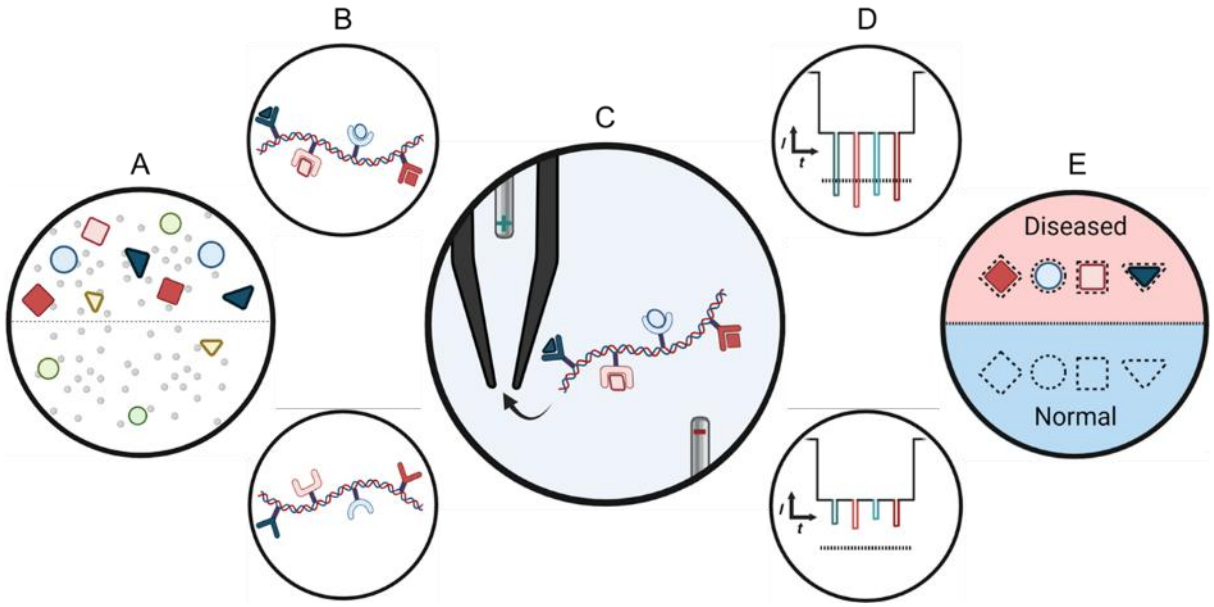


*Figure 1.6: Workflow for disease monitoring with resistive-pulse sensing. A) A complex patient sample with varying concentrations of periodontitis biomarkers. B) Antibody-DNA carrier structures specifically bind to biomarkers, if present in solution. C) The structures undergo DNA translocation with nanopipettes. D) Analysis of the translocation event I(t) traces determines if the probe targets were bound or unbound. E) Cumulatively, the concentration of biomarkers can be calculated and used to determine a diagnosis.*

### 1.2.1 Previous Work

**Linear DNA Translocation at Low Bandwidths**

Initial studies in the group explored the translocation of linear DNA using bandwidths in the range of 10–25 kHz. While these measurements were sufficient to detect DNA translocation through nanopipettes with pore diameters of approximately 20 nm, they were unable to distinguish between overlapping event clusters. Achieving the desired resolution necessitates higher bandwidths (≥100 kHz), which exacerbates noise levels, obscuring the signals of interest. To address this, optimising the experimental setup, particularly noise reduction in the electrical instrumentation, is necessary for high-bandwidth measurements.

**DNA-Aptamer Probe Structures**

SCoNE DNA assembly was developed and tested using 4 kbp double-stranded DNA (dsDNA) structures with two aptamer probes specific to sepsis biomarkers, and target binding to these structures successfully demonstrated.[74] However, expanding the assembly approach to accommodate a broader range of probes, including antibodies, remains a critical challenge. Antibodies have greater off-the-shelf commercial availability for a broader range of targets than aptamers. As such, their integration into DNA carriers would be a significant step towards achieving multiplexed assays and improving the versatility of this technique.

**Analysis of DNA Translocation Events**

Translocation experiments with DNA-aptamer conjugates gave unexpected and varied results, highlighting the need for improved data analysis methods. As a starting point, full characterisation of linear DNA translocation at higher bandwidths (≥100 kHz) is required. This dataset can then be used to help interpret results for more complex DNA constructs.

**Nanopipette Fabrication**

Pulling parameters were optimised, in order to reliably fabricate nanopipettes with pore diameters between 10–25 nm. These pore dimensions are reproducible and suitable for the target analytes in this project. However, unexpected translocation results from previous DNA-aptamer experiments suggest that electrochemical characterisation of nanopipettes is not able to fully describe or explain their performance. A better understanding of the surface chemistry

at the sensing region is essential, in order to better understand transport properties and ensure consistent sensor performance.

## 1.3 THESIS OBJECTIVES

This thesis builds upon the previous foundational work outlined in the project background and focusses on the next steps in the development of nanopore-based multiplexed assays for periodontitis diagnosis. The objectives of each chapter are outlined below.

**Chapter 2 – Noise Optimisation of Nanopore Sensing Equipment**

This chapter focuses on optimising the noise performance of the nanopore sensing setup to enable high-bandwidth measurements at 100 kHz or more. Objectives include benchmarking baseline noise, implementing various noise reduction strategies with a focus on electronic equipment, and evaluating their effectiveness with root-mean-squared (RMS) noise levels and frequency domain analysis.

**Chapter 3 – Developing a DNA-Antibody Conjugate with the SCoNE DNA Assembly Method**

The focus of this chapter is adapting the SCoNE DNA assembly method to include antibodies for the detection of periodontitis protein biomarkers. The key objectives are evaluating the binding affinity and stability of DNA-antibody conjugates, synthesising and isolating an antibody-DNA structure, and determining the compatibility of the structure with nanopore sensing experiments.

**Chapter 4 – Characterisation of DNA Translocation as a Reference for Complex Analytes**

This chapter establishes a reference dataset for linear 4 kbp dsDNA translocation with nanopipettes, using the optimised experimental setup developed in Chapter 2. It also aims to evaluate signal processing algorithms to reliably distinguish and classify translocation events. The work assesses translocation characteristics, signal-to-noise ratios, and event clustering at high bandwidth. These results should serve as a benchmark for analysing more complex DNA structures and provide insights into the experimental setup's capability for resolving subevents.

**Chapter 5 – Nanopipette Sample Preparation and Chemical Analysis**

The final experimental chapter investigates the surface chemistry of quartz nanopipettes to address variability in sensing performance. This involves developing a sample preparation method compatible with high-resolution imaging, employing focused ion beam (FIB) milling for interior access, and testing and comparing the analytical methods energy dispersive X-ray spectroscopy (EDX) with SEM, Auger electron spectroscopy (AES), and time-of-flight secondary ion mass spectrometry (ToF-SIMS). The aim is to use these findings to gain a deeper understanding of nanopipette surface properties and their influence on analyte translocation behaviour.

**Chapter 6 – Conclusions and Future Perspectives**

The concluding chapter will discuss the findings across the thesis, in the context of nanopore-based multiplexed assay for diagnostic applications and identify avenues for further work.

## 1.4 REFERENCES


1 A. Savage, K. A. Eaton, D. R. Moles and I. Needleman, *J Clin Periodontol*, 2009, **36**, 458–467.

2 J. M. Albandar, *Periodontol 2000*, 2014, **65**, 13–26.

3 M. S. Tonetti, S. Jepsen, L. Jin and J. Otomo-Corgel, *J. Clin. Periodontol.*, 2017, **44**, 456–462.

4 M. Sanz, A. Ceriello, M. Buysschaert, I. Chapple, R. T. Demmer, F. Graziani, D. Herrera, S. Jepsen, L. Lione, P. Madianos, M. Mathur, E. Montanya, L. Shapira, M. Tonetti and D. Vegh, *Diabetes Res Clin Pract*, 2018, **137**, 231–241.

5 P. M. Preshaw, A. L. Alba, D. Herrera, S. Jepsen, A. Konstantinidis, K. Makrilakis and R. Taylor, *Diabetologia*, 2012, **55**, 21–31.

6 D. Herrera, M. Sanz, L. Shapira, C. Brotons, I. Chapple, T. Frese, F. Graziani, F. D. R. Hobbs, O. Huck, E. Hummers, S. Jepsen, O. Kravtchenko, P. Madianos, A. Molina, M. Ungan, J. Vilaseca, A. Windak and S. Vinker, *European Journal of General Practice*, 2024, **30**, 2320120.

7 M. Sanz, A. Marco del Castillo, S. Jepsen, J. R. Gonzalez-Juanatey, F. D'Aiuto, P. Bouchard, I. Chapple, T. Dietrich, I. Gotsman, F. Graziani, D. Herrera, B. Loos, P. Madianos, J.-B. Michel, P. Perel, B. Pieske, L. Shapira, M. Shechter, M. Tonetti, C. Vlachopoulos and G. Wimmer, *J Clin Periodontol*, 2020, **47**, 268–288.

8 M. T. Leech and P. M. Bartold, *Best Pract Res Clin Rheumatol*, 2015, **29**, 189–201.

9 A. Dissick, R. S. Redman, M. Jones, B. V Rangan, A. Reimold, G. R. Griffiths, T. R. Mikuls, R. L. Amdur, J. S. Richards and G. S. Kerr, *J Periodontol*, 2010, **81**, 223–230.

10 M. T. Leech and P. M. Bartold, *Best Pract Res Clin Rheumatol*, 2015, **29**, 189–201.

11 M. Ide, M. Harris, A. Stevens, R. Sussams, V. Hopkins, D. Culliford, J. Fuller, P. Ibbett, R. Raybould, R. Thomas, U. Puenter, J. Teeling, V. H. Perry and C. Holmes, *PLoS One*, 2016, **11**, e0151081-.

12 A. Kavarthapu and K. Gurumoorthy, *Oral Oncol*, 2021, **121**, 105375.

13 O. Dizdar, M. Hayran, D. C. Guven, T. B. Yılmaz, S. Taheri, A. C. Akman, E. Bilgin, B. Hüseyin and E. Berker, *Curr Med Res Opin*, 2017, **33**, 2195–2200.

14 V. Baelum and R. Lopez, *Eur J Oral Sci*, 2003, **111**, 2–6.

15 M. S. Tonetti, H. Greenwell and K. S. Kornman, *J Periodontol*, 2018, **89**, S159–S172.

16 V. Galimanas, M. W. Hall, N. Singh, M. D. J. Lynch, M. Goldberg, H. Tenenbaum, D. G. Cvitkovitch, J. D. Neufeld and D. B. Senadheera, *Microbiome*, 2014, **2**, 32.

17 M. Taba Jr., J. Kinney, A. S. Kim and W. V Giannobile, *Dental Clinics*, 2005, **49**, 551–571.

18 E. Kaufman and I. B. Lamster, *J Clin Periodontol*, 2000, **27**, 453–465.

19 N. Arias-Bujanda, A. Regueira-Iglesias, C. Balsa-Castro, L. Nibali, N. Donos and I. Tomás, *J Clin Periodontol*, 2019, **47**, 2–18.

20 S. P. Barros, R. Williams, S. Offenbacher and T. Morelli, *Periodontol 2000*, 2016, **70**, 53–64.

21 W. He, M. You, W. Wan, F. Xu, F. Li and A. Li, *Trends Biotechnol*, 2018, **36**, 1127–1144.

22 T. Albrecht, *Annual Review of Analytical Chemistry*, 2019, **12**, 371–387.

23 F. Haque, J. Li, H.-C. Wu, X.-J. Liang and P. Guo, *Nano Today*, 2013, **8**, 56–74.

24 Y. Wu and J. J. Gooding, *Chem Soc Rev*, 2022, **51**, 3862–3885.

25 S. Wang, Z. Zhao, F. Haque and P. Guo, *Curr Opin Biotechnol*, 2018, **51**, 80–89.

26 A. D. Tyler, L. Mataseje, C. J. Urfano, L. Schmidt, K. S. Antonation, M. R. Mulvey and C. R. Corbett, *Sci Rep*, 2018, **8**, 10931.

27 D. Japrung, A. Bahrami, A. Nadzeyka, L. Peto, S. Bauerdick, J. B. Edel and T. Albrecht, *J Phys Chem B*, 2014, **118**, 11605–11612.

28 R. Ren, S. Cai, X. Fang, X. Wang, Z. Zhang, M. Damiani, C. Hudlerova, A. Rosa, J. Hope, N. J. Cook, P. Gorelkin, A. Erofeev, P. Novak, A. Badhan, M. Crone, P. Freemont, G. P. Taylor, L. Tang, C. Edwards, A. Shevchuk, P. Cherepanov, Z. Luo, W. Tan, Y. Korchev, A. P. Ivanov and J. B. Edel, *Nat Commun*, 2023, **14**, 7362.

29 R. A. Al-Waqfi, O. J. Irving and T. Albrecht, *Biophys J*, 2024, **123**, 439a.

30 N. A. W. Bell and U. F. Keyser, *J Am Chem Soc*, 2015, **137**, 2035–2041.

31 W. Li, N. A. W. Bell, S. Hernández-Ainsa, V. V Thacker, A. M. Thackray, R. Bujdoso and U. F. Keyser, *ACS Nano*, 2013, **7**, 4129–4134.

32 Q. Li, Y.-L. Ying, S.-C. Liu, Y. Lin and Y.-T. Long, *ACS Sens*, 2019, **4**, 1185–1189.

33 N. A. W. Bell and U. F. Keyser, *Nat Nanotechnol*, 2016, **11**, 645–651.

34 S. Confederat, S. Lee, D. Vang, D. Soulias, F. Marcuccio, T. I. Peace, M. A. Edwards, P. Strobbia, D. Samanta, C. Wälti and P. Actis, *Small*, 2024, **20**, 2305186.

35 X. Lin, A. P. Ivanov and J. B. Edel, *Chem Sci*, 2017, **8**, 3905–3912.

36 E. J. Campos and J. Yates, *Sens Actuators B Chem*, 2018, **255**, 2032–2049.

37 K. Chen, J. Kong, J. Zhu, N. Ermann, P. Predki and U. F. Keyser, *Nano Lett*, 2019, **19**, 1210–1215.

38 K. Chen, A. Choudhary, S. E. Sandler, C. Maffeo, C. Ducati, A. Aksimentiev and U. F. Keyser, *Advanced Materials*, 2023, **35**, 2207434.

39 C. Cao and Y.-T. Long, *Acc Chem Res*, 2018, **51**, 331–341.

40 J. Nivala, D. B. Marks and M. Akeson, *Nat Biotechnol*, 2013, **31**, 247–250.

41 M. Zhang, C. Chen, Y. Zhang and J. Geng, *Proteins: Structure, Function, and Bioinformatics*, 2022, **90**, 1786–1799.

42 D. Japrung, M. Henricus, Q. Li, G. Maglia and H. Bayley, *Biophys J*, 2010, **98**, 1856–1863.

43 T. Z. Butler, J. H. Gundlach and M. Troll, *Biophys J*, 2007, **93**, 3229–3240.

44 K.-B. Park, H.-J. Kim, H.-M. Kim, S. A. Han, K. H. Lee, S.-W. Kim and K.-B. Kim, *Nanoscale*, 2016, **8**, 5755–5763.

45 C.-C. Chien, S. Shekar, D. J. Niedzwiecki, K. L. Shepard and M. Drndić, *ACS Nano*, 2019, **13**, 10545–10554.

46 C. Dekker, *Nat Nanotechnol*, 2007, **2**, 209–215.

47 K. Lee, K.-B. Park, H.-J. Kim, J.-S. Yu, H. Chae, H.-M. Kim and K.-B. Kim, *Advanced Materials*, 2018, **30**, 1704680.

48 A. J. Storm, J. H. Chen, X. S. Ling, H. W. Zandbergen and C. Dekker, *Nat Mater*, 2003, **2**, 537–540.

49 E. M. Huisman, A.-L. Biance, A. Madouri, G. Patriarche, E. Bourhis, G. Oukhaled, L. Auvray and J. Gierak, *Microelectron Eng*, 2008, **85**, 1311–1313.

50 S.-Y. Yu, Y.-F. Ruan, Y.-L. Liu, D.-M. Han, H. Zhou, W.-W. Zhao, D. Jiang, J.-J. Xu and H.-Y. Chen, *ACS Sens*, 2021, **6**, 1529–1535.

51 N. Nakatsuka, A. Faillétaz, D. Eggemann, C. Forró, J. Vörös and D. Momotenko, *Anal Chem*, 2021, **93**, 4033–4041.

52 N. Nakatsuka, K. J. Heard, A. Faillétaz, D. Momotenko, J. Vörös, F. H. Gage and K. C. Vadodaria, *Mol Psychiatry*, 2021, **26**, 2753–2763.

53 Y. Zhao, M. Iarossi, A. F. De Fazio, J.-A. Huang and F. De Angelis, *ACS Photonics*, 2022, **9**, 730–742.

54 M. Raveendran, A. J. Lee, R. Sharma, C. Wälti and P. Actis, *Nat Commun*, 2020, **11**, 4384.

55 A. Stuber, A. Cavaccini, A. Manole, A. Burdina, Y. Massoud, T. Patriarchi, T. Karayannis and N. Nakatsuka, *ACS Measurement Science Au*, 2024, **4**, 92–103.

56 S. Denuga, P. Dutta, D. Duleba, G. Macori, S. Fanning and R. P. Johnson, *Anal. Chem.*, 2025, **97**, 2003–2010.

57 G.-C. Liu, W. Chen, M.-J. Gao, L.-B. Song, X.-Y. Hu and Y.-D. Zhao, *Electrochem commun*, 2018, **93**, 95–99.

58 S. Zhang, M. Li, B. Su and Y. Shao, *Annu. Rev. Anal. Chem.*, 2018, **11**, 265-286.

59 M. Kolmogorov, E. Kennedy, Z. Dong, G. Timp and P. A. Pevzner, *PLoS Comput Biol*, 2017, **13**, e1005356-.

60 P. Waduge, R. Hu, P. Bandarkar, H. Yamazaki, B. Cressiot, Q. Zhao, P. C. Whitford and M. Wanunu, *ACS Nano*, 2017, **11**, 5706–5716.

61 C. Plesa, S. W. Kowalczyk, R. Zinsmeester, A. Y. Grosberg, Y. Rabin and C. Dekker, *Nano Lett*, 2013, **13**, 658–663.

62 J. Kong, N. A. W. Bell and U. F. Keyser, *Nano Lett*, 2016, **16**, 3557–3562.

63 A. H. Squires, T. Gilboa, C. Torfstein, N. Varongchayakul and A. Meller, in *Methods in Enzymology*, eds. M. Spies and Y. R. Chemla, Academic Press, 2017, vol. 582, pp. 353–385.

64 B. Hornblower, A. Coombs, R. D. Whitaker, A. Kolomeisky, S. J. Picone, A. Meller and M. Akeson, *Nat Methods*, 2007, **4**, 315–317.

65 S. Abu Jalboush, I. D. Wadsworth, K. Sethi, L. C. Rogers, T. Hollis and A. R. Hall, *ACS Sens*, 2024, **9**, 1602–1610.

66 Y. Qiao, Y. Qian, M. Liu, N. Liu and X. Tang, *Chem Res Chin Univ*, 2019, **35**, 837–841.

67 N. A. W. Bell, M. Muthukumar and U. F. Keyser, *Phys Rev E*, 2016, **93**, 22401.

68 S. W. Kowalczyk, D. B. Wells, A. Aksimentiev and C. Dekker, *Nano Lett*, 2012, **12**, 1038–1044.

69 A. Y. Y. Loh, C. H. Burgess, D. A. Tanase, G. Ferrari, M. A. McLachlan, A. E. G. Cass and T. Albrecht, *Anal Chem*, 2018, **90**, 14063–14071.

70 C. Plesa, N. van Loo, P. Ketterer, H. Dietz and C. Dekker, *Nano Lett*, 2015, **15**, 732–737.

71 K. Chen, M. Juhasz, F. Gularek, E. Weinhold, Y. Tian, U. F. Keyser and N. A. W. Bell, *Nano Lett*, 2017, **17**, 5199–5205.

72 J. Deen, S. Wang, S. Van Snick, V. Leen, K. Janssen, J. Hofkens and R. K. Neely, *Nucleic Acids Res*, 2018, **46**, e64–e64.

73 J. Deen, C. Vranken, V. Leen, R. K. Neely, K. P. F. Janssen and J. Hofkens, *Angewandte Chemie International Edition*, 2017, **56**, 5182–5200.

74 M. H. Lauer, C. Vranken, J. Deen, W. Frederickx, W. Vanderlinden, N. Wand, V. Leen, M. H. Gehlen, J. Hofkens and R. K. Neely, *Chem Sci*, 2017, **8**, 3804–3811.

75 O. J. Irving, L. Matthews, S. Coulthard, R. K. Neely, M. M. Grant and T. Albrecht, *ChemBioChem*, 2023, **24**, e202300361.

76 A. Zrehen, D. Huttner and A. Meller, *ACS Nano*, 2019, **13**, 14388–14398.

77 Z. Zou, H. Yang, Q. Yan, P. Qi, Z. Qing, J. Zheng, X. Xu, L. Zhang, F. Feng and R. Yang, *Chem. Commun.*, 2019, **55**, 6433–6436.

78 K. Sun, P. Chen, S. Yan, W. Yuan, Y. Wang, X. Li, L. Dou, C. Zhao, J. Zhang, Q. Wang, Z. Fu, L. Wei, Z. Xin, Z. Tang, Y. Yan, Y. Peng, B. Ying, J. Chen and J. Geng, *ACS Appl. Mater. Interfaces.*, 2021, **13**, 21030–21039.

79 B. Guo, Y. Zhang, Q. Ren, K. Zhou, L. Liu, H.-C. Wu, *Anal. Sens.*, 2024, **4**, e202400002.

80 R. K. Neely, P. Dedecker, J.-I. Hotta, G. Urbanavičiūtė, S. Klimašauskasb and J. Hofkensa, *Chem. Sci.*, 2010, **1**, 453-460.

81 M. H. Lauer, C. Vranken, J. Deen, W. Frederickx, W. Vanderlinden, N. Wand, V. Leen, M. H. Gehlen, J. Hofkens and R. K. Neely, *Chem. Sci.*, 2017, **8**, 3804-3811.

82 C. Vranken, J. Deen, L. Dirix, T. Stakenborg, W. Dehaen, V. Leen, J. Hofkens and R. K. Neely, *Nucleic Acids Res*, 2014, **42**, e50.

83 D. G. Gibson, L. Young, R.-Y. Chuang, J. C. Venter, C. A. Hutchison III and H. O. Smith, *Nat. Methods*, 2009, **6**, 343–345.

84 P. W. J. Rigby, M. Dieckmann, C. Rhodes and P. Berg, *J. Mol. Biol*., 1977, **113**, 237–251.

85 G. Felsenfeld, D. R. Davies and A. Rich, *J. Am. Chem. Soc*., 1957, **79**, 2023–2024.

# 2 NOISE OPTIMISATION OF NANOPORE SENSING EQUIPMENT

## CONTENTS

# 2.1 INTRODUCTION

In nanopore sensing, noise is a critical experimental consideration. Translocating analytes result in current modulation signals with only picoampere magnitude. In addition, translocation event traces can include even smaller current modulation features, due to conformation, molecular structure, or bound and unbound probe states, in the case of DNA-carriers.[1–4] This information can easily be obscured by background noise in the current signal. Furthermore, a high temporal resolution is necessary to detect subevents, requiring high-bandwidth measurements of 100 kHz and above. Noise contributions scale with filter frequency, necessitating efforts to identify and minimise sources of external noise.

## 2.1.1 SOURCES OF NOISE IN NANOPORE EXPERIMENTS

In nanopore sensing systems, noise in the signal is contributed from a variety of sources, which are categorised by their frequency dependencies (Figure 2.1).[5] These categories are flicker noise, white noise, dielectric noise, and capacitive noise. [5]

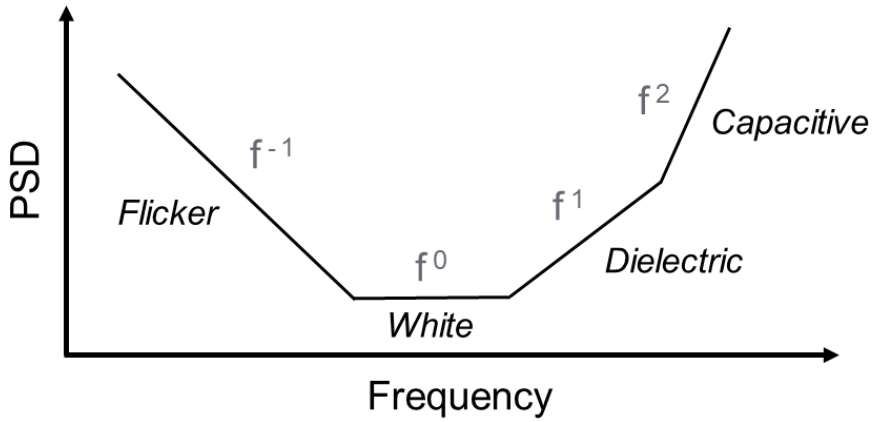


*Figure 2.1: A qualitative plot of the power spectral density (PSD) as a function of frequency for a nanopore set-up. The total current noise PSD is a combination of several different noise sources, each with a different frequency dependency.*

**Flicker Noise**

Also referred to as pink or 1/f noise, flicker noise dominates at low frequencies (< 1 kHz) and scales inversely with increasing frequency. The origins of flicker noise are still speculated, but several mechanisms are proposed in the literature, and they are largely determined by experimental conditions. Some of the proposals include charge trapping,[6] structural fluctuations

of the nanopore walls,[7] and the presence of nanobubbles at the pore surface.[8,9] Flicker noise is more pronounced in solid-state nanopores, particularly silicon nitride chip-based nanopores, due to the increased hydrophobicity of these materials.[10–12] Noise in such chip-based nanopores can be improved with surface treatments, such as atomic layer deposition or oxygen plasma cleaning, to increase hydrophilicity.[10,13–15]

**White Noise**

White noise is frequency independent and typically dominates at mid-range frequencies (0.1 – 2 kHz). It includes thermal (Johnson) noise and shot noise.[16,17] Thermal noise arises from the random thermal motion of ions inside the nanopore,[18] which is linked to the conductance of the solution, and hence electrolyte concentration. The greater the concentration of ions in the electrolyte solution, the greater the contribution of random motion and collisions, which increases noise. Shot noise arises from the inherent quantization of electric charge.[18] White noise represents a fundamental limit to the sensitivity of nanopore measurements; it cannot be entirely eliminated, but can be optimised with certain parameters such as pore size and electrolyte concentration.[18,19]

**Dielectric Noise**

At higher frequencies, 2 – 10 kHz, dielectric noise is the main contributor.[18] It is related to the dielectric properties of the nanopore material, and noise can be exacerbated by current leakage through the dielectric material.[18,19] Glass and quartz nanopipettes have better dielectric properties than silicon nitride nanopores, and as such exhibit lower levels of dielectric noise.[10,12]

**Capacitive Noise**

Beyond these frequencies (typically > 10 kHz), capacitive, or amplifier, noise dominates.[20] It arises from the interaction between the thermal noise at the amplifier input, and the total capacitance of the system. This includes the nanopore, the amplifier and any interconnections.[10] Effective strategies to minimise this noise contribution include reducing the total capacitance and using amplifiers with low parasitic capacitance and thermal noise.[5]

### 2.1.2 High Bandwidth Measurements

To reduce high-frequency noise, most nanopore sensing experiments rely on low-pass filtering of the signal, with cut-off frequencies reportedly in the range of 10 – 100 kHz.[2,4,22] This does have the desired effect of improving the signal-to-noise ratio (SNR), but at the cost of temporal resolution. Translocation events can occur at sub-millisecond timescales, which requires high bandwidth measurements to detect. Achieving high SNR with high bandwidth can require advanced noise reduction strategies, such as optimised amplifier designs, improved dielectric properties, and reduced parasitic capacitance.[10,15,21]

### 2.1.3 Root-Mean-Squared (RMS) Noise

RMS noise is used to assess the overall level of noise in an electrical signal.[23–25] It is a single quantitative value, simplifying comparison of noise performance, and represents the standard deviation of the noise fluctuations in the signal over time. RMS noise is calculated according to Equation 2.1, where $I_{RMS}$ is the noise in the current signal, $I_i$ is the current for datapoint $i$, $\bar{I}$ is the average current value and $n$ is the total number of datapoints.

$$I_{RMS} = \sqrt{\frac{\sum_i^n (I_i - \bar{I})^2}{n}} \tag{2.1}$$

### 2.1.4 Power Spectral Density (PSD) Plots

PSD plots are used to analyse the frequency-dependent characteristics of noise. They provide insights into the distribution and contribution of noise power in the signal across different frequencies, in order to identify specific sources of noise.[26]

PSD is calculated using a Fast Fourier Transform (FFT), which converts the time-domain signal into its frequency components. Noise power ($A^2$/Hz or $V^2$/Hz units) is represented as a function of frequency, providing a visual representation of the noise spectrum, see Figure 2.2. The shape of a PSD plot provides further information. A peak at 50 Hz is common, arising from mains electricity noise interference, alongside harmonics at 100 Hz, 150 Hz, etc.[27] If experimental set-ups are not properly shielded or filtered, these peaks can appear prominent. Thermal noise and shot noise then dominate at higher frequencies, presenting as a flat or gently sloping region of the PSD plot.[28] Analysis of these plots can pinpoint sources of noise interference, allowing for experimental set-ups to be refined.

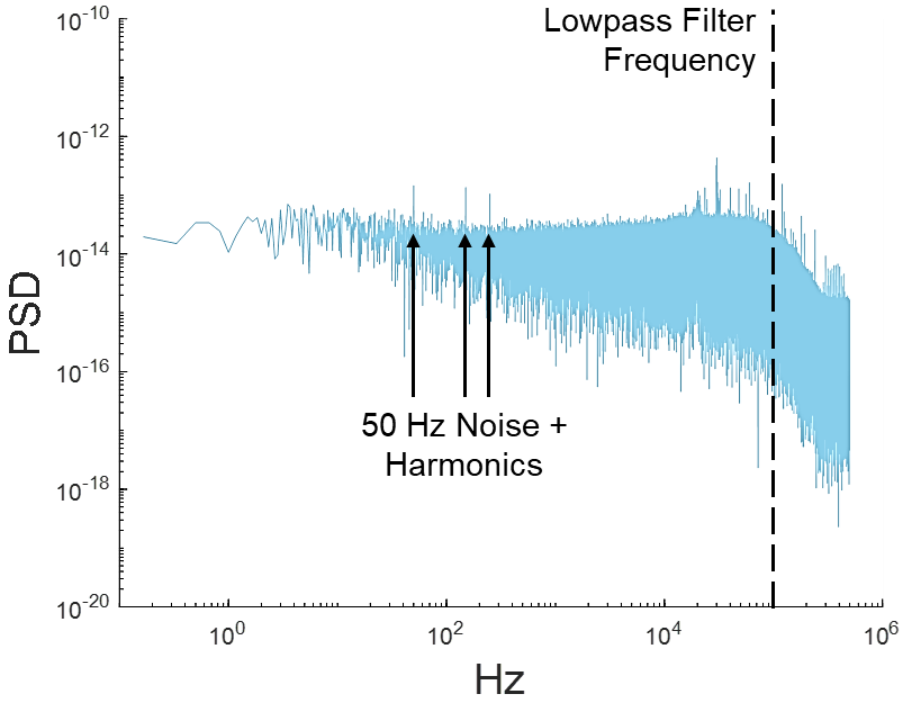


*Figure 2.2: An example of a PSD plot for a nanopore sensing experiment, highlighting the 50 Hz peak with harmonic overtones at low frequency, and the effect of the lowpass filter on high frequency noise.*

Together, RMS noise and PSD plots are useful tools for noise optimisation. RMS noise provides a benchmark for overall noise interference, while PSD plots allow for identification of the specific noise frequencies in the signal. These tools enable verification of noise reduction strategies.

## 2.2 Aims and Objectives

The aim of this chapter was to assess the sources of noise interference in the nanopore set-up and to mitigate these where possible. To achieve this aim, the following objectives were defined:

1. Establish the baseline noise levels of the experimental setup using both a liquid sample cell and a resistor.
2. Using a resistor for controlled comparison, implement the following setup variations:
    - Unfiltered vs. filtered power supply sockets
    - Active vs. passive filtering methods

- Different grounding points
- Mains power supply vs. battery power supply
- Different signal cables connecting the oscilloscope to the PC.

3. Assess the cumulative effect of any changes to equipment and set-up on RMS noise levels and noise frequency contributions, using PSD plots.
4. Compare the optimised set-up to the baseline set-up. Evaluate improvements in performance by analysing both RMS noise and noise frequency distribution in the signal, for both the liquid sample cell and the dummy resistor setup.

## 2.3 MATERIALS AND METHODS

### 2.3.1 LIQUID SAMPLE CELL

Quartz capillaries (outer diameter: 1 mm, inner diameter: 0.5 mm, length: 7.5 cm, Sutter Instruments, USA) were plasma cleaned for 20 minutes. Pipettes were fabricated using a P2000 pipette puller (Sutter Instruments, USA) with the following parameters: heat 750/850, filament 5/0, velocity 35/15, delay 150/128, pull 75/200. This process typically produced pipettes with pore diameters of 20–30 nm and a taper length of approximately 3 mm. Pipette taper lengths were measured using an optical microscope (Type 105, Nikon, Japan) with 4x magnification.

Amber glass vials with screw-top lids were used for the liquid sample cell. Two 1 mm holes were drilled into the vial lid for the electrode and pipette. The lid and the vial were then plasma cleaned for 20 minutes. The electrolyte solution consisted of 4 M anhydrous lithium chloride, MilliQ water, and 10 % TE buffer, filtered through a 0.2 µm filter. Two mL of the electrolyte solution was added to the vial, and the nanopipette was filled with electrolyte using a Microfill 34-gauge needle before insertion into the vial.

Silver/silver chloride electrodes were prepared by immersing silver wire (0.25 mm diameter, 99.998 % purity) in 35.5 % nitric acid for 20 seconds, rinsing with MilliQ water, and anodising electrochemically using a gold counter electrode with a 1 mA current for 20 minutes. Electrodes were re-anodised before use to prevent AgCl depletion. One electrode was placed in the nanopipette and the other in the electrolyte.

### 2.3.2 NANOPORE SENSING INSTRUMENTATION

Figure 2.3 shows a schematic of the nanopore set-up. With an aim to characterise and reduce the noise contribution from the instrumentation, the liquid sample cell was tested twice; first as a benchmark, and then after optimisation to determine any improvement. During optimisation, the liquid sample cell was replaced with a 40 MΩ resistor. This allowed for direct comparison between the noise profiles that would not have been possible (owing to inherent variations between electrodes and nanopipettes) had a liquid sample cell been used, as exact reproducibility is difficult. The resistor was placed within a small Faraday cage containing a low-pass filter to reduce 50 Hz noise. A second, larger Faraday cage was grounded to the mains and used to hold both the smaller Faraday cage and the signal amplifier, to protect the equipment from external noise sources. For further protection from external noise sources and to minimise current leakage, all connecting cables were shielded with copper tape, kept as short as possible and placed within the Faraday cage when practical. All equipment bar the PC was placed on a granite worktop to reduce mechanical vibrations.

Custom-written MATLAB code (authored by Tim Albrecht, University of Birmingham, UK) was used for instrument control, data acquisition and analysis. A bias voltage was applied to the resistor and the current-time ($I(t)$) signal measured using a low-noise amplifier, dubbed 'Polimi' (designed and built by Pietro Ciccarella, Marco Carminati and Giorgio Ferrari, Politecnico di Milano, Italy).[29–31]

The amplifier splits the current signal into two channels, an alternating current (AC) and a direct current (DC) channel. Slow modulations of current, below approximately 10 Hz, are contained in the DC signal. Therefore, the DC signal responds slowly to current changes and details the open pore current. The AC signal contains fast current modulation, greater than 10 Hz, and is used to detect fast changes to the current signal, such as current blockages. As such, translocation events appear in the AC signal.[29–31]

The analogue signal from the AC channel is passed through a low-pass Bessel filter (8 poles, 3940 Krohn-Hite filter, Krohn-Hite Corporation, USA) and then digitised using the AD converter in an oscilloscope (PicoScope 4262, Pico Technology, UK). The signal from the DC channel passes, without filtering, to the oscilloscope for digitisation.

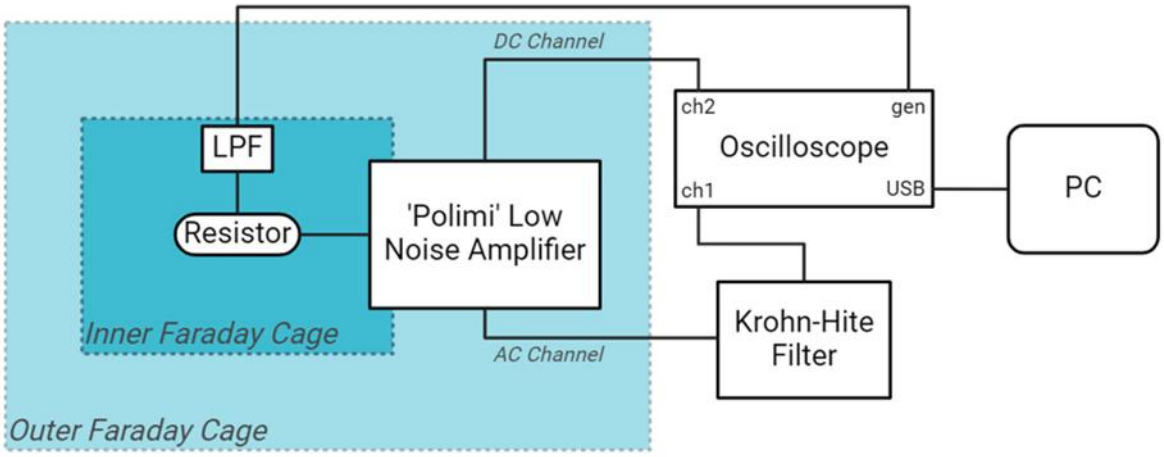


*Figure 2.3: Schematic representation of the modified nanopore set-up, containing a resistor, 'Polimi' amplifier, low-pass filters, and oscilloscope. A voltage is applied to the resistor using a PicoScope oscilloscope. The current signal is amplified and split into two channels by the 'Polimi' amplifier. The AC channel is filtered through a low-pass 8-pole Bessel filter before digitisation, alongside the DC channel, by an AD converter in the oscilloscope. The small and large Faraday cage are represented by the dashed lines.*

The active Krohn-Hite filter was replaced with a passive filter (Low-Pass Electrical Filters BNC Feedthrough, ThorLabs GmbH, Germany) when specified. The large Faraday cage was grounded to either the mains power or a metal water pipe.

When testing the oscilloscope – PC connection for noise, only the PC, connecting USB cable and oscilloscope were used for signal acquisition. All other ports on the oscilloscope were capped with a 50 Ω terminator. Three USB cables were tested: 'blue' (Pico Technology, UK), 'black' (supplier unknown) and 'pearl' (AudioQuest).

### 2.3.3 Data Acquisition and Analysis

The signal was sampled at 1 MHz and filtered at 10 kHz or 100 kHz, as specified. Custom MATLAB codes recorded the data and output a log file, containing the RMS noise, mean and standard deviation of both signal channels. At each bias, the RMS noise of the AC channel for three *I(t)* traces from the same experiment were averaged.

Custom MATLAB code (authored by Tim Albrecht, University of Birmingham, UK) was used to perform a FFT of *I(t)* traces and to plot PSD graphs.

## 2.4 RESULTS AND DISCUSSION

### 2.4.1 BASELINE NOISE MEASUREMENTS

First, the RMS noise and PSD plots of the nanopore set-up were established as a reference point for further optimisation. These were generated for both a resistor and a liquid sample cell (Figure 2.4). In the PSD plots, distinct noise contributions are observed, beginning with 50 Hz (mains interference) and harmonic overtones. Smaller noise contributions were observed at frequencies above 10 kHz.

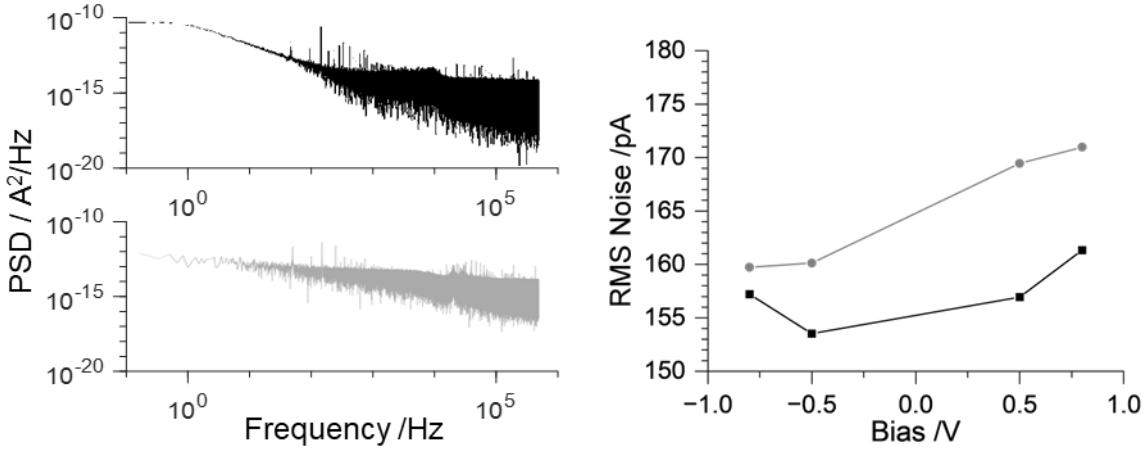


*Figure 2.4: PSD plots and RMS noise profiles of the initial nanopore set-up for both the resistor (black) and liquid sample cell (grey). Both experiments were performed with a 10 kHz lowpass filter.*

The calculated RMS noise for the resistor ranged between 150 and 160 pA, whereas for the liquid sample cell it was slightly higher, between 160 and 175 pA. This increase in RMS noise for the liquid sample cell is expected, due to the additional sources of noise in this set-up, such as dielectric loss and capacitance noise.

### 2.4.2 COMPARISON OF EXPERIMENTAL SET-UPS WITH A RESISTOR

Using a resistor for controlled comparison, the following changes to equipment were implemented and the noise assessed: unfiltered vs. filtered power supply sockets, active vs. passive filtering methods, different grounding points, mains power supply vs. battery power supply and, finally, different signal cables connecting the oscilloscope to the PC.

**Effect of Standard vs. Filtered Extension Lead on Noise**

In an effort to minimize 50 Hz noise and associated overtones from the mains electricity, the effect of using a standard extension lead versus a filtered extension lead to power all equipment was investigated. A filtered extension lead contains surge suppression and interference suppression filters to protect electronic equipment from overvoltages and high current peaks from the power supply, and both electromagnetic and radio frequency interference. The results, shown in Figure 2.5, indicate that the background noise was generally lower when the filtered extension lead was used. While some 50 Hz noise peaks remained, they were reduced, and the high-frequency noise contributions (>10 kHz) were similar between the two leads.

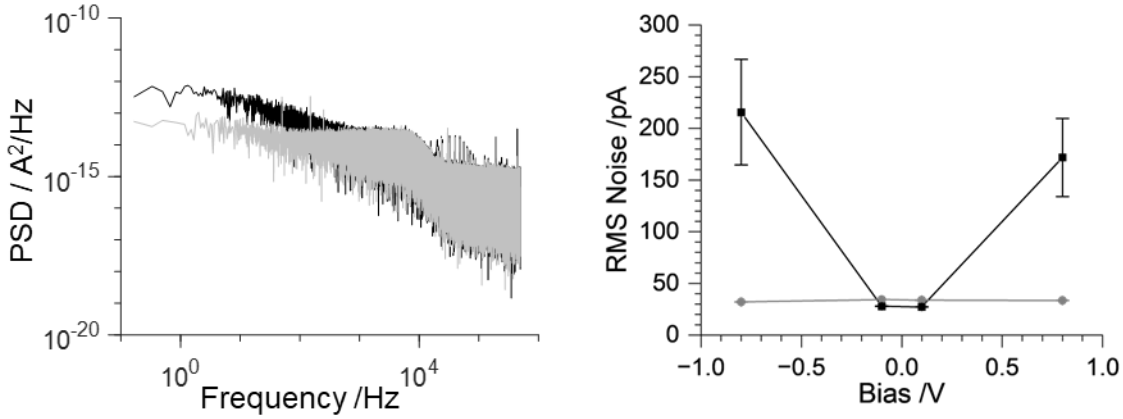


*Figure 2.5: PSD plots and RMS noise profiles comparing the performance of a standard extension lead (black) and a filtered extension lead (grey). Both experiments used a 10 kHz lowpass filter.*

The RMS noise for both extension leads was less than 50 pA at ±0.1 V. At higher bias voltages (±0.8 V), the performance of the two leads diverged. RMS noise for the standard extension lead was over 150 pA, whereas the filtered lead consistently reduced the noise to below 50 pA at all biases. As a result, the filtered extension lead replaced the standard extension lead, and was used throughout the following experiments.

**Active vs. Passive Lowpass Filters**

To reduce noise interference from the mains power further, passive and active lowpass filters were compared. Active filters, which rely on powered components such as op-amps and transistors, can introduce additional noise. Passive filters, using only resistors and capacitors, do not require external power. Both filters had a cutoff frequency of 100 kHz.

As seen in Figure 2.6, PSD plots for both lowpass filters showed 50 Hz noise. For the passive filter, a steeper cutoff at 100 kHz was observed, with fewer high-frequency noise contributions, particularly around 6 kHz. The passive filter consistently reduced the RMS noise from 28 pA to 12 pA. Therefore, the passive filter was adopted for further use in the setup.

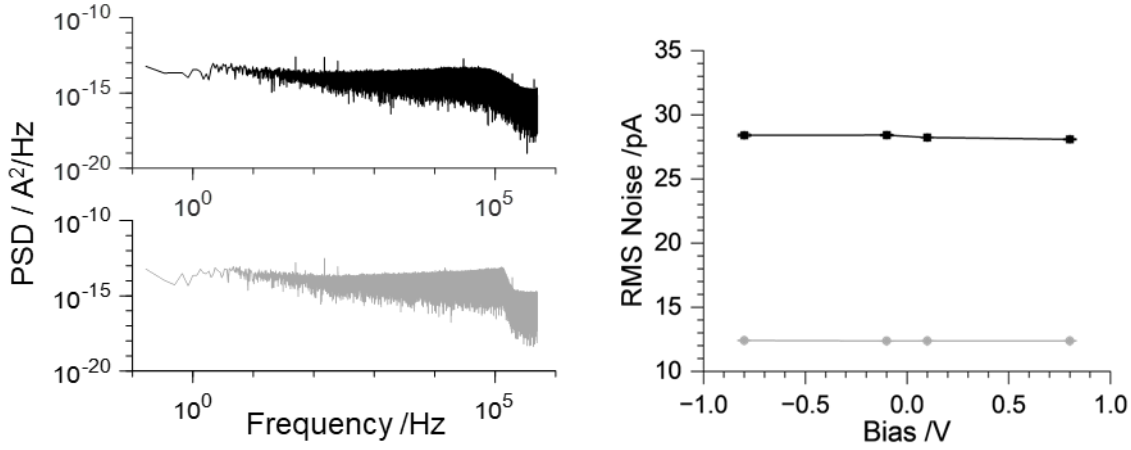


*Figure 2.6: PSD plots and RMS noise profiles comparing the performance of an active lowpass filter (black) and a passive lowpass filter (grey). Both experiments used a 100 kHz lowpass filter.*

**Evaluation of Grounding Points**

The impact of different grounding points was then investigated, comparing the performance of grounding the Faraday cage to a metal water pipe versus a newly installed grounding wire. High-precision electronic measurements typically require isolated "clean" grounding to avoid noise cross-contamination from other equipment, whereas "dirty" grounding connects to shared systems that may introduce noise interference.[32,33]

Contrary to expectations, using the dedicated grounding wire resulted in higher noise levels, particularly above 10 kHz (Figure 2.7). This increase is likely due to cross-contamination noise and potential ground loops induced by connecting to the same ground source as other powered electrical instruments. The metal water pipe, by contrast, provided a more independent connection to the building's main ground and helped shield the equipment from high-frequency noise.[32,33] The RMS noise was slightly lower when using the water pipe (13.0 pA at -0.8 V) compared to the grounding wire (13.8 pA at -0.8 V). Consequently, the water pipe was retained as the preferred grounding option.

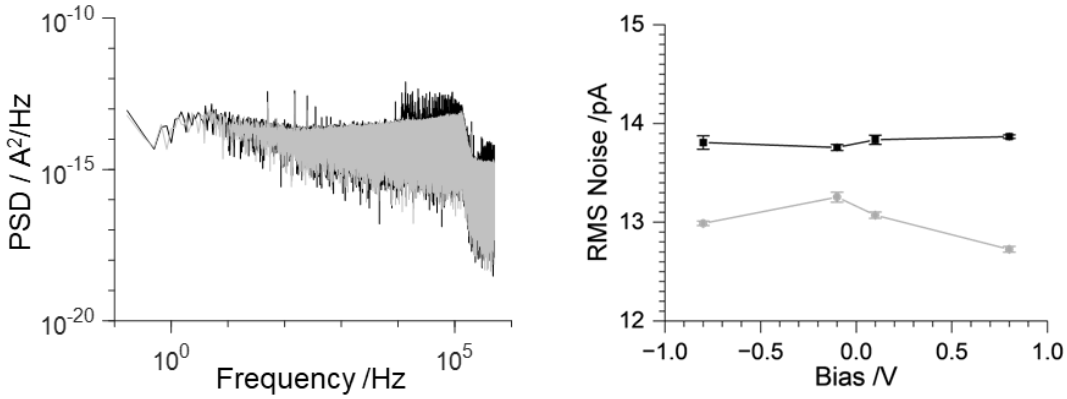


*Figure 2.7: PSD plots and RMS noise profiles comparing performance when the Faraday cage was grounded to a dedicated grounding wire (black) or a metal water pipe (grey). Both experiments were performed with a 100 kHz lowpass filter.*

**Replacement of Mains Power with Battery Power**

To eliminate 50 Hz noise contributions from mains electricity, the amplifier was powered by a battery pack, and an unplugged laptop was used instead of a desktop PC. The results, displayed in Figure 2.8, show a significant reduction in both 50 Hz noise and low-frequency contributions. While some high-frequency noise remained, the RMS noise range improved from 20.8–60.5 pA using mains power to 13.9–30.7 pA with battery power.

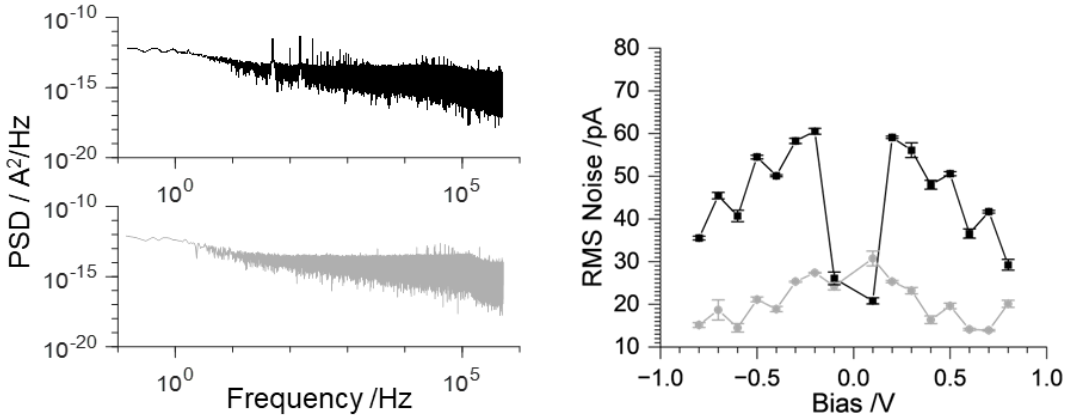


*Figure 2.8: PSD plots and RMS noise profiles comparing performance when the equipment was powered with mains power (black) or battery power (grey). Both experiments were performed with a 100 kHz lowpass filter.*

However, long-term use of battery-powered setups proved impractical for extended translocation experiments due to the limited battery life of the laptop. As such, a connection to mains power was necessary.

**Impact of USB Cables on Noise Reduction**

As mains power was unavoidable, different USB cables connecting the oscilloscope and PC were tested to assess their impact on noise levels. Three cables were compared: a standard 'blue' cable provided with the oscilloscope, a 'black' cable featuring a ferrite core, and a 'pearl' cable with enhanced shielding and a solid conductor core. Results are shown in Figure 2.9.

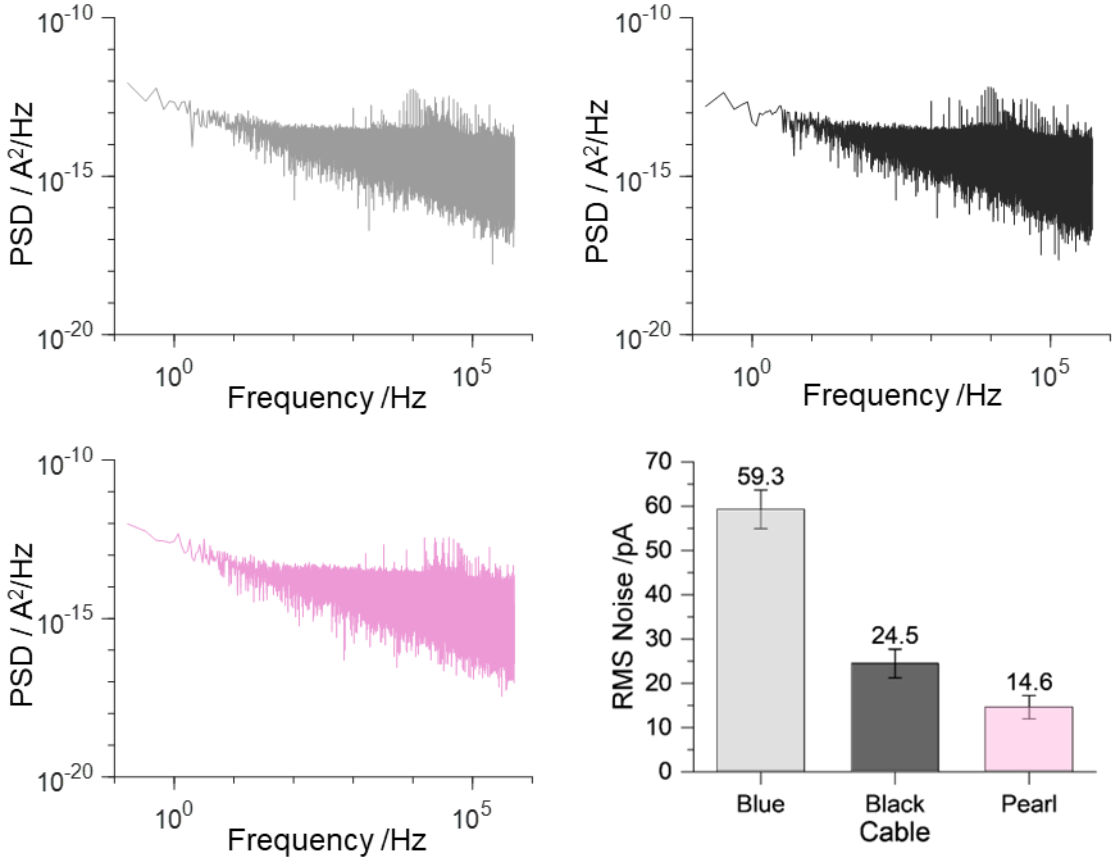


*Figure 2.9: PSD plots and average RMS noise for different USB cables, a standard 'blue' cable (grey), a 'black' cable (black), or a 'pearl' cable (pink).*

The PSD plots indicate that both the 'blue' and 'black' cables exhibited noise contributions in the 10 kHz range and above, with the 'black' cable performing slightly better. However, the

"pearl" cable demonstrated a significant reduction in high-frequency noise, resulting in RMS noise values of 58.4 pA (blue), 24.8 pA (black), and 14.3 pA (pearl).

The improvement seen moving from the ‘blue’ to the ‘black’ cable may be due to the ferrite core. This ferrite core acts as a choke, preventing the cable from acting as an antenna and receiving electromagnetic interference from external sources.[34] The further reduction in noise moving from the ‘black’ to the ‘pearl’ cable is purported to be two-fold. First, the ‘pearl’ cable is internally shielded using hard-cell foam. This shielding supposedly does not release heat, unlike the ferrite core, and so reduces distortion of the carried signal. Secondly, the cable uses solid long-grain copper, whereas the ‘black’ cable uses standard oxygen-free high-conductivity copper. The manufacturer of the ‘pearl’ cable claims “solid conductors prevent strand interaction, a major source of distortion”, alongside better surface quality, resulting in a better performance.[35]

### 2.4.3 Noise Analysis and Optimisation

A comparison between the performance of the initial experimental setup and the optimised setup is presented in Figure 2.10, highlighting the cumulative effect of incremental improvements made throughout the noise optimisation process.

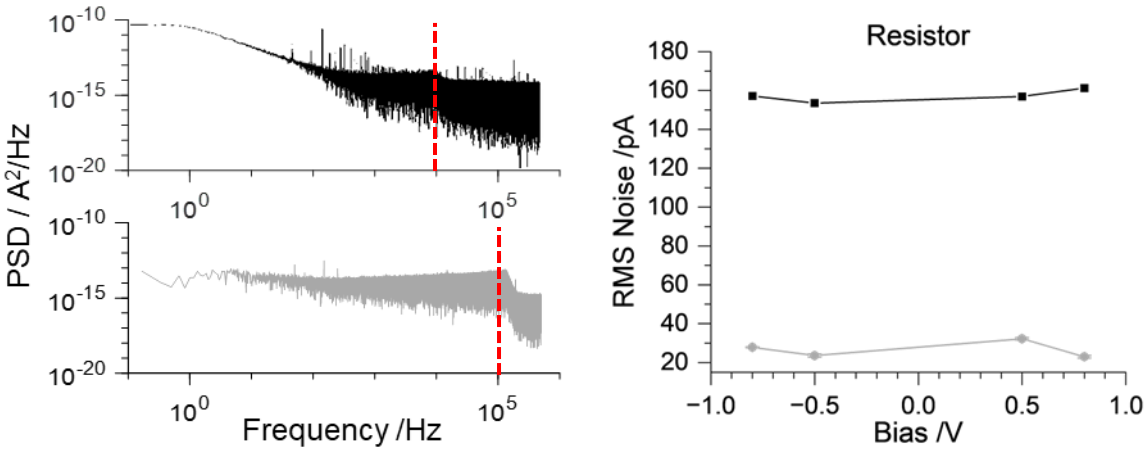


*Figure 2.10: PSD plots and RMS noise profiles comparing the performance of the initial experimental set-up (black) and the optimised set-up (grey), both with a resistor. The red dotted line on the PSD plots represents the lowpass filter frequency cut-off, at 10 kHz (initial set-up) and 100 kHz (optimised set-up).*

The PSD plots indicate that, although the 50 Hz noise contribution was not entirely eliminated in the optimised setup, a reduction was achieved. The starting set-up employed a 10 kHz

lowpass filter, whereas the optimised setup used a 100 kHz lowpass filter. A higher filter frequency is necessary for future experiments with complex analyte translocation, such as DNA carriers. A 100 kHz lowpass filter allows for higher signal resolution, necessary to detect quick subevents during translocation which could be missed with a 10 kHz filter. Despite this increase in bandwidth, which typically increases noise, a large improvement in noise performance was demonstrated with the optimised set-up.

The RMS noise for the optimised set-up was 27.8 pA at -0.8 V, down from 157 pA for the initial setup at the same bias voltage. This substantial reduction in RMS noise demonstrates the success of the various changes implemented, despite the increase in bandwidth from 10 kHz to 100 kHz.

### 2.4.4 Application to Liquid Sample Cell

The optimised set-up was tested with a liquid sample cell, and a comparison with the initial set-up presented in Figure 2.11. Low frequency noise contributions and 50 Hz noise are shown to be reduced in the PSD plots of the optimised set-up. Comparison of the RMS noise levels for each set-up shows a marked improvement following optimisation. At -0.8 V, the RMS noise decreased from 160 pA to 26.9 pA, even when increasing bandwidth from 10 kHz to 100 kHz.

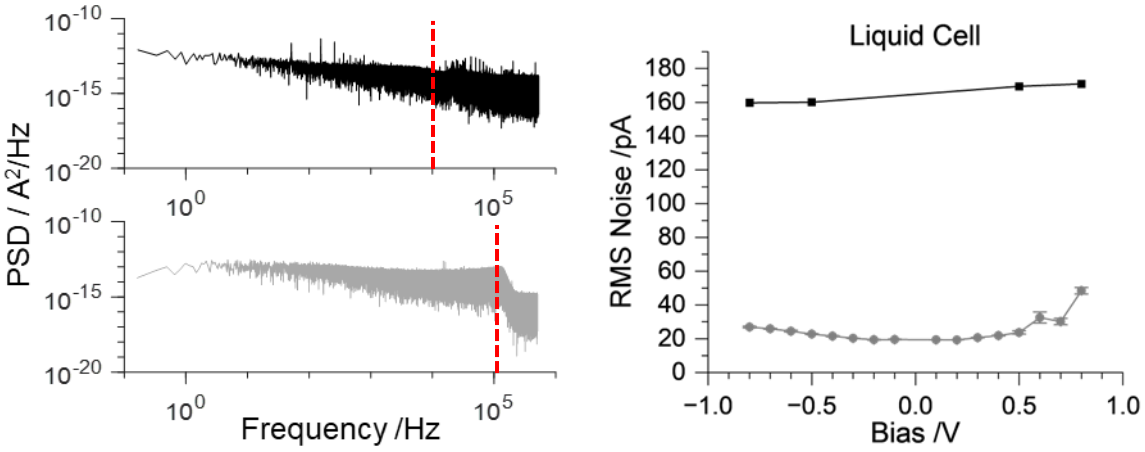


*Figure 2.11: PSD plots and RMS noise profiles comparing the performance of the initial experimental set-up (black) and the optimised set-up (grey), both with a liquid sample cell. The red dotted line on the PSD plots represents the lowpass filter frequency cut-off, at 10 kHz (initial set-up) and 100 kHz (optimised set-up).*

In summary, the optimisation process achieved a substantial reduction in noise for the nanopore set-up. An 82% reduction in RMS noise was observed for a resistor, and an 83% reduction

observed for a liquid sample cell. The optimised setup was adopted for subsequent translocation experiments, enabling high bandwidth measurements.

## 2.5 CONCLUSIONS AND FUTURE WORK

The primary objective of this chapter was to reduce noise contributions from the instrumentation used in nanopore sensing experiments, enabling translocation experiments to be performed with a ≥ 100 kHz lowpass filter. The following conclusions were drawn from the optimisation process:

1. **Resistor-based testing:**
    - Filtered extension leads reduced overall RMS noise.
    - Passive filtering effectively reduced high-frequency noise contributions and lowered RMS noise.
    - The grounding wire introduced significant high-frequency noise due to the formation of ground loops.
    - Battery-powered equipment eliminated 50 Hz noise and its overtones.
    - Higher-quality data transmission cables further reduced overall noise.
2. **Overall noise reduction:**
    - An 82% reduction in noise was achieved using the optimised set-up with a resistor.
    - An 83% reduction in noise was observed when applying the optimised set-up to the liquid sample cell.
    - This improvement in performance was observed when increasing measurement bandwidth from 10 kHz to 100 kHz.

For future work, it would be useful to perform further noise measurements during experiments, in order to benchmark any differences in noise over time. As noise performance can fluctuate, a longer-term study and a collection of data from a variety of experimental conditions would be beneficial to provide a true indication of ‘average’ noise performance of the optimised set-up.

There are additional sources of noise yet to be investigated and optimised, particularly those pertaining to the liquid sample cell. For example, reducing the volume of the electrolyte reservoir could reduce noise by minimising capacitance and dielectric loss. Exploring simple adjustments to the liquid sample cell could likewise contribute further reductions to noise levels, allowing for further increases in recording bandwidth.

## 2.6 REFERENCES


1 N. A. W. Bell and U. F. Keyser, *J Am Chem Soc*, 2015, **137**, 2035–2041.

2 N. A. W. Bell and U. F. Keyser, *Nat Nanotechnol*, 2016, **11**, 645–651.

3 A. Y. Y. Loh, C. H. Burgess, D. A. Tanase, G. Ferrari, M. A. McLachlan, A. E. G. Cass and T. Albrecht, *Anal Chem*, 2018, **90**, 14063–14071.

4 J. Kong, N. A. W. Bell and U. F. Keyser, *Nano Lett*, 2016, **16**, 3557–3562.

5 K. Lee, K.-B. Park, H.-J. Kim, J.-S. Yu, H. Chae, H.-M. Kim and K.-B. Kim, *Advanced Materials*, 2018, **30**, 1704680.

6 S. Gravelle, R. R. Netz and L. Bocquet, *Nano Lett*, 2019, **19**, 7265–7272.

7 S. M. Bezrukov and M. Winterhalter, *Phys Rev Lett*, 2000, **85**, 202–205.

8 R. Roth, D. Gillespie, W. Nonner and R. E. Eisenberg, *Biophys J*, 2008, **94**, 4282–4298.

9 R. M. M. Smeets, U. F. Keyser, M. Y. Wu, N. H. Dekker and C. Dekker, *Phys Rev Lett*, 2006, **97**, 88101.

10 V. Tabard-Cossa, D. Trivedi, M. Wiggin, N. N. Jetha and A. Marziali, *Nanotechnology*, 2007, **18**, 305505.

11 Z. Siwy and A. Fuliński, *AIP Conf Proc*, 2003, **665**, 273–282.

12 L. J. Steinbock, R. D. Bulushev, S. Krishnan, C. Raillon and A. Radenovic, *ACS Nano*, 2013, **7**, 11255–11262.

13 P. Chen, T. Mitsui, D. B. Farmer, J. Golovchenko, R. G. Gordon and D. Branton, *Nano Lett*, 2004, **4**, 1333–1337.

14 C. A. Merchant, K. Healy, M. Wanunu, V. Ray, N. Peterman, J. Bartel, M. D. Fischbein, K. Venta, Z. Luo, A. T. C. Johnson and M. Drndić, *Nano Lett*, 2010, **10**, 2915–2921.

15 E. Beamish, H. Kwok, V. Tabard-Cossa and M. Godin, *Nanotechnology*, 2012, **23**, 405301.

16 A. Fragasso, S. Pud and C. Dekker, *Nanotechnology*, 2019, **30**, 395202.

17 C. Tasserit, A. Koutsioubas, D. Lairez, G. Zalczer and M.-C. Clochard, *Phys Rev Lett*, 2010, **105**, 260602.

18 J. D. Uram, K. Ke and M. Mayer, *ACS Nano*, 2008, **2**, 857–872.

19 A. J. W. Hartel, S. Shekar, P. Ong, I. Schroeder, G. Thiel and K. L. Shepard, *Anal Chim Acta*, 2019, **1061**, 13–27.

20 J. K. Rosenstein, M. Wanunu, C. A. Merchant, M. Drndic and K. L. Shepard, *Nat Methods*, 2012, **9**, 487–492.

21 V. Tabard-Cossa, in *Engineered Nanopores for Bioanalytical Applications*, eds. J. B. Edel and T. Albrecht, William Andrew Publishing, Oxford, 2013, pp. 59–93.

22 J. Rosenstein, M. Wanunu, M. Drndic and K. L. Shepard, *Biophys J*, 2012, **102**, 428a.

23 W. M. Parkin and M. Drndić, *ACS Sens*, 2018, **3**, 313–319.

24 M. Albu and G. T. Heydt, *IEEE Transactions on Power Delivery*, 2003, **18**, 1586–1587.

25 P. Dutta and P. M. Horn, *Rev Mod Phys*, 1981, **53**, 497–516.

26 Z. Siwy and A. Fuliński, *AIP Conf Proc*, 2003, **665**, 273–282.

27 R. M. M. Smeets, U. F. Keyser, N. H. Dekker and C. Dekker, *Proceedings of the National Academy of Sciences*, 2008, **105**, 417–421.

28 V. Dimitrov, U. Mirsaidov, D. Wang, T. Sorsch, W. Mansfield, J. Miner, F. Klemens, R. Cirelli, S. Yemenicioglu and G. Timp, *Nanotechnology*, 2010, **21**, 065502.

29 R. L. Fraccari, M. Carminati, G. Piantanida, T. Leontidou, G. Ferrari and T. Albrecht, *Faraday Discuss*, 2016, **193**, 459–470.

30 P. Ciccarella, M. Carminati, G. Ferrari, R. Fraccari and A. Bahrami, in *2014 10th Conference on Ph.D. Research in Microelectronics and Electronics (PRIME)*, 2014, pp. 1–4.

31 R. L. Fraccari, P. Ciccarella, A. Bahrami, M. Carminati, G. Ferrari and T. Albrecht, *Nanoscale*, 2016, **8**, 7604–7611.

32 Power Quality: Symptoms & Solutions, http://www.marcspages.co.uk/pq/3353.htm, (accessed December 2024).

33 Bonding of isolated, common & integrated grounding systems, Electrical Engineering Portal, https://electrical-engineering-portal.com/bonding-of-isolated-common-and-integrated-grounding-systems, (accessed December 2024).

34 J. Carr, *RF Components and Circuits*, Bedford, 2002.

35 Pearl, AudioQuest, https://www.audioquest.com/products/pearl-usb-a-b-digital-audio-cable, (accessed December 2024).

# 3 DEVELOPING A DNA-ANTIBODY CONJUGATE WITH THE SCONE DNA ASSEMBLY METHOD

## CONTENTS

# 3.1 INTRODUCTION

For diagnosis and monitoring of various diseases, accurate and efficient detection of proteins is necessary. Antibodies are well-studied, particularly in diagnostic applications, owing to their chemical specificity and high affinity for target molecules. For protein detection, enzyme-linked immunosorbent assay (ELISA) and mass spectrometry (MS) are well-established techniques. However, these methods are not without limitations, most particularly their inability to detect multiple proteins simultaneously. There is, therefore, an interest in developing multiplexed protein detection techniques, so as to improve diagnostic accuracy and efficiency.[1–6]

## 3.1.1 LIMITATIONS OF PROTEIN DETECTION TECHNIQUES

ELISA is a well-established technique used for the detection and quantification of proteins. In its most simple form, direct ELISA, the technique relies on specific binding between the antibody and the target antigen immobilized on a well-plate surface. Owing to its use of monoclonal antibodies, which bind to a specific epitope of the antigen target, ELISA techniques are often highly specific and sensitive (down to sub-picomolar detection concentrations[7]) with typically low cross-reactivity. However, the technique is not without limitations. One such limitation is its single-analyte detection capability per well (see Figure 3.1). To perform multiplexed assay, multiple wells are required, involving 100 µL of prepared sample per well. This is not viable for incredibly small sample volumes, such as from gingival crevicular fluid, and also where many target antigens may need to be detected for diagnostic applications. As such, using ELISA to detect multiple biomarkers in a single sample is impractical. This severely limits the diagnostic ability of ELISAs, where detection of multiple biomarkers is necessary to determine disease status and progression.[8,9]

Furthermore, an ELISA workflow includes many steps, such as washing, blocking, and incubation, often repeated several times, introducing potential for error. In complex samples with more abundant background proteins, it can be difficult to detect low concentrations of proteins owing to the limited dynamic range of this method.[8] In addition, the signal (enzyme-substrate reactions facilitate colour change) is susceptible to background noise from non-specific binding. This can have a further detrimental effect on sensitivity and specificity, particularly in more complex biological samples, such as serum or saliva.[8,9]

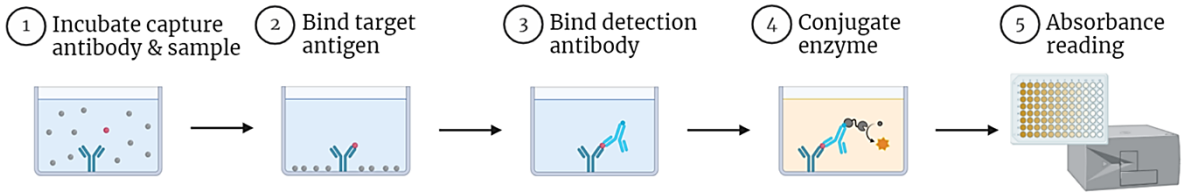


*Figure 3.1: Simplified sandwich ELISA workflow schematic. 1) Incubation of capture antibody on the plate surface and introduction of the sample. 2) Target antigen binds specifically to the capture antibody. 3) Addition of a detection antibody specific to a different epitope on the target antigen, forming a sandwich complex. 4) Conjugation of an enzyme to the detection antibody, facilitating colour change which forms the signal. 5) Measurement of absorbance following the enzymatic reaction, proportional to the amount of bound antigen. For clarity, washing steps between each phase have been omitted from this schematic.*

An alternative method for protein detection, mass spectrometry (MS), is able to analyse complex samples and identify multiple proteins simultaneously (Figure 3.2), but often requires sophisticated instrumentation and operator expertise. In addition to this, time- and labour-intensive sample preparation processes can be necessary; further purification and enrichment steps can be required to achieve the desired level of sensitivity. Finally, labelled standards are required for quantitative analysis, adding to the overall cost and complexity of the technique. These additional steps restrict the use of MS in diagnostic applications.[10]

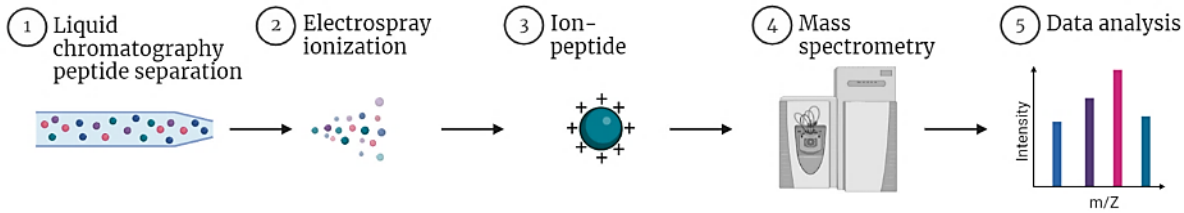


*Figure 3.2: Simplified mass spectrometry workflow schematic. 1) Liquid chromatography is used to separate peptide mixtures based on their properties, such as hydrophobicity. 2) Peptides are ionized by electrospray ionization. 3) The ionized peptides are directed into the mass spectrometer. 4) Ions are analysed based on their mass-to-charge ratio, generating a spectrum. 5) Resulting spectra are processed to identify and quantify peptides, correlating mass data with protein sequences.*

### 3.1.2 Multiplexed Protein Detection for Diagnosing Periodontitis

With the most common techniques having these significant limitations, new techniques are being explored to allow for multiplexed protein assay. In order to accurately diagnose and

monitor periodontitis, a multifactorial disease, several biomarkers would need to be detected in one assay.[11–13] These biomarkers could include inflammatory mediators, tissue degradation products and microbial proteins.[12,13] Such an approach could potentially allow for improved diagnosis accuracy, disease progression monitoring, and earlier detection.

### 3.1.3 Antibodies and Dissociation Constants

Antibodies, also known as immunoglobulins, are Y-shaped proteins produced as part of a cell's immune response. An antibody structure has three main components; two identical heavy chains, and two identical light chains, held together by disulfide bonds. Antibodies are described as having two regions; a constant (Fc) region, responsible for immune effector functions, and a variable (Fab) region, which binds specific antigens.

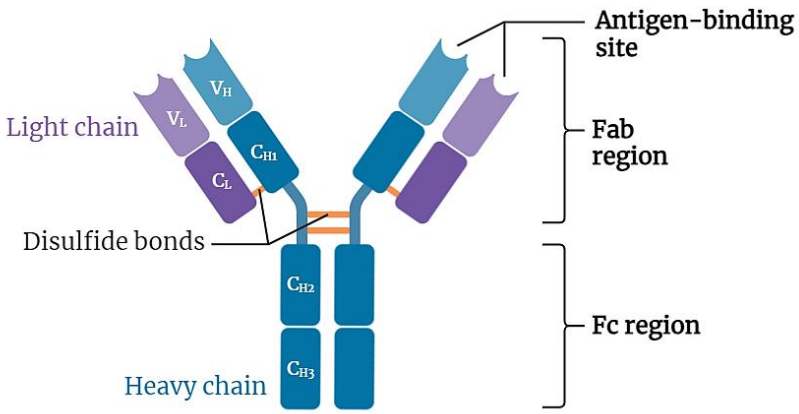


*Figure 3.3: Illustration of the basic structure of an IgG antibody. Two identical light chains (purple) form part of the antigen binding site, the two identical heavy chains (blue) provide the structural framework and define the class of the antibody, with the disulfide bonds (orange) stabilising the structure. The antigen binding site is located at the variable regions of the Fab fragments, responsible for specific antigen binding. The Fc region mediates immune system interactions.*

The binding affinity is commonly used to describe the strength of the binding interaction between an antibody and antigen, and this binding process is reversible. As such, the formation of an antibody-antigen complex exists in equilibrium, which is defined by the dissociation constant ($K_D$). $K_D$ defines the tendency of a complex to reversibly dissociate into its constituent parts and is the inverse of binding affinity. $K_D$ values for typical antibody-antigen complexes are in the range of $10^{-6}$ to $10^{-14}$ M.

Antibodies with a low $K_D$ have a high affinity for their target antigen, resulting in a stable and strong non-covalent bond. Antibodies can also be modified by conjugation to various molecules, such as DNA,[14–16] radioisotopes[17,18] and toxins.[19,20] This could potentially lead to changes in the binding ability and stability of antibodies if conjugation occurs at the binding site.[21]

### 3.1.4 SCoNE DNA Assembly Method

The sterically controlled nuclease-enhanced (SCoNE) DNA assembly method allows for tuneable design and controlled synthesis of DNA carriers, using Gibson assembly methods and customisable sticky-end cohesion. The technique has been developed and tested using aptamers as target-binding probes for sepsis biomarkers, demonstrating the technique's potential for multiplexed assay.[22] However, aptamers have limited commercial availability for many protein targets, including periodontitis biomarkers. By contrast, antibodies are widely available and well-characterised, demonstrating high specificity and binding affinity for a wide array of proteins. In this study, the modification of SCoNE DNA assembly to synthesize antibody-probe DNA carriers was evaluated. The ability to incorporate antibodies would greatly enhance the applicability of the SCoNE DNA assembly method and broaden the scope of suitable disease diagnosis targets.

The antibody-DNA carrier structure synthesized in this study was intended for resistive-pulse sensing applications with nanopipettes. To develop a multiplexed assay with resistive-pulse sensing, multiple antibodies must be incorporated onto the same DNA strand. Not only this, but the assay performance of the DNA structure is dependent on the stability, binding affinity and functional integrity of the antibodies under nanopore sensing conditions. However, there is the potential for antibodies to become denatured, either during the conjugation process or on exposure to the high-salt electrolyte used in nanopore experiments. Therefore, the suitability of antibodies for this application was evaluated by determining $K_D$ both before and after DNA conjugation, as well as assessing stability and binding behaviour under SCoNE DNA assembly conditions.

## 3.2 AIMS AND OBJECTIVES

This work aimed to adapt the SCoNE DNA assembly method for use with antibody probes, and to build a functional antibody-DNA structure able to detect periodontitis biomarkers. This work was achieved with the following objectives:

1. Determine antibody-protein $K_D$ values of various periodontitis biomarker proteins with titration ELISA and evaluate suitability for translocation experiments.
2. Measure and compare $K_D$ of unmodified and DNA-conjugated antibodies and assess impact of conjugation on binding affinity.
3. Evaluate the effect of SCoNE DNA assembly conditions on antibody binding ability with comparative ELISA.
4. Synthesize, isolate and assess binding ability of a 3 kbp antibody-DNA structure, using the SCoNE DNA assembly method and comparative ELISA.

## 3.3 MATERIALS AND METHODS

All chemical reagents were purchased from Sigma-Aldrich (Merck Group, United States) unless otherwise stated.

### 3.3.1 TITRATION ELISA

$K_D$ for the protein-antibody interactions of six identified protein biomarkers for periodontitis were experimentally determined using a modified sandwich ELISA approach.[23] Titration ELISA experiments for protein PK utilised pre-coated well-plates and reagents from a M2-PK ELISA kit (CSB-E08377h, Cusabio, United States). The DuoSet ELISA Ancillary Reagent Kit (DY008B) and DuoSet ELISA Development kits (R&D Systems, Bio-Techne, United States) were used for the following proteins: A1-AGP (DY3694), HGF (DY294), MMP-8 (DY908), MMP-9 (DY911) and S100A8 (DY4570). Titration curves were obtained by expanding the protein concentration range of the standard curve, obtained by two-fold serial dilution. Details of maximum and minimum protein concentration for each titration curve can be found in Table 3.1. All other technical operating instructions provided by the manufacturer were followed, with each standard performed in duplicate. After the colour change reaction had been allowed to proceed for a minimum of 20 minutes, the reaction was stopped, and the light absorbance

signal of each well was measured by photometric quantification at 450 nm using an Infinite 200 PRO microplate reader (Tecan Trading AG, Switzerland).

| Protein | Minimum – Maximum Protein Concentration |
|---|---|
| A1-AGP | 0.5 – 150,000 pg/mL |
| HGF | 2.4 – 430,000 pg/mL |
| MMP-8 | 1.9 – 110,000 pg/mL |
| MMP-9 | 2.5 – 670,000 pg/mL |
| PK | 0.3 – 1,200 µg/mL |
| S100A8 | 5 – 150,000 pg/mL |

*Table 3.1: Range of protein concentrations for each respective titration curve.*

**Data Analysis**

The titration curves were then fitted to Equation 3.1, a non-linear regression algorithm developed by Eble, to obtain $K_D$ values.[23] The data analysis was carried out using OriginPro 2021 (OriginLab Corportation, United States).

$$S(L_t) = (S_{max} - S_{min}) \cdot \frac{(K_D + R_t + L_t) - \sqrt{(K_D + R_t + L_t)^2 - 4 \cdot R_t \cdot L_t}}{2 \cdot R_t} + S_{min} + B \cdot L_t \qquad (3.1)$$

This equation correlates the absorbance signal intensity at 450 nm ($S(L_t)$) with the concentration of added ligand ($L_t$). The titration curve is characterised by five parameters: the dissociation constant ($K_D$), concentration of immobilised receptor ($R_t$), maximum and minimum absorbance signal ($S_{max}$ and $S_{min}$) and finally the slope of the background signal ($B$). $B$ is a proportionality constant, which describes the nonspecific background signal that increases linearly with $L_t$.

### 3.3.2 Antibody Modification

The biotinylated HGF detection antibody stock solution (36 µg/mL) from the DuoSet ELISA kit was used for a sequence of conjugation and click-reactions to produce an antibody conjugated to a short, 60 bp dsDNA strand. DBCO-NHS-ester was initially dissolved in DMSO to prepare a 2.5 mM stock solution. The stock solution was further aliquoted and diluted to the working concentration of 50 µM with MilliQ water. Into 20 µL of antibody stock solution, 5 µL of DBCO-NHS-ester solution was added, and the conjugation reaction left to proceed overnight.

The short DNA strands were provided by Oliver Irving (Albrecht Group, University of Birmingham). Originally purchased from Integrated DNA Technologies (Danaher Corporation, USA), they had been modified with a reactive azide group. Details of the enzymatic modification procedure, DNA sequence and structure of the SAM azide-donor (AW-39, provided by the Neely Group, University of Birmingham) have been detailed in previous work by Oliver Irving (Thesis: Sterically Controlled Nuclease Enhanced DNA Assembly in Rapid Sepsis Diagnostics, Chapter 2).[24] For the final click-reaction, 2 µL of DNA (600 ng/µL) was added to the antibody-DBCO reaction mixture and the reaction allowed a minimum of two hours to proceed. This mixture was then made up to 2.5 mL with DuoSet Reagent Diluent and used directly in an ELISA as the detection antibody in a sandwich assay (working concentration 288 ng/mL). The titration curve of the DNA-antibody sample was generated following the procedure detailed previously (3.3.1), alongside the standard, unmodified antibody, for comparison.

### 3.3.3 Reaction Conditions and Antibody Extraction

**Temperature, Time and Salt Buffer Conditions**

Six different reaction conditions, intended to mimic conditions of a SCoNE assembly procedure, were each tested on 10 µL of HGF detection antibody stock solution. The conditions were as follows: incubation at 20 °C for 2 and 24 hours, incubation at 45 °C for 2 and 24 hours, incubation at 4 °C in a salt buffer solution for 24 hours, and a method of biotinylated antibody extraction using streptavidin beads. The incubation temperature was controlled using a Techne Prime Thermal Cycler (Techne, Bio-Techne). The salt buffer solution was a ready-made buffer containing 70 mM Tris-HCl, 10 mM $MgCl_2$ and 5 mM DTT (New England Biolabs), of which 10 µL was added to the 10 µL antibody solution. Dynabeads™ MyOne™ Streptavidin C1 (Invitrogen, ThermoFisher) were used to test antibody extraction with a method used previously for isolation of aptamer-DNA structures. [22]

**Extraction with Ethanol**

For extraction, the 10 µL antibody sample was added to 70 µL of streptavidin beads and placed on a shaker at room temperature for 10 minutes. The beads were then separated from the solution with magnets for 3 minutes, the solution removed, and washed with 200 µL of 80 % ethanol. The wash step was repeated twice, and the beads allowed to dry in air for 5 minutes.

Following this, 50 µL of nuclease free water was added to the beads and incubated for 10 minutes. The beads were again separated from the solution with magnets for 3 minutes, and the supernatant collected.

**Limited Concentration Range ELISA**

All of the antibody samples were diluted with DuoSet Reagent Diluent to the working concentration of 200 ng/mL and used as the detection antibody in a sandwich ELISA. The standard curve had the following HGF protein concentrations: 4000, 2000, 1000 and 500 pg/mL. Each antibody sample was incubated in a well containing 4000 pg/mL HGF, and the resulting signal compared to the standard curve to determine any detrimental impact on antibody binding ability.

### 3.3.4 SCoNE Assembly of Antibody-DNA Structures

SCoNE DNA assembly is a method to build DNA carriers containing multiple antigen-binding probes. Previous work has tested the method using aptamers, and the synthesis can be broken down into four steps: conjugation, enzymatic modification, click-reaction, and Gibson assembly, as outlined in Figure 3.4. The DNA carrier in this experiment contained three long DNA strands and two short DNA strands, conjugated to HGF antibodies, to give a DNA carrier approximately 3.5 kbp in length.

Short, 60 bp DNA strands (600 ng/µL) were purchased from Integrated DNA Technologies (Danaher Corporation, USA). Longer, 1000 bp DNA strands (70 ng/µL) were purchased from Geneart (Sigma-Aldrich, Merck Group, Germany). Details of the DNA sequences, linearisation, and PCR amplification can be found in reference 23, chapter 2. All enzymes, buffers and nuclease free water were purchased from New England BioLabs (USA).

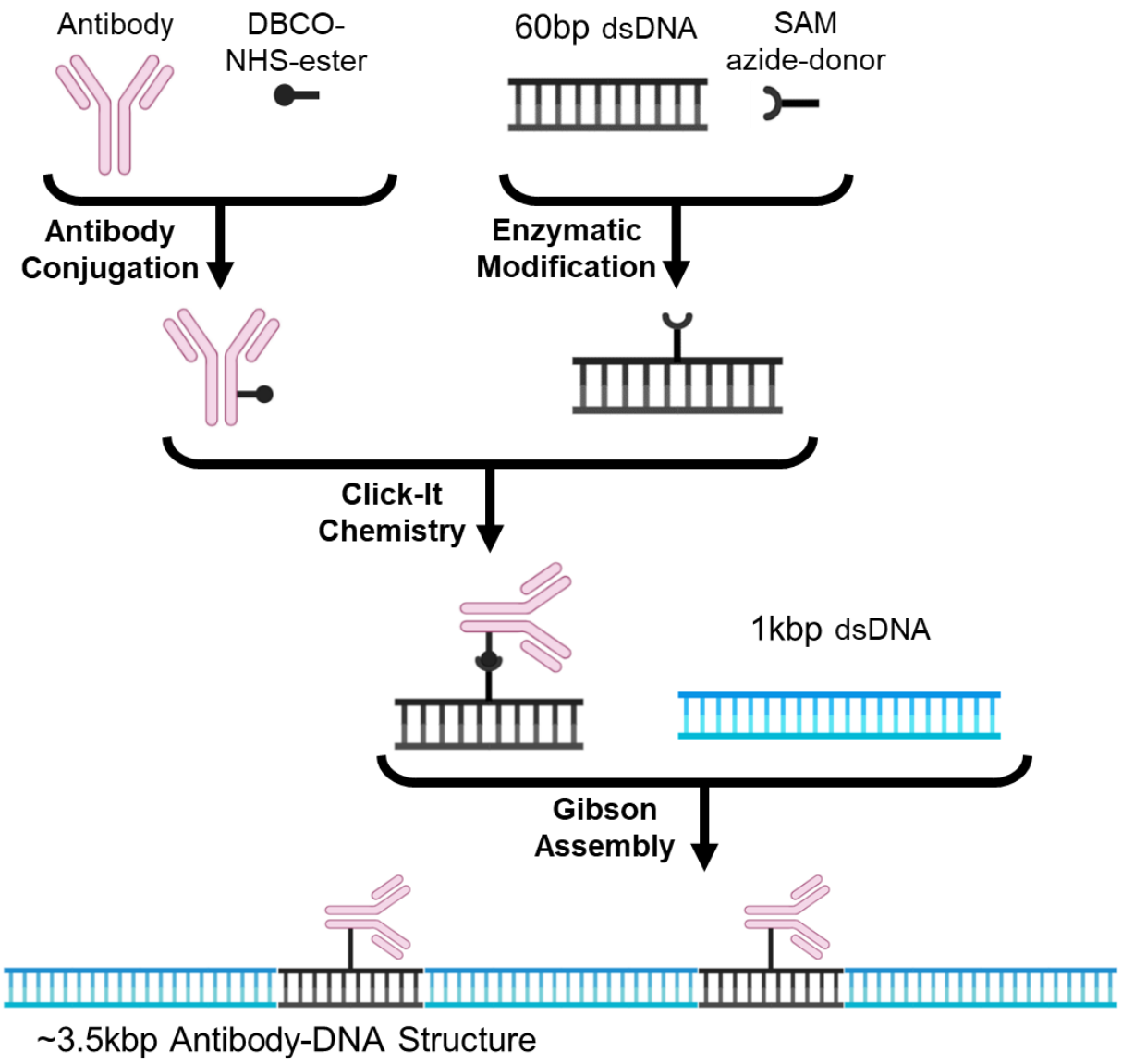


*Figure 3.4: Reaction scheme of a representative DNA carrier-strand synthesis using SCoNE DNA assembly. The reaction consists of four reaction steps; antibody conjugation with DBCO-NHS-ester, enzymatic modification with a modified SAM azide-group donor and 60 bp dsDNA probe strand, click-chemistry between the DBCO-moiety on the antibody and azide group on the DNA, and finally, Gibson assembly of the antibody-conjugated DNA strands with longer, spacer strands of 1 kbp dsDNA. Note, not-to-scale; final structure DNA length and width is approx. 1.2 µm and 2 nm, respectively, and antibodies are approx. 9 nm in size.*

**Antibody Conjugation**

To conjugate the antibody with DBCO-NHS-ester, 2 µL of HGF detection antibody (R&D Systems, Bio-Techne, USA) was added to 18 µL of 50 mM aqueous DBCO-NHS-ester. The mixture was incubated at 20 °C overnight.

**Enzymatic Modification**

To introduce an azide functional group onto the short DNA strands via enzymatic modification, the following reagents were added to a PCR vial and gently mixed: 15.5 µL nuclease free water, 2 µL cutsmart buffer, 1 µL SAM molecule modified with azide donor (AW-39, provided by the Neely Group, University of Birmingham), 1 µL 60 bp DNA strand (600 ng/µL) and 0.5 µL M.Taq1 enzyme. The reaction was heated to 45 °C for 1.5 hours, after which time 0.5 µL Proteinase K was added and the reaction further heated to 50 °C for 1 hour. The azide-functionalised DNA strands were isolated using the GenElute™ PCR Clean-Up Kit (Sigma-Aldrich, Merck Group, Germany), following the technical instructions from the manufacturer.

**Click-Reaction**

The azide-DNA strands were then reacted with the DBCO-moiety conjugated to the antibody, to chemically link the two components. The reaction mixture, 4 µL of the azide-DNA strand and 2 µL of the DBCO-antibody conjugate, was incubated overnight at 20 °C.

**Gibson Assembly**

The full DNA construct was created via Gibson assembly. The following reagents were added to a PCR vial and heated to 45 °C for 2 hours: 2 µL of each long DNA strand (70 ng/µL), 2 µL of each short DNA strand (with chemically linked antibody), 10 µL of Gibson Assembly MasterMix™ and 10 µL nuclease free water.

**Gel Electrophoresis**

The final product was isolated by gel electrophoresis, using a 1 wt. % agarose gel, at 75 V for 45 minutes. The gel was then stained with 1X GelRed dye and imaged with an AlphaImager Gel Imaging System (Protein Simple, Bio-Techne, USA) under UV illumination.

For comparison, equivalent 3 kbp aptamer-DNA structures were provided by Oliver Irving, synthesis details can be found in reference 23, chapter 2.

### 3.3.5 ANTIBODY ISOLATION METHODS

**Streptavidin Beads**

Sample isolation was further tested with streptavidin beads (Dynabeads™ MyOne™ Streptavidin C1, Invitrogen, ThermoFisher, USA), using biotinylated HGF detection antibodies from the stock solution (with no initial modification) and two different extraction methods.

The first protocol was provided by the manufacturer for nucleic acid extraction. To wash the beads, 50 µL of streptavidin beads were resuspended in 1 mL of washing buffer (5 mM Tris-HCL, 0.5 mM EDTA, 1 M NaCl) in an Eppendorf tube. The tube was placed on the magnet for 1 minute and the supernatant discarded. The washing step was repeated twice, for a total of three washes. To immobilise the sample, the washed beads were resuspended in 100 µL of 1X binding and washing (B&W) buffer (10 mM Tris-HCl, 1 mM EDTA, 2 M NaCl) to give a concentration of 5 µg/µL. 100 µL of biotinylated HGF detection antibody (36 µg/mL, R&D Systems, Bio-Techne, USA) was added to the tube and incubated on a shaker, at room temperature, for 15 minutes. The beads were separated from the solution with magnets for 3 minutes, and the solution removed. The beads were washed 3 times with 1X B&W buffer. The beads were resuspended with 100 µL of elution buffer (0.1 M glycine) and the solution separated from the beads. The extracted solution was immediately transferred into 10 µL of neutralisation buffer (1 M Tris solution).

The second protocol tested with streptavidin beads was specifically for antibody extraction. This method was identical to the nucleic acid method, barring a different wash buffer (PBS buffer, pH 7.4), an incubation time of 30 minutes and 4 wash steps using PBS buffer.

**Adapted PCR Clean-Up Protocol**

Two alternative approaches to isolate DNA-antibody conjugates (as described in 3.2) were tried. The first utilised the GenElute™ PCR Clean-Up Kit (Sigma-Aldrich, Merck Group, Germany) and an adapted protocol. To prepare the column, 0.5 mL of the provided column preparation solution was added to a mini spin column and centrifuged (12,000 x g, 30 seconds), then the eluate discarded. Then, 0.5 mL of provided binding solution was added to the antibody-DNA mixture, centrifuged (13,000 x g, 1 minute) and the eluate discarded. The mini spin column was washed with a further 0.5 mL of binding buffer (13,000 x g, 1 minute) and the eluate discarded. The wash step was repeated twice, for a total of three washes. The column

was emptied (13,000 x g for 2 minutes), and both the eluate and collection tube discarded. The DNA-antibody sample was eluted with 50 µL of water three times (13,000 x g, 1 minute each), to give approximately 150 µL of product solution.

**Molecular Weight Cut-Off Filters**

The second alternative approach to isolate DNA-antibody conjugates required molecular weight cut-off (MWCO) filters (Amicon® Ultra 30K device, Millipore, Merck Group, USA). The sample was added to the filter, spun in a centrifuge (13,000 x g, 10 minutes) and the eluate discarded. The filter was then washed with 0.5 mL TE buffer (13,000 x g, 10 minutes), the eluate discarded, and the wash step repeated twice. To recover the sample, the filter was inserted upside down into a clean microcentrifuge tube for a reverse spin (1,000 x g, 2 minutes), and the filtrate stored in the centrifuge tube.

**Limited Concentration Range ELISA**

All samples were diluted with DuoSet Reagent Diluent to the working concentration of 200 ng/mL and used as detection antibody in a sandwich ELISA. The standard curve had the following HGF protein concentrations: 8000, 4000, 2000, 1000, 500, 250 and 125 pg/mL.

## 3.4 RESULTS AND DISCUSSION

### 3.4.1 ANTIBODY SELECTION FOR DNA ASSEMBLY

In this work, the antigen targets were chosen from a list of proteins that were found to be present in periodontitis patient saliva, and hence a strong indicator for a positive periodontitis diagnosis.[25,26] The proteins studied were alpha-1 acid glycoprotein (α1-AGP), hepatocyte growth factor (HGF), matrix metalloproteinase-8 (MMP8), matrix metalloproteinase-9 (MMP9), pyruvate kinase (PK) and S100 calcium-binding protein A8 (S100A8).

The suitability of each antibody-antigen pair for resistive-pulse sensing was evaluated with titration ELISA (method detailed in Section 3.1). The titration curves for each of the six proteins studied are displayed in Figure 3.5.

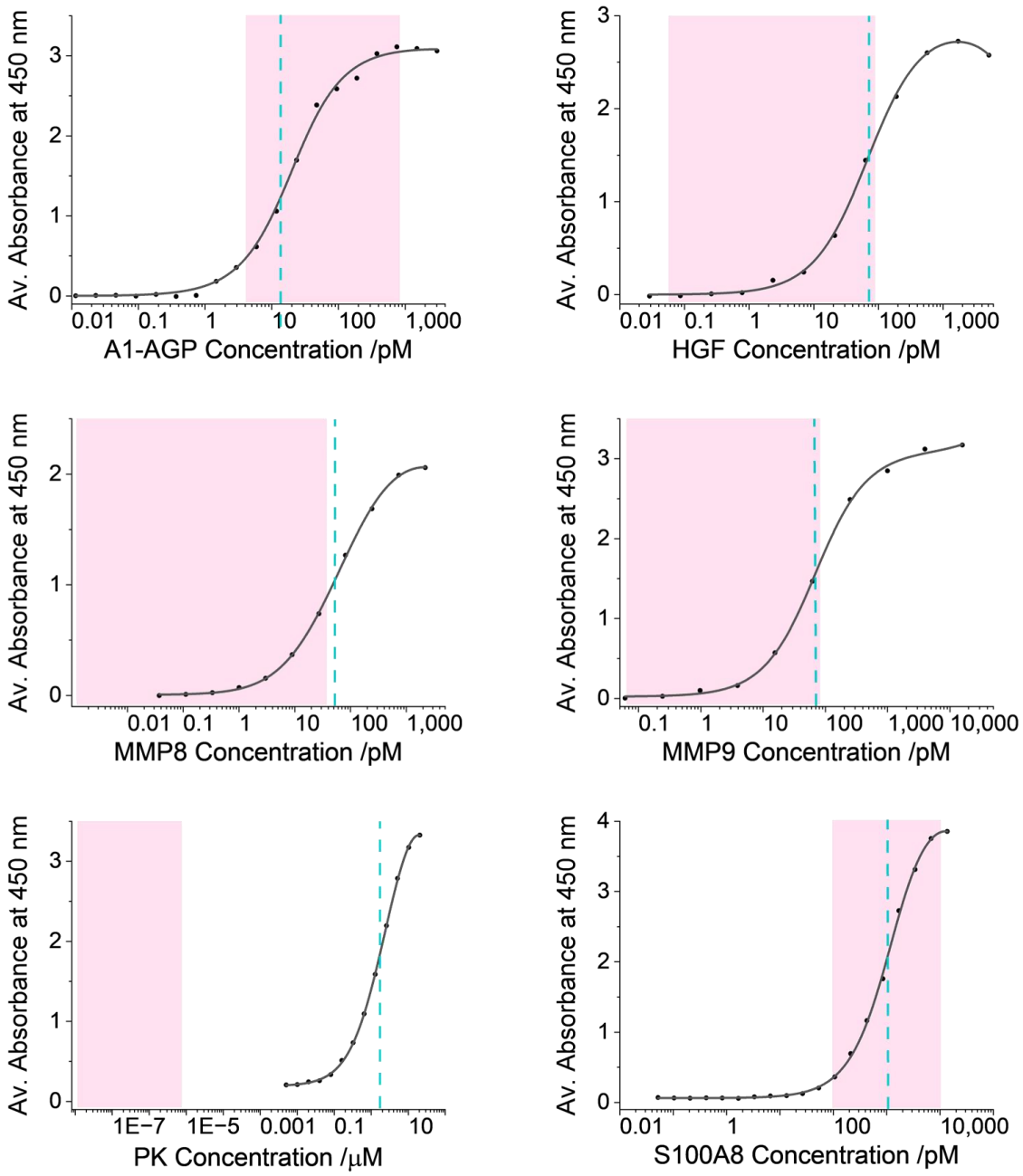


*Figure 3.5: Titration curves of ELISA absorbance signal against protein concentration for protein-antibody pairs α1-AGP, HGF, MMP8, MMP9, PK and S100A8, shown here with the black line. The experimentally determined $K_D$ value is indicated by the dashed blue line, and the magenta box highlights the expected protein concentration range in clinical settings as found in periodontitis patient saliva samples.*

The aim of this experiment was to determine $K_D$ values for each antibody-protein pair and evaluate their suitability for protein detection. In particular, the binding affinity must be

appropriate for detecting clinically relevant protein concentrations, as previously determined by mass spectrometry of periodontitis patient saliva.

The suitability of $K_D$ values in a diagnostic context depends on its position relative to the clinical concentration range of the target protein. Optimal sensitivity is achieved when the $K_D$ lies within this range, as the antibody's binding response (and therefore the signal change) is steepest near its $K_D$. This enables small variations in analyte concentration to produce measurable differences in assay output, allowing accurate quantification. Conversely, when $K_D$ is significantly above the target concentration range, binding is minimal under physiological conditions, resulting in poor signal response and reduced diagnostic utility. Therefore, for accurate quantification, the halfway point of the titration curve (corresponding to $K_D$) must align or have significant overlap with the clinically relevant concentration range.

The results show that antibodies targeting α1-AGP and S100A8 exhibited the most favourable overlap with the protein concentration ranges typically observed in periodontitis patient saliva. The binding affinities of these antibodies were such that the midpoint of their titration curves (and calculated $K_D$) corresponded well with the concentration range expected in clinical samples. Such overlap would be expected to enable sensitive quantification of these proteins.

Considering next HGF and MMP-9, the alignment of $K_D$ with the target concentration range is acceptable, but not as optimal as the overlap of α1-AGP and S100A8. The complex formation signal would be distinguishable between average and maximum protein concentrations. However, for below-average to minimum protein concentrations, the reduced signal response would mean less sensitive quantification. In a multiplexed assay, HGF and MMP-9 proteins would not be measured with equal sensitivity across the entire concentration range.

Finally, PK and MMP-8 antibodies demonstrated poor suitability, as $K_D$ values exceeded the maximum protein concentration found in patients. Signal response due to complex formation would be incredibly limited over the clinically relevant concentration range, and therefore these antibody-protein pairs are not suitable for the intended application.

**Analyte Concentration and Protein Size in Resistive-Pulse Sensing**

In the context of resistive-pulse sensing with nanopipettes, several practical considerations must be considered to allow effective detection of target proteins. This includes the concentration of probe DNA carrier structures, the detection sensitivity required, and the size of the protein relative to the antibody.

The concentration of probe DNA carrier structures in translocation experiments must be carefully balanced. High concentrations of DNA carriers can lead to pore clogging, and due to structure design, this places an inherent limit on the concentration of antibodies that can be present in solution. Furthermore, a large excess of unbound-probe events can swamp the data and under-report protein concentrations. On the other hand, if DNA concentration is too low, the formation of antibody-protein complexes will be saturated, and the protein concentration over-reported. The experimentally determined $K_D$ values for each antibody-antigen complex is displayed in Figure 3.6.

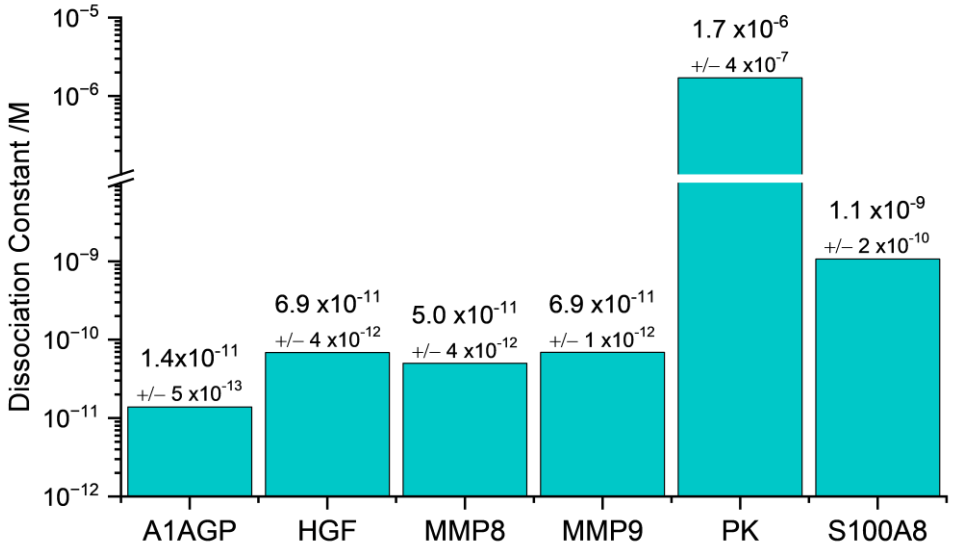


*Figure 3.6: Experimentally determined $K_D$ values (± standard error, owing to log scale) for the following antibody-protein pairs: α1-AGP, HGF, MMP8, MMP9, PK and S100A8.*

For optimal event recording during DNA translocation experiments, a DNA carrier concentration of 300 pM is typically chosen. This concentration allows for a sufficient number of translocation events to be recorded within a reasonable timeframe, whilst avoiding issues

like pore-clogging. As such, proteins with high $K_D$ in the micromolar and nanomolar range, namely PK and S100A8, are unsuitable analytes for this application. Complex formation for these proteins would occur at high analyte concentrations, above 300 pM. Therefore, the likelihood of detecting a sufficient number of bound protein events over the course of an experiment would be greatly reduced.

Equally important is the size of the target protein relative to the antibody, which determines whether a bound protein will generate a distinguishable signal. Small proteins may not produce a modulation in current sufficiently large enough to be detected and distinguished from background noise. Furthermore, the blockage events for bound or unbound states must be distinguishable from one another. With an approximate molecular weight of 80 kDa, HGF is the largest of the six proteins studied here. Relative to the size of an antibody (typically 150 kDa), HGF is the protein most suitable for further study, as it is expected to produce the most distinguishable signal between bound and unbound states.

With these considerations, HGF was chosen for further investigation owing to its larger size and the practicalities of DNA carrier concentration and protein detection.

### 3.4.2 Effect of Antibody Modification on Dissociation Constant

Titration ELISAs were performed with two antibody samples; an unmodified antibody, and an identical antibody conjugated to a short (60 bp) dsDNA strand. The antibody was conjugated to the DNA strand by following the antibody conjugation, DNA enzymatic modification and click-chemistry reaction steps, as outlined in section 3.3.4. The $K_D$ values for each sample were compared to determine the effect, if any, of the conjugation reaction on antibody functionality. Results are shown in Figure 3.7.

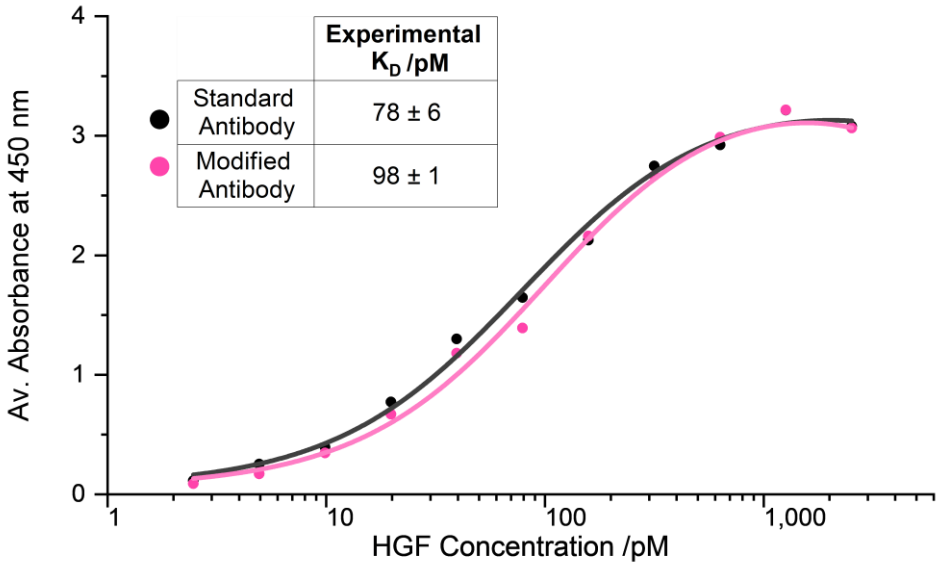


*Figure 3.7: ELISA titration curves, showing absorbance signal against HGF protein concentration, for a standard anti-HGF antibody (shown in black) and a modified, DNA-conjugated anti-HGF antibody (shown in magenta). Table inset shows experimentally determined $K_D$ values (± standard error).*

The titration ELISA results revealed that the $K_D$ values for the HGF antibodies were 78 ± 6 pM for the unmodified antibody and 98 ± 1 pM for the antibody conjugated to the 60 bp dsDNA strand. The relatively small difference in $K_D$ values between the two forms—approximately 20 pM—indicates that the conjugation of the antibody to the dsDNA did not have an overly detrimental effect on its binding affinity for HGF.

The small variation in $K_D$ values addresses potential concerns regarding antibody denaturation during the conjugation process. If conjugation caused significant structural changes to the binding region, a large increase in $K_D$ would be expected for the antibody-DNA sample. While the precise degree of labelling was not quantified in this study, the moderate shift in $K_D$ suggests a low degree of labelling and/or that labelling occurred predominantly at sites away from the binding region. Previous work in the literature has shown that excessive labelling, particularly at or near antigen-binding sites, can significantly reduce binding ability.[27] The slight change in $K_D$ observed here therefore supports the conclusion that the antibody retained functional integrity after conjugation and in the presence of dsDNA.

### 3.4.3 Stability of Antibodies Under SCoNE DNA Assembly Conditions

The potential impact of SCoNE DNA assembly on HGF antibody stability and binding ability was studied with a series of comparative ELISAs. Aliquots of antibody stock were subjected to conditions intended to mimic each step of the synthesis process, including conjugation, click-chemistry, and Gibson assembly. The conditions tested included varying temperatures, salt buffer exposure, and an ethanol-based extraction method. The percentage of HGF bound for each sample relative to standard conditions is shown in Figure 3.8.

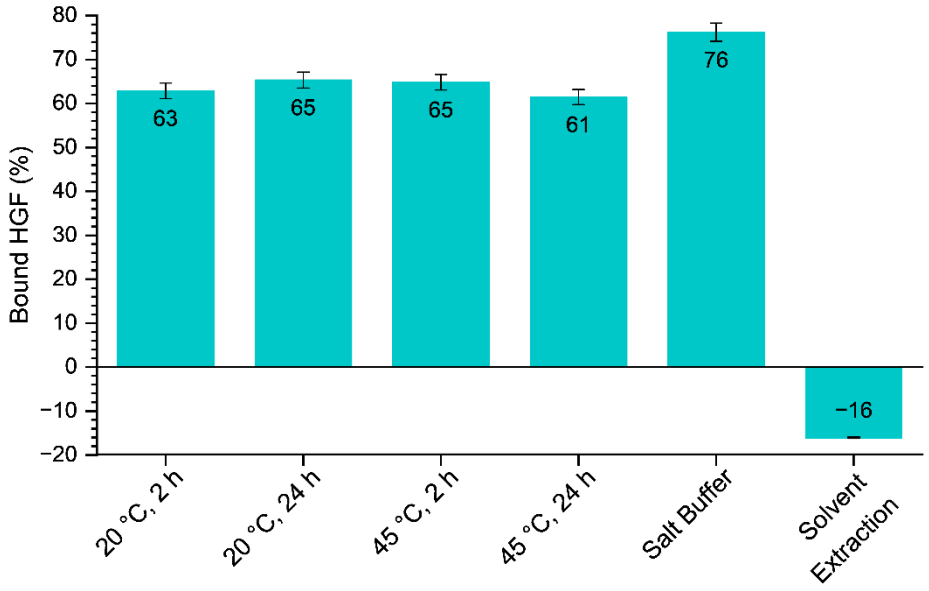


*Figure 3.8: Percentage of HGF protein bound by antibodies exposed to synthesis conditions, relative to the standard antibody sample, run under standard ELISA conditions. The following conditions were studied; 20 ºC and 45 ºC for both 2 and 24 hours, salt buffer solution, and ethanol solvent extraction.*

**Impact of Temperature and Time on Antibody Binding Efficiency**

Antibodies were subjected to temperatures of 20 °C and 45 °C for durations of 2 and 24 hours to replicate the conditions of the conjugation, click-chemistry reactions, and the higher-temperature Gibson assembly step. Relative to standard conditions, the binding efficiency of the antibody aliquots ranged from 60 – 65 % across all temperature and time conditions tested. The consistency in binding efficiency across different temperatures and durations suggests that these parameters (within the range tested) do not have a significant impact on binding ability.

These results suggest that the SCoNE DNA assembly protocol can be used without modification of these variables, optimised to increase product yield.

**Effect of Salt Buffer Solutions**

To mimic the high salt concentrations found in Gibson Assembly Master Mix (GAMM), an antibody aliquot was added to a salt buffer solution and held at 4 ºC for 24 hours. Relative to standard conditions, the antibody aliquot achieved a binding efficiency of 76 %. This suggests that the high salt concentration does not significantly reduce antibody binding ability, and the salt content of GAMM should not have a significantly detrimental effect.

If the decrease in binding ability has a cumulative effect for each reaction, it is estimated that approximately 30 % of the antibody's binding efficiency may be retained in the final product.

**Incompatibility of Ethanol Extraction**

The ethanol-based extraction method was demonstrated to be incompatible with antibodies, resulting in no detectable ELISA signal for extracted samples. Whilst ethanol-based extraction methods were effective for aptamer probe extraction,[22] they severely impact antibody stability. It is likely that the loss of binding ability is due to the disruption ethanol causes to the protein structure of antibodies. This finding highlights the importance of selecting appropriate extraction techniques for antibody-DNA structures.

**Implications for SCoNE Assembly**

The observed binding efficiencies suggest that, despite some degradation, the antibody aliquots retained a sufficient level of binding ability. Theoretically, the final antibody-DNA product should retain enough binding activity for practical use. However, some experimental parameters remain untested, such as the effect of GAMM enzymes on antibody stability.

In summary, ethanol extraction was found to be unsuitable for an antibody-DNA carrier, whilst reaction parameters such as salt solution, temperature and reaction time resulted in similar levels of antibody degradation, but functionality was still maintained.

### 3.4.4 Synthesis of Antibody-DNA Structures Using SCoNE DNA Assembly

The SCoNE DNA assembly method was tested with HGF antibody probes, in place of previously tested aptamers. A 3 kbp DNA structure was designed to include two identical antibody probes placed between three 1 kbp DNA spacer strands. The length of the final structure was confirmed by gel electrophoresis imaging and compared with an equivalent aptamer-DNA structure (Figure 3.9). This confirms that a full DNA structure can be built using antibodies in the assembly process.

However, the gel image also revealed the presence of lighter weight bands. These bands are predominantly seen at 2 kbp, 1 kbp and 60 bp, resulting from unreacted reagents and side products (indicative of incomplete reactions) remaining in the sample solution. The band at 2 kbp is attributed to side products, the band at 1 kbp to unreacted spacer DNA strands, and the band at 60 bp to unreacted probe DNA strands.

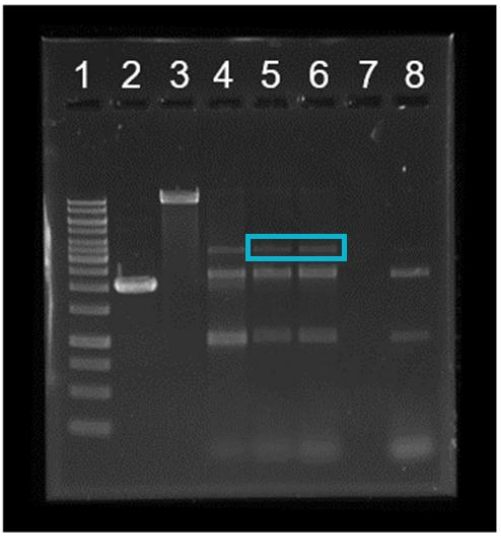


| Lane | Sample |
|---|---|
| 1 | 1 kbp Ladder |
| 2 | 2 kbp dsDNA |
| 3 | 10 kbp dsDNA |
| 4 | Aptamer-DNA Structure |
| 5 | Antibody-DNA Structure |
| 6 | Antibody-DNA Structure |
| 7 | Empty |
| 8 | Unreacted Mixture |

*Antibody-DNA Structure*

*Figure 3.9: Agarose gel electrophoresis image, with the illustrated antibody-DNA product highlighted by the blue box. Within each lane; 1 – 1 kbp DNA ladder, 2 – 2 kbp dsDNA, 3 – 10 kbp dsDNA, 4 – final aptamer reaction mixture, 5 & 6 – final antibody reaction mixture, 7 – empty, 8 – unreacted reagent mixture.*

However, the successful incorporation of antibodies into the DNA structure is currently inferred only from the gel migration pattern, which matches the expected molecular weight of the assembled product and is consistent with aptamer-based controls. This indirect evidence does not confirm the presence of antibodies in the final construct. To directly verify antibody incorporation, further validation using protein-specific techniques such as Western blotting or dot blotting with anti-IgG antibodies would be required. While direct confirmation of antibody incorporation using blotting techniques would have been valuable, such experiments were not feasible within the constraints of available time and expertise. Future studies are encouraged to include these methods to validate the final structure and presence of antibodies.

These results highlight the importance of finding a suitable extraction technique to isolate the antibody-DNA structure from the unreacted DNA fragments and antibody-containing side products. Furthermore, accurate quantification of the structure is necessary for ELISA, in order to evaluate the binding ability of the pure final product.

### 3.4.5 Evaluation of Antibody-DNA Product Isolation Techniques

As the isolation technique recommended in the SCoNE DNA assembly protocol, ethanol extraction, proved unsuitable for antibodies, different extraction methods were evaluated. Three alternative approaches were tested: an adapted polymerase chain reaction (PCR) clean-up protocol, molecular weight cut-off (MWCO) filters, and streptavidin bead extraction using both nucleic acid and antibody protocols. The experimental workflow is shown in Figure 3.10.

Following sample extraction, the final product was collected and antibody yield determined with a comparative ELISA. In the ELISA, the presence of functional antibody was detected via binding to immobilised HGF protein, followed by HRP-conjugated to the biotin label and subsequent 3,3′,5,5′-Tetramethylbenzidine (TMB) substrate conversion, producing a quantifiable colour change at 450 nm. The ELISA measured the retention of antigen-binding capacity of the antibody component in the product. However, it did not distinguish between (ay potentially remaining) free and DNA-bound antibody. Therefore, the presence of functional antibody signal in the ELISA suggests that at least some antibody remained active, but does not on its own confirm successful conjugation to DNA. If antibody yield was high, the colour intensity and hence absorbance signal from the ELISA would be expected to be similar to that of the standard antibody stock solution. If extracted antibody yield was low, the ELISA absorbance signal for that sample would be expected to be lower than that of the standard.

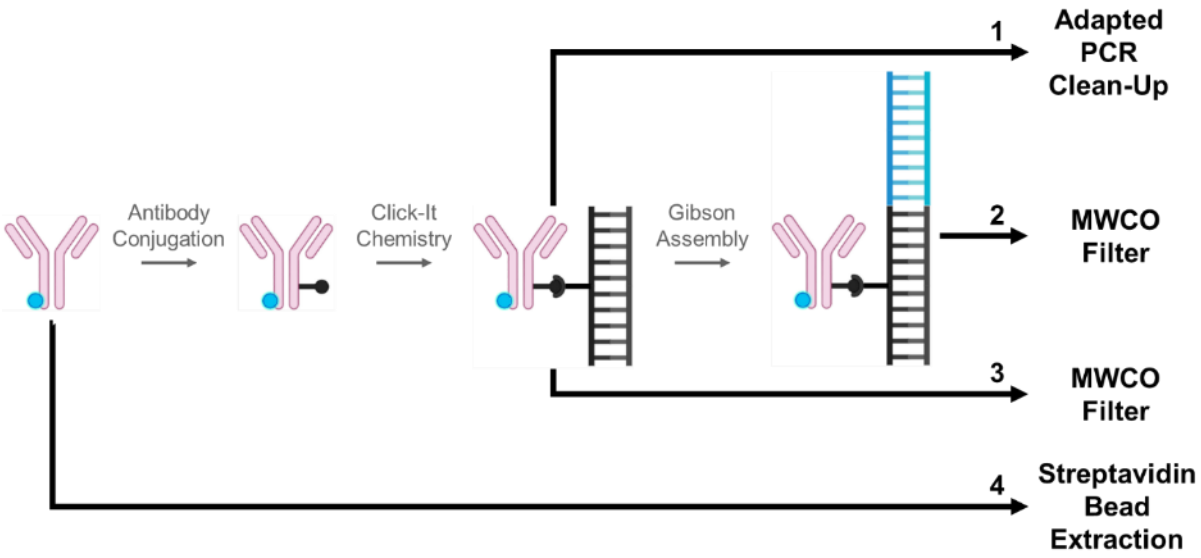


*Figure 3.10: Schematic representation of biotinylated antibody/DNA reaction steps preceding each extraction method. Experiment 1; conjugation, click-chemistry, adapted PCR clean-up. Experiment 2; conjugation, click-chemistry, Gibson assembly, MWCO filtration. Experiment 3; conjugation, click-chemistry, MWCO filtration. Experiment 4; no reaction steps, streptavidin bead extraction.*

**Adapted PCR Clean-Up Protocol**

Initially, an adapted PCR clean-up protocol was tried to exploit the strong negative charge of DNA for isolation, results shown in Figure 3.11. The method was modified to exclude ethanol washes, which are known to denature biomolecules, particularly proteins. The intent was to selectively isolate antibodies bound to DNA and remove excess biotinylated antibodies.

Although previous results showed that high salt concentrations alone did not impair antibody function, the binding buffer used here also included the chaotrope guanidinium hydrochloride to facilitate DNA binding to the silica column. These chaotropes are known to disrupt hydration shells and can denature proteins. Therefore, the absence of a detectable ELISA signal may be attributed to denaturation of the antibody during the extraction process. It remains unclear whether any product was successfully recovered or if degradation occurred during the conjugation or assembly steps.

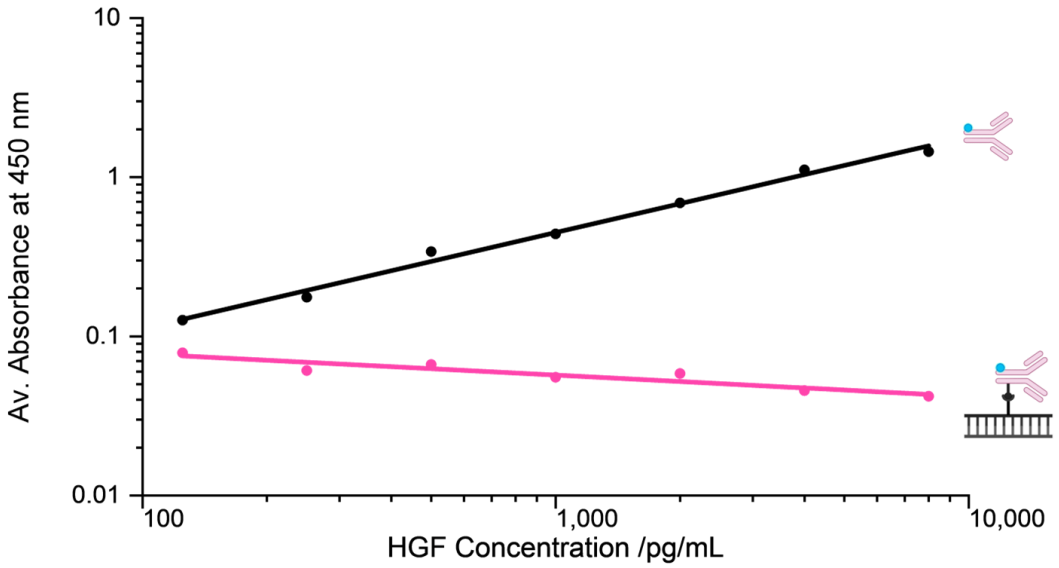


*Figure 3.11: ELISA absorbance signal at varying HGF protein concentrations for experiment 1. The black line shows the absorbance signal of the antibody standard, the magenta line shows the signal from the antibody-DNA structure after adapted PCR extraction (experiment 1). The near zero signal with no change shows that either no product was extracted (hence no antibodies present), or the antibodies were denatured.*

**Molecular Weight Cut-Off Filters**

The second approach tested MWCO filters to separate the antibody-DNA construct from unreacted reagents. However, the unreacted antibodies were too large to be effectively removed by the MWCO filters, leading to their continued presence in the solution. Unfortunately, experiments could not be performed with a higher value MWCO filter owing to time constraints, but should be attempted in future experiments. As such, they would be expected to contribute even a weak signal to the filtered sample. Despite this, no colour absorbance signal was detected in the ELISA for experiment 2 (see Figure 3.12), which included an additional step of Gibson assembly. One possible explanation is that some enzymes were retained by the filter, and as such may have interfered with the subsequent ELISA.

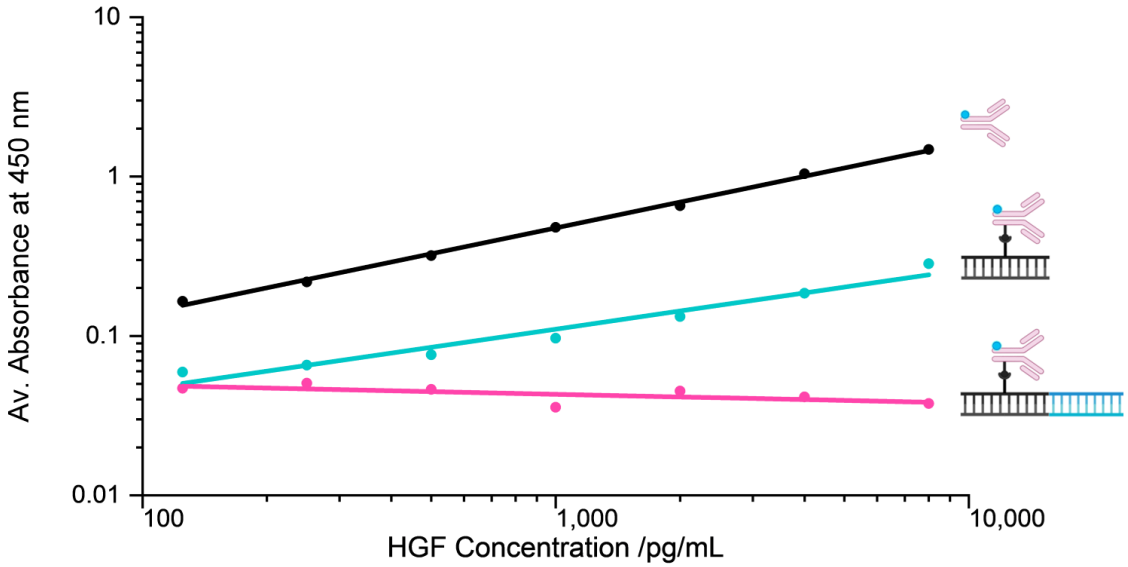


*Figure 3.12: ELISA absorbance signal at varying HGF protein concentrations for experiments 2 and 3. The black line shows the absorbance signal of the antibody standard, the magenta line shows the signal from the MWCO filtration product after Gibson assembly (experiment 2), and the blue line shows the signal from the MWCO filtration product without a Gibson assembly step (experiment 3). For experiment three, the near zero signal with no change shows that either no product was extracted (hence no antibodies present), or the antibodies were denatured.*

By contrast, the sample from experiment 3, which did not undergo the Gibson assembly step, showed a less intense but detectable ELISA signal, suggesting that some functional antibodies were retained, and the MWCO filter was not the cause of antibody denaturation. It is also possible that steric hindrance from the larger DNA-conjugated structure (additional Gibson assembly step) impeded the antibody's ability to bind to surface-immobilised antigen, thereby reducing ELISA signal despite the presence of the conjugate. Future experiments could explore alternative detection formats or assess binding kinetics directly (with isothermal titration calorimetry, for example).

**Streptavidin Bead Extraction**

The final extraction method tested streptavidin beads with the stock solution of detection antibodies. As such, these antibodies contained a biotin tag to bind to the streptavidin, and did not undergo any further modification or Gibson assembly step. Two protocols were tested: one designed for nucleic acid extraction and another for antibody extraction. The nucleic acid

extraction protocol yielded no UV-Vis signal from nanodrop quantification, indicating ineffective isolation of antibodies. UV-Vis analysis was employed as an initial qualitative check. However, the concentration of antibodies in these samples may have been below the detection limit of the instrument, and the lack of signal does not conclusively rule out the presence of product.

The antibody extraction protocol produced a low UV-Vis signal, therefore warranting an ELISA test (see Figure 3.13). The resulting absorbance signal was higher at low protein concentrations, which is unexpected. Despite the attempt to use a higher concentration of antibodies to enhance the signal, the streptavidin bead extraction method proved to be too low yielding to provide enough data for meaningful analysis.

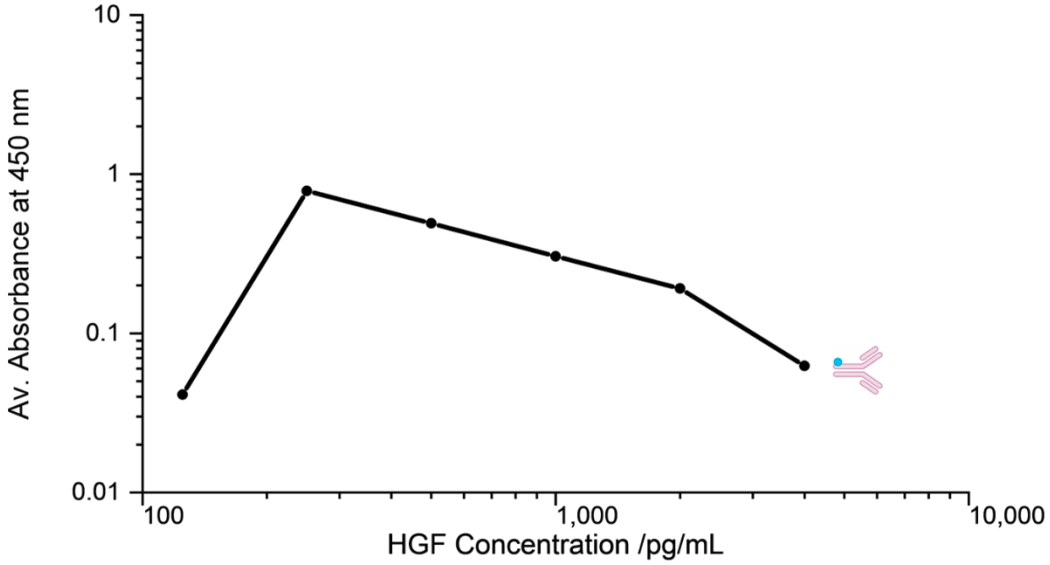


*Figure 3.13: ELISA absorbance signal at varying HGF protein concentrations for experiment 4. The black line shows the absorbance signal for an unreacted antibody after extraction with streptavidin beads, using the antibody extraction method. The irregular signal suggests an inhomogeneous solution, and overall a low product yield.*

These findings emphasize the need for further optimisation of extraction and assembly protocols to ensure the successful isolation and functional assessment of antibody-DNA constructs. These results also highlight the potential unsuitability of the SCoNE DNA assembly method overall with antibody probes. While ELISA suggested a lack of functional binding, this does not conclusively indicate a failure in construct formation. It is possible that the antibody-

DNA conjugate was successfully formed but sterically prevented from binding to the antigen. Nanopore sensing was considered but not performed in this set of experiments; this technique could be used in future studies to investigate construct integrity.

## 3.5 CONCLUSIONS & FUTURE WORK

The aim of this study was to integrate antibody probes into the SCoNE DNA assembly method, focussing on their potential for application with resistive-pulse sensing.

**Conclusions**

1. **Titration ELISA Experiments:** The titration ELISA experiments demonstrated that the concentration range of the antibody-antigen complex binding response and its overlap with the expected protein concentrations in patient saliva were important. Proteins such as pyruvate kinase (PK) and matrix metalloproteinase-8 (MMP8) were found to be unsuitable due to their low overlap with disease-relevant protein concentrations. Among the remaining proteins, α1-acid glycoprotein (A1-AGP), S100 calcium-binding protein A8 (S100A8), hepatocyte growth factor (HGF), and matrix metalloproteinase-9 (MMP9), HGF was selected for further study based on its favourable size (approx. 80 kDa), suitable $K_D$ value (78 ± 6 pM), and good overlap with disease-relevant concentrations.

2. **Antibody Modification:** Only a small increase in $K_D$ was observed after conjugation of DNA to the antibody (from 78 ± 6 pM to 98 ± 1 pM). This result suggested that the conjugation reactions do not significantly reduce the binding ability of the modified antibodies.

3. **SCoNE DNA Assembly Conditions:** The stability of HGF antibodies under SCoNE DNA assembly conditions was assessed by exposing them to various temperatures, salt buffer solutions, and an ethanol-based extraction method. Exposure to moderate temperatures led to a consistent reduction in binding efficiency of 60-65% of that achieved under standard conditions. This demonstrated that the temperature and duration of reaction steps do not require further optimisation. Exposure to high salt concentrations at 4°C resulted in a relative binding efficiency of 76%. It was estimated that only 30% of the antibody's binding ability might be retained after the full SCoNE DNA assembly process. The ethanol extraction method proved unsuitable, resulting in no detectable ELISA signal.

4. **Synthesis of a 3 kbp Antibody-DNA Structure:** The successful synthesis of a 3 kbp antibody-DNA structure demonstrated that the SCoNE method can be effectively applied to antibodies, similar to previously tested aptamer-DNA constructs. Gel electrophoresis confirmed the expected length of the structure at 3 kbp. Bands resulting from partially reacted constructs and unreacted DNA reagents were also seen. This demonstrates that the SCoNE method can use antibodies to make full-length construct, but probe functionality still needs to be tested.

5. **Product Extraction and Isolation Methods:** Attempts to extract and isolate the antibody-DNA construct using ethanol extraction, adapted PCR clean-up, MWCO filters, and streptavidin beads were mostly unsuccessful. The PCR clean-up protocol, suspected to have denatured the antibodies due to chaotropes, and the molecular weight filters, which could not effectively isolate the construct from excess antibodies, were inadequate. Streptavidin bead extraction methods were also low yielding. These findings highlight the impact GAMM enzymes may have on antibody stability. If found to be detrimental, the SCoNE DNA assembly method would be unsuitable for use with antibodies, limiting its applications.

**Future Work**

It is recommended that future work focus on several key areas to address the limitations raised by this study:

1. **Enhanced Isolation Methods:** The use High-Performance Liquid Chromatography (HPLC) is well-documented in the literature for the separation of biochemical molecules.[28-30] Whilst it is a more complex technique than those tested in this study, and would require additional method development, it could successfully isolate and quantify the antibody-DNA construct and allow for further crucial analysis.

2. **Titration Curve of the Full Construct:** A titration curve of the full antibody-DNA construct is necessary to determine its binding affinity and confirm the functionality of the structure. This would be necessary to assess its suitability for the intended application, and to determine if GAMM enzymes have a detrimental effect on antibody binding ability.

3. **Multi-Antibody Constructs:** Future experiments could study the synthesis of DNA carriers for multiplexed assay, with multiple target antigen-antibodies included on one DNA strand. This would allow the binding ability of multi-antibody constructs to be evaluated.
4. **Optimisation of Assembly Conditions:** Further optimisation of the SCoNE DNA assembly conditions will be necessary to improve antibody stability and the efficiency of DNA assembly.

While this study has made progress in synthesizing and testing antibody-DNA constructs with the SCoNE DNA assembly method, further improvements regarding product extraction will be necessary to further advance this work to practical applications; the proposals here aim to address these challenges and answer some of the questions raised throughout this work.

## 3.6 REFERENCES


1 R. Ren, S. Cai, X. Fang, X. Wang, Z. Zhang, M. Damiani, C. Hudlerova, A. Rosa, J. Hope, N. J. Cook, P. Gorelkin, A. Erofeev, P. Novak, A. Badhan, M. Crone, P. Freemont, G. P. Taylor, L. Tang, C. Edwards, A. Shevchuk, P. Cherepanov, Z. Luo, W. Tan, Y. Korchev, A. P. Ivanov and J. B. Edel, *Nat Commun*, 2023, **14**, 7362.

2 J. Y. Y. Sze, A. P. Ivanov, A. E. G. Cass and J. B. Edel, *Nat Commun*, 2017, **8**, 1552.

3 L. He, D. R. Tessier, K. Briggs, M. Tsangaris, M. Charron, E. M. McConnell, D. Lomovtsev and V. Tabard-Cossa, *Nat Commun*, 2021, **12**, 5348.

4 M. M. Ling, C. Ricks and P. Lea, *Expert Rev Mol Diagn*, 2007, **7**, 87–98.

5 C. Wu, T. J. Dougan and D. R. Walt, *ACS Nano*, 2022, **16**, 1025–1035.

6 C. Koch, B. Reilly-O'Donnell, R. Gutierrez, C. Lucarelli, F. S. Ng, J. Gorelik, A. P. Ivanov and J. B. Edel, *Nat Nanotechnol*, 2023, **18**, 1483–1491.

7 D. M. Rissin, C. W. Kan, T. G. Campbell, S. C. Howes, D. R. Fournier, L. Song, T. Piech, P. P. Patel, L. Chang, A. J. Rivnak, E. P. Ferrell, J. D. Randall, G. K. Provuncher, D. R. Walt and D. C. Duffy, *Nat. Biotechnol.*, 2010, **28**, 595–599.

8 S. Hosseini, P. Vázquez-Villegas, M. Rito-Palomares and S. O. Martinez-Chapa, in *Enzyme-linked Immunosorbent Assay (ELISA): From A to Z*, Springer Singapore, Singapore, 2018, pp. 67–115.

9 P. J. Tighe, R. R. Ryder, I. Todd and L. C. Fairclough, *Proteomics Clin Appl*, 2015, **9**, 406–422.

10 G. Lubec and L. Afjehi-Sadat, *Chem Rev*, 2007, **107**, 3568–3584.

11 W. He, M. You, W. Wan, F. Xu, F. Li and A. Li, *Trends Biotechnol*, 2018, **36**, 1127–1144.

12 M. Taba Jr., J. Kinney, A. S. Kim and W. V Giannobile, *Dental Clinics*, 2005, **49**, 551–571.

13 S. P. Barros, R. Williams, S. Offenbacher and T. Morelli, *Periodontol 2000*, 2016, **70**, 53–64.

14 S. Black, D. Phillips, J. W. Hickey, J. Kennedy-Darling, V. G. Venkataraaman, N. Samusik, Y. Goltsev, C. M. Schürch and G. P. Nolan, *Nat Protoc*, 2021, **16**, 3802–3835.

15 S. A. Kazane, D. Sok, E. H. Cho, M. L. Uson, P. Kuhn, P. G. Schultz and V. V Smider, *Proceedings of the National Academy of Sciences*, 2012, **109**, 3731–3736.

16 S. S. Agasti, M. Liong, V. M. Peterson, H. Lee and R. Weissleder, *J Am Chem Soc*, 2012, **134**, 18499–18502.

17 C. Koehler, P. F. Sauter, B. Klasen, C. Waldmann, S. Pektor, N. Bausbacher, E. A. Lemke and M. Miederer, *ACS Chem Biol*, 2023, **18**, 443–448.

18 H. Kawashima, *The Scientific World Journal*, 2014, **1**, 492061.

19 J. W. Marsh, K. Srinivasachar and D. M. Neville, in *Immunotoxins*, ed. A. E. Frankel, Springer US, Boston, MA, 1988, pp. 213–237.

20 R. M. Hoffmann, S. Mele, A. Cheung, D. Larcombe-Young, G. Bucaite, E. Sachouli, I. Zlatareva, H. O. J. Morad, R. Marlow, J. M. McDonnell, M. Figini, K. E. Lacy, A. J. N. Tutt, J. F. Spicer, D. E. Thurston, S. N. Karagiannis and S. Crescioli, *Sci Rep*, 2020, **10**, 8869.

21 P. Dennler, E. Fischer and R. Schibli, *MDPI*, 2015, **4**, 197-224.

22 O. J. Irving, L. Matthews, S. Coulthard, R. K. Neely, M. M. Grant and T. Albrecht, *ChemBioChem*, 2023, **24**, e202300361.

23 J. A. Eble, *J. Vis. Exp.*, 2018, **15**, 57334.

24 B. Oliver James Irving, *Sterically Controlled Nuclease Enhanced DNA Assembly in Rapid Sepsis Diagnostics*, 2022.

25 W. M. Sexton, Y. Lin, R. J. Kryscio, D. R. Dawson III, J. L. Ebersole and C. S. Miller, *J Clin Periodontol*, 2011, **38**, 434–441.

26 M. M. Grant, J. J. Taylor, K. Jaedicke, A. Creese, C. Gowland, B. Burke, K. Doudin, U. Patel, P. Weston, M. Milward, S. M. Bissett, H. J. Cooper, G. Kooijman, A. Rmaile, M. de Jager, P. M. Preshaw and I. L. C. Chapple, *J Clin Periodontol*, 2022, **49**, 622–632.

27 J. Wiener, D. Kokotek, S. Rosowski, H. Lickert and M. Meier, *Sci Rep*, 2020, **10**, 1457.

28 F. Sousa, V. M. F. Gonçalves and B. Sarmento, *J Pharm Biomed Anal*, 2017, **142**, 171–177.

29 G. A. Perry, J. D. Jackson, T. L. McDonald, D. A. Crouse and J. G. Sharp, *Prep Biochem*, 1984, **14**, 431–447.

30 D. Josić, K. Löster, R. Kuhl, F. Noll and J. Reusch, *Biol. Chem.*, 1991, **372**, 149–156.

# 4 CHARACTERISATION OF DNA TRANSLOCATION AS A REFERENCE FOR COMPLEX ANALYTES

## CONTENTS

# 4.1 INTRODUCTION

Applying a voltage bias between two electrodes immersed in an electrolyte solution causes an ion current to flow. This results in potential drops in solution and local electric fields in the cell. In a nanopore setup, a pore in the range of 1 – 100 nm restricts the ion current flow and the electric field lines converge towards the pore. This strong electric field can pull charged objects, like DNA, through the pore, simultaneously causing a change in the ion current. This ion current modulation is known as the translocation event and is the basis for resistive-pulse sensing.[1-4]

Detecting features of more complex analytes, such as DNA modified to have additional structural features like biomarker probes, can also be detected using nanopores.[5-10] Various modifications and additional binding along DNA strands have been studied in the literature. Some examples include direct protein binding,[5] biotin-streptavidin complexes,[6] single-stranded DNA (ssDNA) hybridisation[10] and DNA strand displacement.[9] Experiments such as these require not just careful consideration of experimental conditions, but also an understanding of the translocation process of DNA, to allow for the resulting subevents to be detected and effectively analysed.

## 4.1.1 DNA TRANSLOCATION MECHANISMS

### Entropic Effects and Confinement Regimes

As a DNA molecule enters a confined space (such as a nanopore channel), it loses the freedom to fluctuate and adopt random configurations. The loss of conformational entropy results in an energetic penalty, an entropic barrier. To continue moving through the channel, the DNA must overcome this entropic barrier. The change in entropy can itself act as a driving force for DNA translocation, even in the absence of an applied voltage.[11]

A theoretical model developed by Meng et al. analyses the movement of the leading end of a polymer chain (such as DNA) as it enters a finite-length nanochannel.[11] It was found that the entropy gradient along the channel generates a nearly constant force, that acts to pull the molecule forwards. Importantly, this entropic force was found to be dependent on the channel diameter, and increased as the channel diameter narrowed. It was found to be relatively independent of channel length and polymer length, supporting the theory that confinement drives translocation. The model also predicts a linear free energy profile within the channel, meaning the translocation driving force remains constant throughout.[11]

Two regimes can be used to describe the DNA structural response to confinement.[11] The de Gennes regime applies when the channel diameter is significantly larger than the DNA's persistence length (approximately 50 nm). In this case, DNA coils into a series of compressed blobs. The entropic cost arises from restricting the size and number of these blobs. The structural response transitions to the Odijk regime under strong confinement, where the channel diameter is much smaller than the persistence length (typically less than 10 nm). The DNA is constrained to follow the shape of the channel with limited bending, forcing it into an extended conformation. The greater degree of confinement results in a higher entropic barrier.[11] These regimes help explain why channel geometry, particularly pore diameter, has such a significant effect on the mechanisms and timescales of DNA translocation events.

**Electrophoretic Forces and Hydrodynamic Drag**

Whilst entropic effects govern passive translocation, most nanopore experiments apply an external voltage to actively drive DNA through the pore. Additional forces must be considered under these conditions, of most importance are the electrophoretic force and hydrodynamic drag, which are the dominant forces acting on the DNA molecule during translocation.[12]

The electrophoretic force arises from the interaction between the electric field and the negatively charged phosphate backbone of the DNA. Most of the voltage drop occurs across the nanopore due to its high resistance, producing a concentrated electric field that drives DNA along the pore axis. In nanopore translocation under an applied voltage, the strong electric field at the pore entrance exerts a force that rapidly overcomes the entropic barrier associated with uncoiling the DNA.[12]

Opposing this motion is hydrodynamic drag, which arises from the resistance of the electrolyte solution. This force is most significant within the confined geometry of the pore, and depends on the velocity of the DNA and the pore geometry. Outside the nanopore, drag is comparatively minor. Overall, DNA translocation with applied voltage is dominated by electrophoresis and drag forces, with entropic effects primarily effecting the initial capture step.[12]

Recent studies have shown that DNA translocation through asymmetric conical nanopores (where one end of the nanopore channel is wider than the other) introduces additional complexity to the translocation process.[13-16] There are two directions for translocation: forward translocation, where DNA moves from an open reservoir into the narrow confinement of the

nanopore, and reverse translocation, where DNA exits the nanopore and re-enters the bulk solution (Figure 4.1).

Bell et al. developed a hydrodynamic model describing this process.[13] The DNA was approximated as a straight cylinder within the pore itself, and they considered only aligned (straight) segments contributing significantly to the net drag, while coiled regions outside the pore have minimal effect. The electric field is modelled as strongest at the nanopore entrance and decays with distance. Inside the pore, it aligns with the nanopipette's axis of symmetry, applying a unidirectional force on the DNA. Again, the electric field outside of the pore is considered negligible.[13]

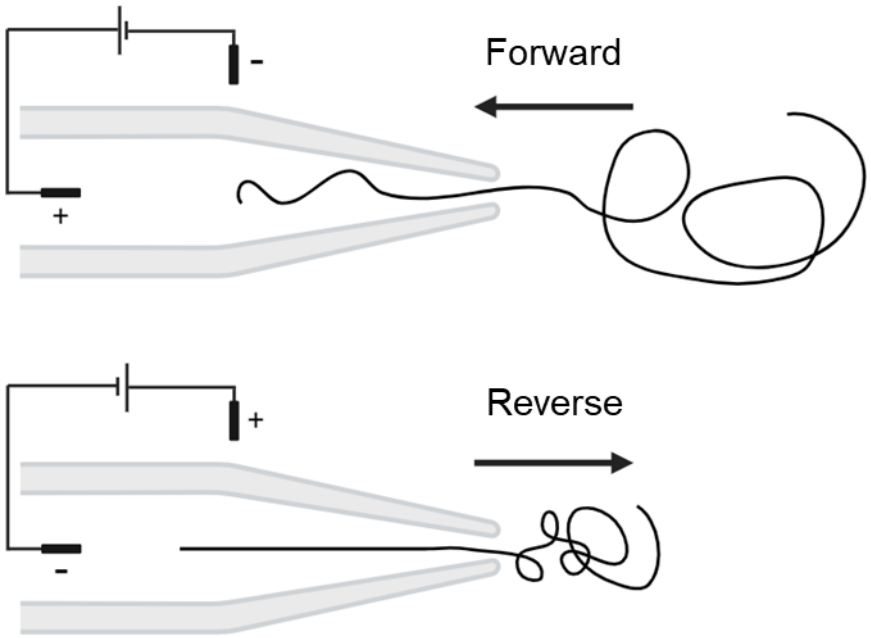


*Figure 4.1: Forward translocation occurs when DNA enters the nanopore from the open reservoir. Reverse translocation occurs when DNA exits the nanopore into the reservoir.*

The two dominant forces scale differently with distance. Hydrodynamic drag scales with an approximately $1/ln(x)$ relationship, while the electric force scales with approximately $1/x^2$. These scaling relationships show that the electric field is highly concentrated near the nanopore entrance, while hydrodynamic effects extend over a larger region.[13]

In forward translocation, it was described through the model that DNA may 'buckle' due to compressive forces. This means only a short leading section is considered to contribute to drag. In reverse translocation, the DNA is under tension, and the portion remaining inside the pore

adds to the resistance. This compression versus tension effect of forces is the difference between forward and reverse translocation, and impacted the observed translocation characteristics. Forward events had shorter event duration with increased current blockades. Reverse events had longer event duration, and were also found to have more complex event profiles due to increased folding and steric effects.[13,17,18]

### 4.1.2 TRANSLOCATION CHARACTERISTICS

To illustrate how DNA translocation events appear and their potential diversity, a representative current-time trace from a DNA translocation experiment is shown in Figure 4.1. This 10-second recording was obtained at an applied voltage of -0.6 V, with a sampling rate of 10 MHz. The open-pore current appears as the baseline, which fluctuates above and below 0 A. The transient downwards spikes in the signal indicate discrete DNA translocation events. A detection threshold of 5σ (five times the standard deviation of the baseline noise) is applied to identify significant deviations from the background. This relatively high threshold is used to minimise the number of false positives arising from electrical noise and to reduce the burden of downstream data analysis. DNA translocation events typically produce a large and distinct current blockade, therefore setting a higher cutoff helps to focus data analysis on meaningful events with a high likelihood of being true DNA events.

Four representative examples of detected events (labelled I – IV) have been highlighted to demonstrate the variety of observed signal types. Events I – III display true DNA translocation events and show characteristic differences in their traces. Event I displays a deep and 'square-shaped' blockade, consistent with a folded DNA translocation. Event II shows a shallower but broader event trace, consistent with single-file, linear translocation of the DNA strand. Event III appears more complex, with two blockade steps during translocation. The initial, deeper blockade is due to partial folding of the DNA as it enters the pore. Once the folded region has passed through the pore, the remaining segment of DNA translocates in a linear fashion, shown in the trace by a lower degree of current blockade. By contrast, event IV exhibits a very brief, high-amplitude spike with no square-base or clear substructure. This is characteristic of noise, rather than a DNA event. These examples help distinguish between true events and noise artefacts, and illustrate the importance of considering signal shape, amplitude and duration in data interpretation.

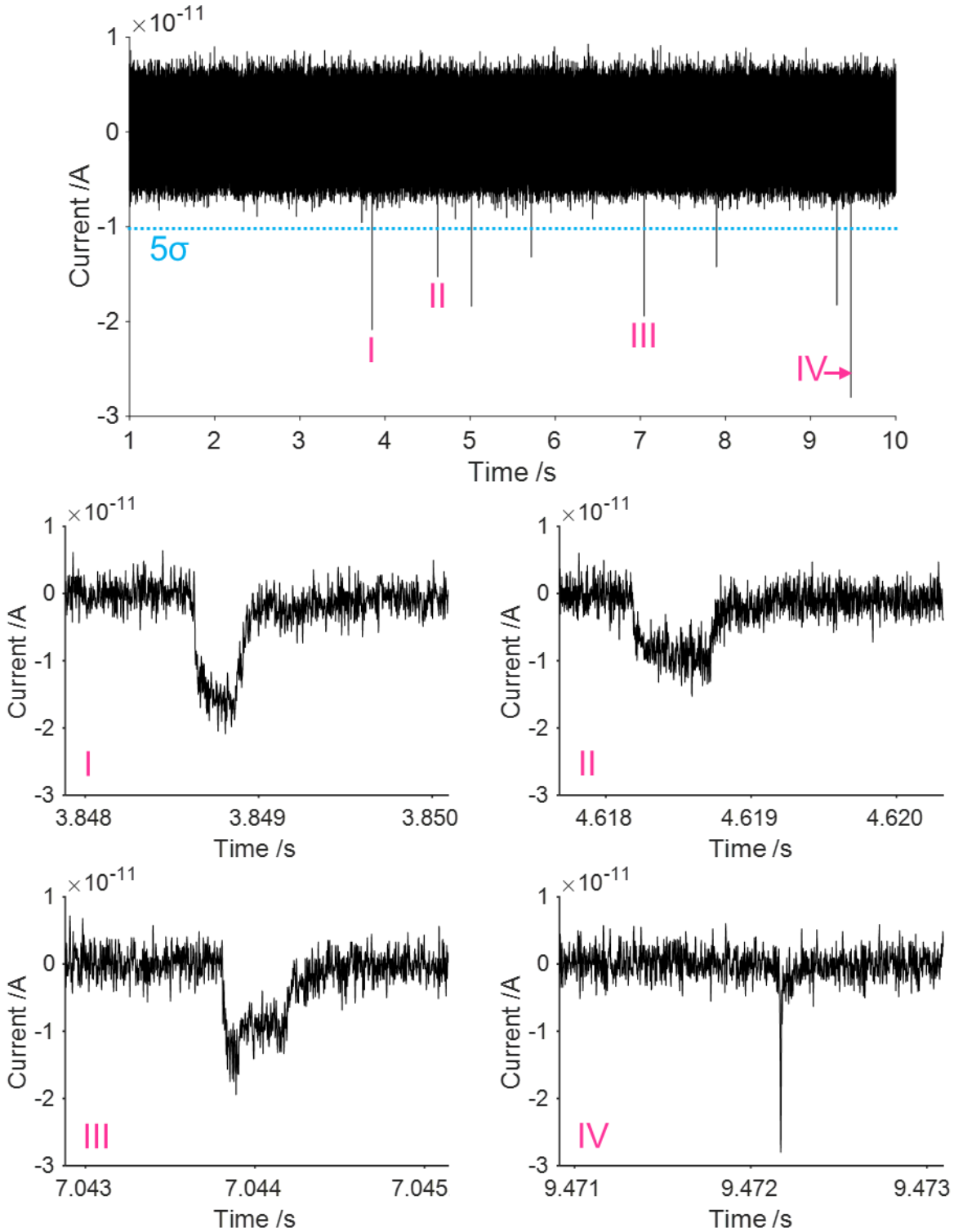


*Figure 4.2: Top, current-time trace recorded at -0.6 V, showing DNA translocation events as sharp deviations from the open-pore current baseline. A 5σ threshold (dashed blue line) is used for data filtering and event detection. Four representative events are highlighted displayed in the smaller traces: I) folded DNA molecule, II) linear DNA molecule, III) partially folded DNA molecule, and IV) noise spike.*

As such qualitative analysis isn't practical to study potentially thousands of translocation events, two primary characteristics are used to quantitatively describe and compare DNA translocation events: current blockade ($\Delta I$) and dwell time ($\tau$). Current blockade refers to the change (either increase or decrease) in ionic current caused by the presence of the DNA molecule in the nanopore, while dwell time is the duration for which the DNA remains within the pore during translocation (Figure 4.3).

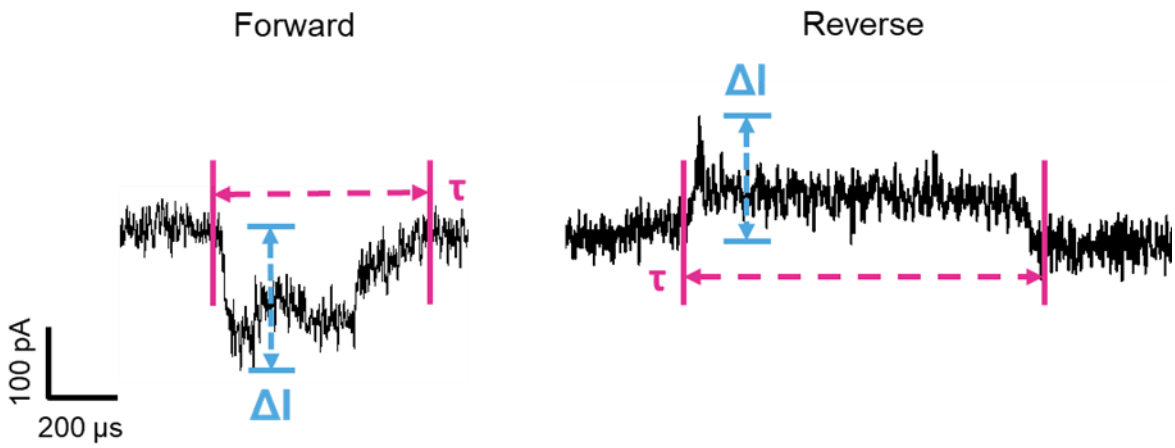


*Figure 4.3: Examples of translocation events in current-time traces, labelled with the peak current change in blue ($\Delta I$) and event duration in magenta ($\tau$). In the forward translocation direction, a current decrease is observed, in the reverse direction a current increase is observed.*

These parameters are influenced by several factors, including the size and conformation of the DNA, the geometry of the nanopore, and the applied voltage. These average translocation properties can be useful for determining the contour length of analytes, for example.[19] However, the distribution of these properties can also be revealing.

At high applied bias, the electric field near the nanopore entrance is strong enough to drive DNA translocation in the drift-dominated regime, where electrophoretic forces outweigh passive diffusion. In this regime, the distribution of DNA translocation durations can be described by Equation 4.1, a model proposed by Ling & Ling and based on Schrödinger's first-passage time theory.[20] The probability density function, *P(t)*, represents the likelihood of a molecule completing translocation through the nanopore at a given time *t*.

$$P(t) = \frac{L}{\sqrt{4Dt^3}} \cdot e^{-\frac{(L-vt)^2}{4Dt}} \tag{4.1}$$

In this equation, $L$ is the contour length of the DNA molecule, $D$ is the diffusion coefficient of the DNA inside the nanopore, $v$ is the drift velocity due to the applied electric field and $t$ is the translocation time. This model predicts a positively skewed time distribution under typical conditions, where the most probable translocation times are shorter than the mean. This is due to the forces on the DNA, both the consistent, directional drift from the pull of the electric field and the random, fluctuating effects of diffusion, which results in the model's predicted asymmetry. Most events are faster, because drift dominates, but a tail of slower events exists due to the stochastic nature (hence, occasionally stronger influence) of diffusion.[20] The width of the time distribution therefore depends on $D$, $L$ and $v$.

Importantly, this distribution places a theoretical limit on the ability of nanopores to detect the structural features of a modified DNA strand, whatever they may be. If the time between the successive features is smaller than the standard deviation of the translocation time, the features cannot be temporally resolved. This sets a lower limit on the spacing between features in a designed DNA carrier structure.[20] This will be further compounded by the experimental reality of bandwidth limitations,[2] additional distribution broadening[3] and practical restrictions on structure design.[6-9]

### 4.1.3 Complex DNA Structures and Reference Datasets

The complexity of DNA translocation and data analysis increases when moving from linear translocation configurations, to folded configurations, and finally to a combination of the two with more complex structures, such as DNA carriers. Translocation of these structures can often yield difficult-to-interpret current blockade signals and subevents,[21-23] owing to different translocation conformations and the potential for nanopore interactions.[24] Without a clear understanding and full characterisation of the translocation behaviour of simpler, linear DNA molecules, it becomes more difficult to accurately interpret data from more complex analytes.

In these cases, having a reliable reference dataset of simpler translocation events, such as those presented in this chapter, is necessary to allow for accurate interpretation of more complex events. By understanding the characteristic features of linear DNA translocation, including the expected current blockade and dwell time distributions, researchers can better identify anomalies or unique features in the translocation profiles of complex molecules. This study

aims to provide a reference dataset for linear 4 kbp dsDNA translocation in both forward and reverse directions, under controlled experimental conditions.

## 4.2 AIMS AND OBJECTIVES

The aim of this work is to establish a reference dataset for DNA translocation, by fully characterising the translocation of linear 4 kbp double-stranded DNA (dsDNA) molecules through a quartz nanopipette, using the optimised experimental set-up (established in Chapter 2) and a 100 kHz low-pass filter. The chosen analyte length is approximately the same as modified DNA structures produced in related work,[23] providing a valuable reference for subsequent experiments on more complex analytes. The objectives of this work are as follows:

1. Evaluate linear/folded event clusters and separation in both the forward-direction at negative bias and the reverse-direction at positive bias.
2. Determine average translocation characteristics of linear events for both directions and compare with literature.
3. Gauge potential impact of baseline noise on subevent detection in linear events.
4. Assess the signal-to-noise ratio (SNR) of the optimised experimental set-up with a 4 kbp dsDNA translocation experiment.
5. Conclude suitability of experimental set-up and current analysis methods for translocation of more complex structures.

## 4.3 MATERIALS AND METHODS

Unless otherwise stated, chemical reagents were purchased from Sigma-Aldrich (Merck Group).

### 4.3.1 PIPETTE FABRICATION

Quartz capillaries (outer diameter: 1 mm, inner diameter: 0.5 mm, length: 7.5 cm, catalogue number QF100-50-7.5, Sutter Instruments, USA) were plasma cleaned for 20 minutes. A P2000 pipette puller (Sutter Instruments, USA) and the following two-line program was used: heat 750/850, filament 5/0, velocity 35/15, delay 150/128, and pull 75/200. These parameters typically produced pipettes with a pore diameter in the range of 20 – 30 nm, and a taper length of approximately 3 mm.

Images of pipettes were taken using a Nikon Type 105 optical microscope (Nikon Corporation, Japan), with 4x magnification used to measure the length of the taper, from shoulder to tip.

### 4.3.2 LIQUID CELL ASSEMBLY

Amber glass vials with screw-top lids were used to hold both the nanopipette and outer electrolyte reservoir. The glass vials were plasma cleaned for 20 minutes before use. To create the openings for the electrode and pipette, two 1 mm holes were drilled into the vial lid, as illustrated in Figure 4.4.

The electrolyte used was composed of 4 M anhydrous lithium chloride, MilliQ water and 10 % Tris-EDTA (TE) buffer (Fisher Scientific, USA). This solution was then filtered through a 0.2 µm filter to remove any particulates. Two mL of the electrolyte solution was pipetted into the vial. The nanopipette was filled with electrolyte using a Microfill 34-gauge 64 mm needle before being inserted into the vial.

Silver/silver chloride electrodes were used to measure the ion current through the pore. First, pure silver wire (0.25 mm diameter, 99.998 % purity) was cut to the desired length and partially immersed in 35.5 % nitric acid for 20 seconds. The wire was removed and rinsed thoroughly with MilliQ water. The cleaned portion of the wire was then anodised electrochemically, using a gold counter electrode. A constant current of 1 mA was applied for 20 minutes. The electrolyte solution of 4 M LiCl and 10 % TE buffer was used for anodisation. The electrodes were then soldered to a gold pin and stored in the dark when not in use. After initial anodisation, electrodes were re-anodised before use to prevent depletion of AgCl. One electrode was inserted into the nanopipette and the other directly into the cell.

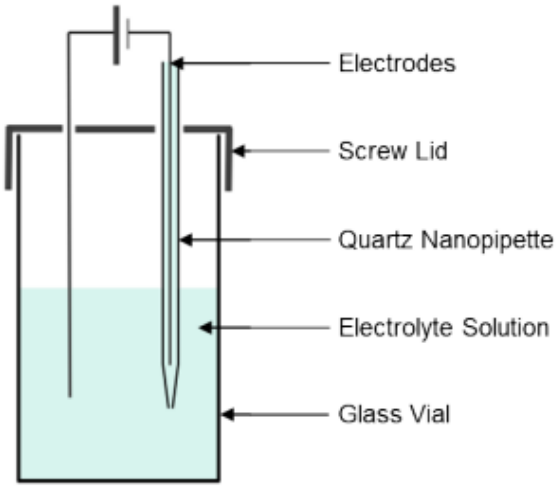


*Figure 4.4: Experimental set-up of the liquid cell.*

### 4.3.3 Conductance Measurements

The prepared liquid sample cell was transferred to a Faraday cage and the electrodes connected to a two electrode CompactStat potentiostat (Ivium Technologies, Netherlands). The electrode within the pipette was connected as the working electrode; the pipette within the electrolyte/cell functioning as the counter electrode. The associated Ivium software had the following settings: scan range of -0.5 to +0.5 V, 4 mV scan rate for 5 scans in total. From the current-voltage scan, the conductance was determined and used to generate an estimate for the pore size, illustrated in Equation 4.2. The equation relates conductance and pore size, where *G* is conductance of the nanopipette, *l* the taper length, $D_i$ the inner diameter of the quartz capillary, and *g(c)* the conductivity of the electrolyte solution.

$$d_{pore} = \frac{4Gl + \frac{\pi}{2}GD_i}{D_i\pi g(c) - \frac{\pi}{2}G} \tag{4.2}$$

### 4.3.4 DNA Translocation Experiments

Figure 4.5 shows the nanopore sensing set-up. Further details of the electronic instrumentation can be found in Chapter 2, section 2.3.1.

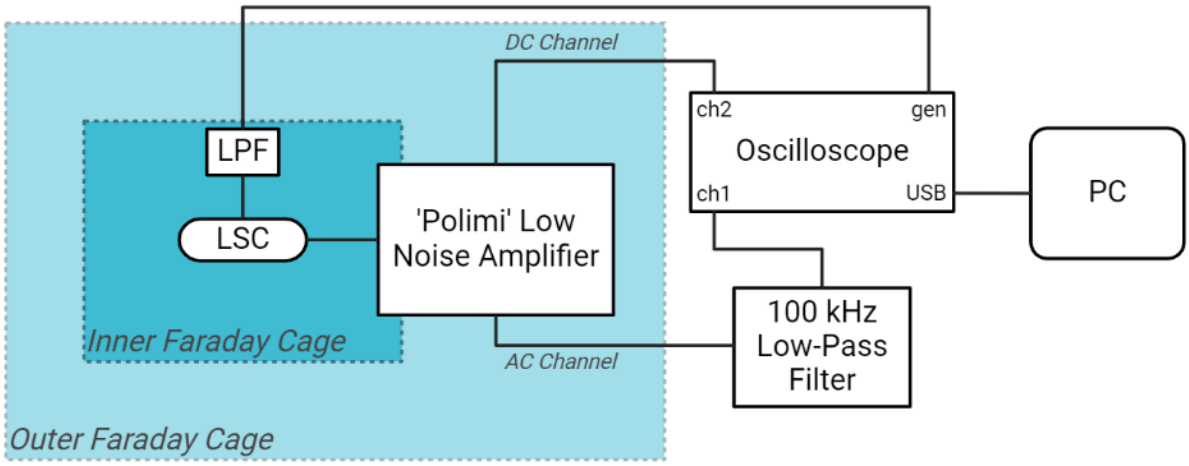


*Figure 4.5: Schematic representation of the nanopore sensing set-up, containing the liquid sample cell (LSC), 'Polimi' amplifier and peripheral electronics. A voltage is applied to the cell using a PicoScope oscilloscope. The current signal is amplified and split into two channels by the 'Polimi' amplifier. The AC channel is filtered through a passive 100 kHz low-pass filter before digitisation, alongside the DC channel, by the oscilloscope. The small and large Faraday cage are represented by the dashed lines.*

For DNA translocation, 4 kbp dsDNA (NoLimits 4000 bp DNA Fragment, Thermo Scientific, USA) was pipetted into the liquid cell and homogenised, to give a working concentration in the vial of 300 pM. One hundred data files were recorded at each bias voltage, between -0.8 to -0.4 V, and +0.4 to +0.8 V.

Custom-written MATLAB code (authored by Prof. Tim Albrecht, University of Birmingham) was used for instrument control, data acquisition, event detection thresholding analysis and subevent detection. Events were detected using an $5\sigma$ cut-off value, where $\sigma$ is the standard deviation of the current noise in the AC channel. The search algorithm then selected data points with a $1\sigma$ cut-off. This defined the start and the end of the translocation event. Using a $1\sigma$ cut-off allows for the majority of the event shape to be captured, whilst minimising the effect of local baseline fluctuations on the event characteristics. The duration of the event is therefore defined as $\tau_e = t_{end} - t_{start}$. The current decrease of the event, $\Delta I_e$, was calculated from the integral of the $I(t)$ trace, between $t_{start}$ and $t_{end}$ (which gives the event charge deficit of the event $q_e$) and divided by $\tau_e$.

To separate the linear translocation events from the folded, custom-written MATLAB code with *k*-means clustering was used. SNR was calculated with the equation $SNR = \Delta I_e / I_{RMS}$, where $I_{RMS}$ is the root-mean-squared noise as calculated by the MATLAB code.

## 4.4 RESULTS AND DISCUSSION

For these 'baseline' translocation experiments, dsDNA of 4 kbp length was chosen as the analyte. The modified DNA structures produced within the Albrecht group are also approximately 4 kbp in length.[25] Hence, an experiment performed with unmodified DNA of similar length could be fully analysed and used as a reference point for future experiments with a more complicated analyte that would allow the data analysis to be simplified. Furthermore, it is of interest to fully characterise translocation in the both the forward and reverse direction. Analysis of forward translocation data, conducted by Rand Al-Waqfi in the Albrecht Group, revealed distinct event profiles, prompting further investigation into the characteristics of DNA translocation in both forward and reverse directions. This initial finding served as the foundation for the dataset analysis presented in this work.

### 4.4.1 Characterisation of Linear and Folded Event Clusters

The current-time data was analysed using a thresholding algorithm to identify events, signal-blocking at negative bias (forward translocation) and signal-enhancing at positive bias (reverse translocation).

**Forward Translocation at Negative Bias**

The results from the thresholding algorithm for forward translocation events are shown in Figure 4.6. The graph on the left is a scatter plot of all signal-blocking events that passed the 5σ detection threshold. Each point corresponds to a single detected event, plotted by it's maximum current blockade (in amperes) and event duration (in seconds), as determined by the analysis algorithm. This representation allows for easy interpretation of the key translocation characteristics (as discussed in section 4.1.2). However, the inclusion of all detected events above the 5σ threshold means that short-lived noise spikes are also present, alongside DNA translocation events.

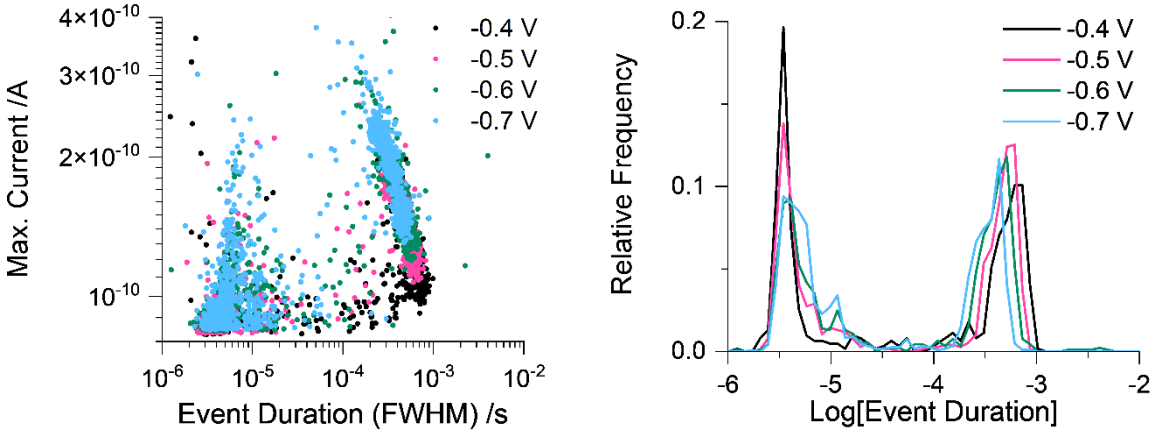


*Figure 4.6: Results of the thresholding algorithm for signal-blocking events in the forward translocation direction. Left; maximum current decrease and full-width half-maximum (FWHM) time duration of each signal detected as an event. Right; histogram of the time duration of detected events.*

The graph on the right of Figure 4.6 shows a histogram of event durations, plotted as relative frequency vs. $\log_{10}$(event duration). The x-axis values are therefore log-scaled representations of time (as such, -3 corresponds to $10^{-3}$ seconds, or 1 ms), and both axes are dimensionless. This representation of data allows for a clearer assessment of translocation time and bias

dependency. This distribution shift with voltage is a hallmark of electrophoretically driven translocation, and absent in noise-dominant populations.[19]

Two clear clusters in the data are visible. The first cluster, at short durations (1 – 10 µs), is attributed to high frequency noise spikes. These are stochastic fluctuations and have no dependence on applied voltage. This is supported by the observation that, for all biases, the peak of this noise cluster remains fixed at approximately 3 µs.

The second data cluster (0.1 – 1 ms), does show clear voltage dependency. As bias increases, the events become shorter, consistent with electrophoretic transport.[33-35] As such, these events are assigned to DNA translocation. This time-bias dependency is explored in greater detail later in this chapter.

Although the current blockade values of noise and DNA clusters overlap, the histogram shows good temporal separation to aid in further data filtering and prevent noise data from skewing quantitative analysis of translocation characteristics.

**Reverse Translocation at Positive Bias**

Figure 4.7 shows the same style of analysis as shown previously in Figure 4.6, but instead applied to the reverse translocation direction at positive bias. Here, the thresholding algorithm detects signal-enhancing events (transient increases in current), corresponding to DNA exiting the nanopipette.

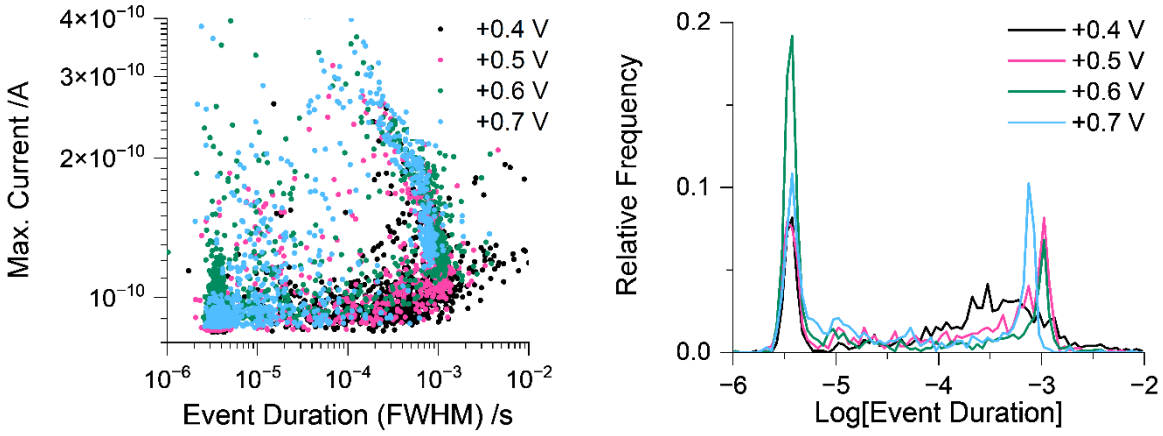


*Figure 4.7: Results of the thresholding algorithm for signal-enhancing events in the reverse translocation direction. Left; maximum current increase and FWHM time duration of each signal detected as an event. Right; histogram of the time duration of detected events.*

Similar to forward translocation, two data clusters can be seen: shorter time duration noise spikes (peaking at 3 μs), and longer duration translocation events (approximately 1 – 0.1 ms). Again, the longer duration cluster exhibits bias dependency of electrophoretic transport, supporting the conclusion that this cluster is due to DNA translocation.

However, compared to the forward direction, the temporal separation between noise and translocation events is much poorer at +0.4 V and +0.5 V. This reduced separation complicates analysis and suggests an underlying difference in translocation dynamics.

The underlying mechanisms for reverse translocation are only speculated, but one explanation is that DNA molecules face a higher energy barrier when attempting to translocate out of the nanopore in the reverse direction owing to the asymmetric, conical geometry of the nanopipette.[16] This narrowing of the pore increasingly confines the DNA and increasing resistance as it moves towards the tip. Although electrophoretic forces would typically dominate with applied biases, the associated entropic barrier may become increasingly significant, particularly at lower voltages. This could lead to transient blockades or increased interactions with the nanopipette walls, resulting in shorter duration, lower amplitude events and, consequently, poorer temporal separation. At lower experimental biases, some DNA molecules may lack sufficient energy to fully overcome the entropic barrier, leading to fewer successful translocation events.

In addition to this, at higher biases, the dwell time distribution appears compressed, peaking at longer translocation times, with a narrower spread than that observed for forward translocation. This may be attributed to the increased entropic barrier, hydrodynamic drag, and geometric constraints during reverse translocation, which collectively result in more uniformly prolonged translocation times. These effects likely reduce the relative influence of stochastic diffusion on the overall time distribution, compared to the forward direction.

### 4.4.2 Average DNA Translocation Characteristics

Further clustering and noise removal was performed to focus on the key characteristics of DNA translocation events.

**Forward Translocation at Negative Bias**

The distribution of DNA translocation events in the forward direction is shown in Figure 4.8. The histogram of event durations (right) displays a negative skew, meaning that while most

events have longer durations, a smaller number show shorter translocations, presenting as a tail in the data. This is seen in the sharp increase in relative frequency from -3 of the log($\tau$), and a more gradual decline in the relative frequency moving towards -4 of log($\tau$) (in real terms, from 1 ms to 0.1 ms). This contradicts models such as that by Ling & Ling, which predict a positively skewed distribution. This means most events should be faster, with a tail in the data towards longer translocation times.[20]

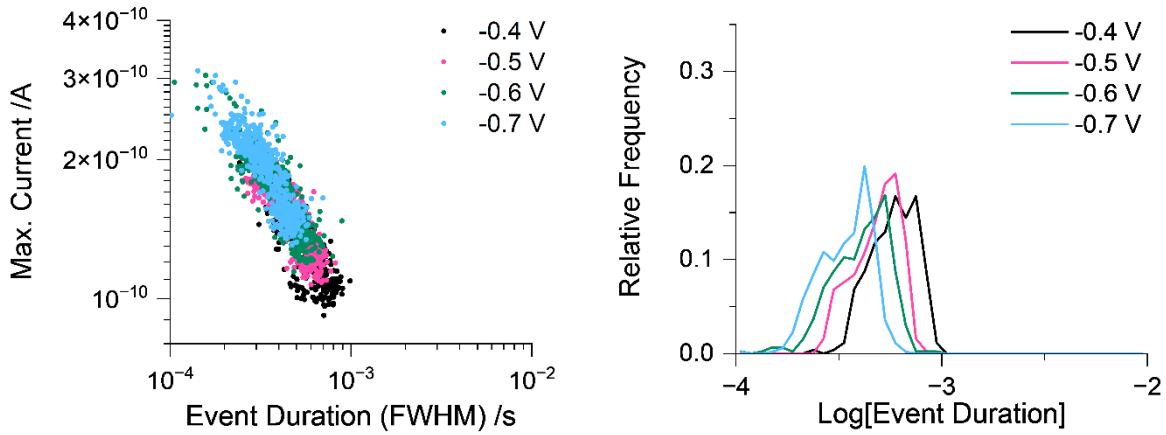


*Figure 4.8: DNA translocation event clusters in the forwards direction at negative bias. Left; maximum current decrease and FWHM event duration of DNA translocation events. Right; histogram of FWHM event duration.*

In this case, the observed negative skew may arise from multiple overlapping event populations. This corresponds to the different DNA conformations during translocation, such as linear, folded or knotted structures, which have been well studied in the literature. [13,18,34,36] These conformations effect both the translocation speed and the observed current blockade. For example, folded DNA produces larger current blockades but shorter dwell times. This would change the expected distribution shape and mask the underlying drift-diffusion behaviour predicted by theory. The current dataset supports this, as shown in Figure 4.9, where examples of knotted, folded, and linear DNA traces are presented.

These various translocation conformations produce distinct signatures in both current blockade and event duration. Trace number 1 most likely arises from DNA knotting, traces 2 – 15 demonstrate different degrees of DNA folding over on itself and the corresponding doubling in the current decrease as the folded sections of DNA translocate, and traces 16 – 25 show linear DNA translocation.

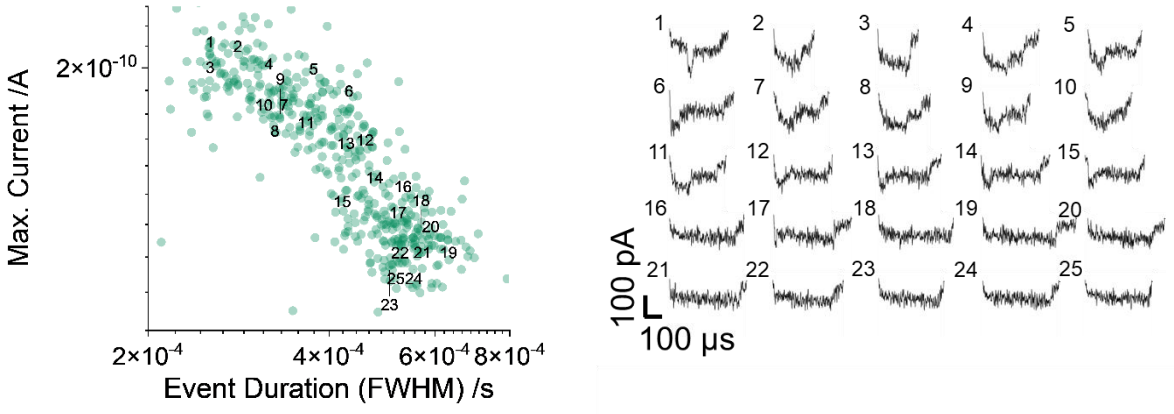


*Figure 4.9: Left; current v. event duration for DNA translocation events at -0.6 V bias, overlaid numbers correspond to the event traces shown on the right and their location in the event clusters. Events are numbered 1-25, from largest current decrease to smallest.*

**Reverse Translocation at Positive Bias**

The DNA translocation event cluster for reverse translocation is shown in Figure 4.10. Again, the time distributions largely skew negative due to overlapping clusters of different DNA conformations, as discussed above.

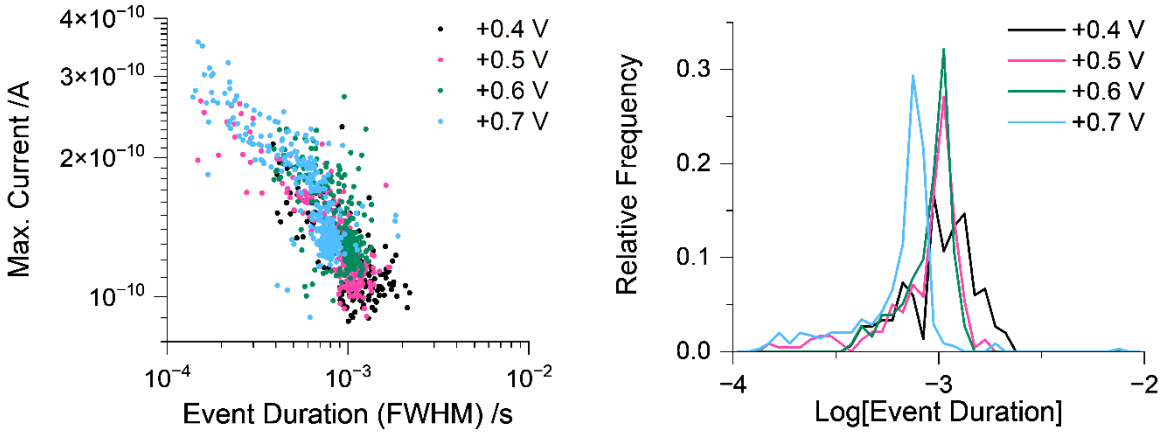


*Figure 4.10: DNA translocation event clusters in the reverse direction at positive bias. Left; maximum current increase and FWHM event duration of DNA translocation events. Right; histogram of FWHM event duration.*

**Relative Frequency of Linear and Folded Events**

A 40/60 ratio in the frequency of linear and folded translocation is seen for all negative biases, shown in Figure 4.11.

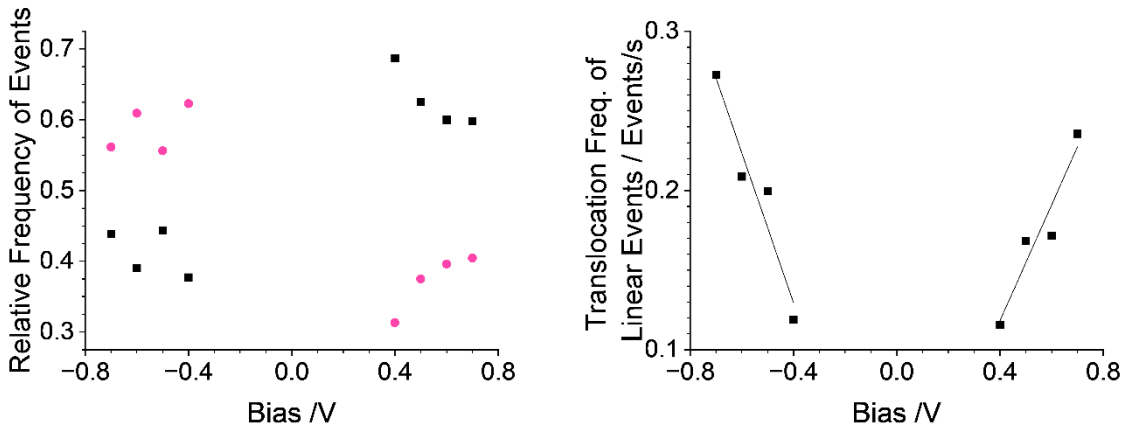


*Figure 4.11: Left; relative frequency of linear (black) and folded (magenta) translocation events at each bias voltage. Right; the translocation frequency of linear events at each bias voltage, with linear data fit.*

This finding is at odds with reports in the literature by Chen *et al*. They observed that the proportion of linear events increases with bias voltage. They suggest this is because of an inhomogeneous electric field on the globular DNA strand in solution as it approaches the pore. At higher bias the electric field is stronger, and the DNA is more likely to stretch and translocate linearly.[37] However, the results in Figure 11 suggest a deviation from this trend, likely due to the high salt concentration (4 M LiCl) used in this experiment. The lithium ions act to further shield the DNA strand from the effects of the electric field.[38,39]

Ermann *et al.* have studied the effect of salt concentration, alongside the effects of DNA concentration, pH, and electrolyte composition, on the relative proportion of linear events.[18] Their work demonstrated that, in 4 M LiCl electrolyte, only 40% of the observed translocation events were linear, closely aligning with the results here. They suggest the reason for increased linear translocation at low salt concentrations is due to the onset of electro-osmotic flow from the pore, as the negative charge of the glass nanopipette surface is not as well screened by electrolyte counterions.[16]

In the reverse direction, DNA translocation is influenced by a distinct set of factors. Zheng & Han reported that DNA tends to adopt more compact, folded conformations during reverse

translocation due to higher energy barriers, though they did not quantify the relative occurrence of linear and folded events.[16] However, it was noted that the more constricted the nanopipette, the higher the probability of DNA folding during reverse translocation. Similarly, Bell *et al*. observed a greater incidence of complex folded DNA conformations, but also provide arguments for DNA translocation in the reverse direction as occurring under tension, where the molecule translocates as a rigid rod.[13] In contrast to this study, both experiments used nanopipettes with reported pore diameters of 14 ± 3 nm. The larger pore size of ~25 nm used in this study may explain the higher frequency of linear events observed. As the DNA becomes increasingly restricted towards the nanopore exit, the larger pore size may prevent the DNA from becoming trapped in the reported complex transient conformations.[13,16]

For translocation in both directions, the number of events, and hence linear events, does increase with bias. This is as expected; the voltage bias is proportional to the flux, the frequency with which DNA enters the capture radius of the nanopore,[40] shown in Equation 4.3.

$$J = \frac{\pi d^2 \mu}{4 L_P} \cdot V_{bias} \cdot c \qquad (4.3)$$

$J$ is flux, $d$ is the pore diameter, $\mu$ the free-solution electrophoretic mobility of DNA, $L_P$ the length of the pore channel, $V_{bias}$ the applied voltage bias and $c$ the DNA concentration in solution. Fewer translocation events are recorded in the reverse direction. This may be due to the reduced volume within the nanopipette which significantly restricts the diffusion of DNA, reducing the number of molecules which can diffuse from the wider region of the nanopore to be captured by the electric field.

**Translocation Characteristics of Linear Events**

The data cluster of folded events was excluded from further analysis. Histograms of peak current and event duration for linear events in both forward and reverse translocation are shown in Figures 4.12 and 4.13, respectively.

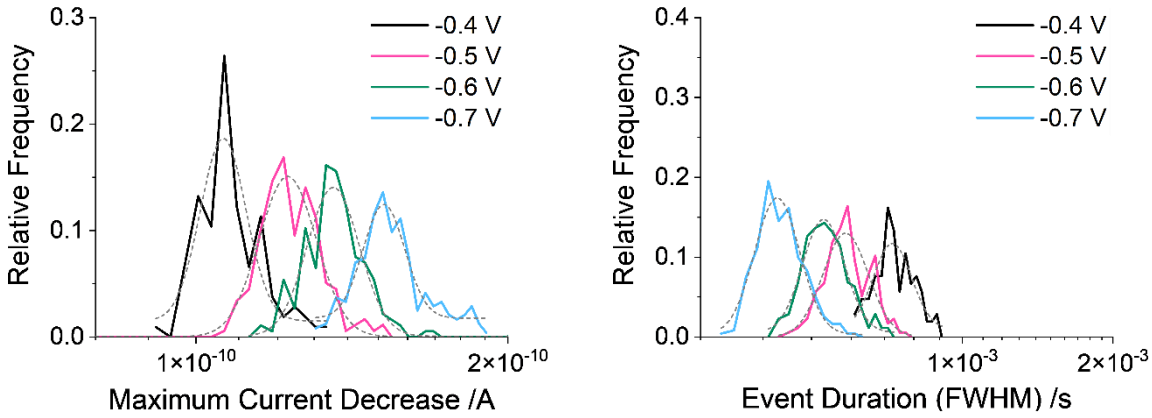


*Figure 4.12: Linear DNA translocation events in the forward direction. Left; normalised histogram for the maximum current decrease of linear events at each negative bias voltage. Right; normalised histogram for the event duration of linear events at each negative bias. The dashed grey lines are log-normal curve fits for each bias dataset.*

DNA translocation is a stochastic process, and a relatively wide distribution in event duration and current decrease is well reported. In fact, experimental distributions are often wider than theoretically predicted. Thermal fluctuations, local variations in electroosmotic flow, and the diverse structural conformations of DNA as it approaches the pore all contribute to the spread in measured values.[20,41,42]

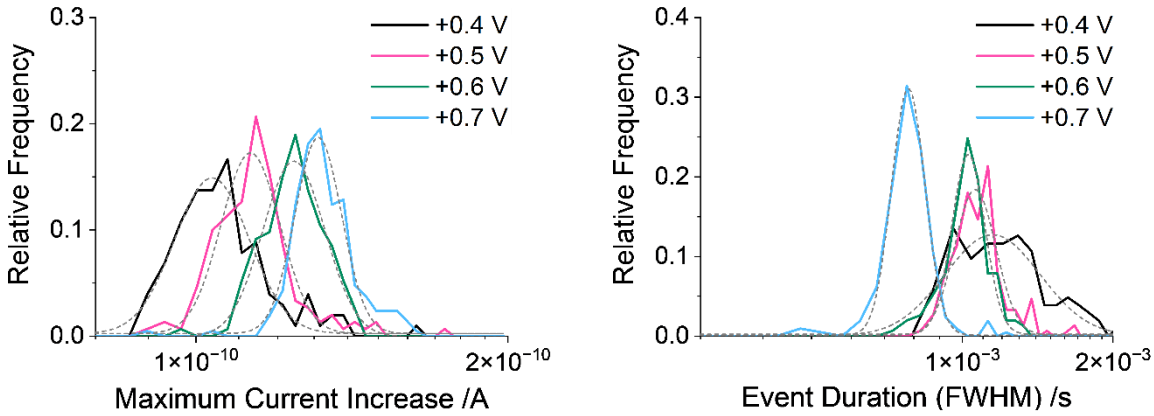


*Figure 4.13: Linear DNA translocation events in the reverse direction. Left; normalised histogram for the maximum current increase of linear events at each positive bias voltage. Right; normalised histogram for the event duration of linear events at each positive bias. The dashed grey lines are log-normal curve fits for each bias dataset.*

In both forward and reverse translocation, the distributions of peak current and event duration exhibit a positive skew, in agreement with predictions from the Ling & Ling model.[20] Despite efforts to fit the data to Equation 4.1, difficulties in parameter optimization prevented a direct fit. As an alternative, a log-normal fit was applied to the data to determine the mode values for both current decrease and event duration, as summarized in Figure 4.14.

**Bias Dependence of Translocation Parameters**

The relationship between translocation parameters and applied bias follows expected trends. The peak current of translocation events exhibits a linear dependence on applied bias, consistent with reports in the literature. The geometry of the nanopore (the pore diameter, channel length and inner cone angle) influences the peak current. The dimensions of the nanopipette used in this experiment were calculated from conductance measurements, an indirect technique. Direct characterisation with imaging techniques, such as SEM or TEM, would give more information and allow for a more accurate measurement of pore dimensions.

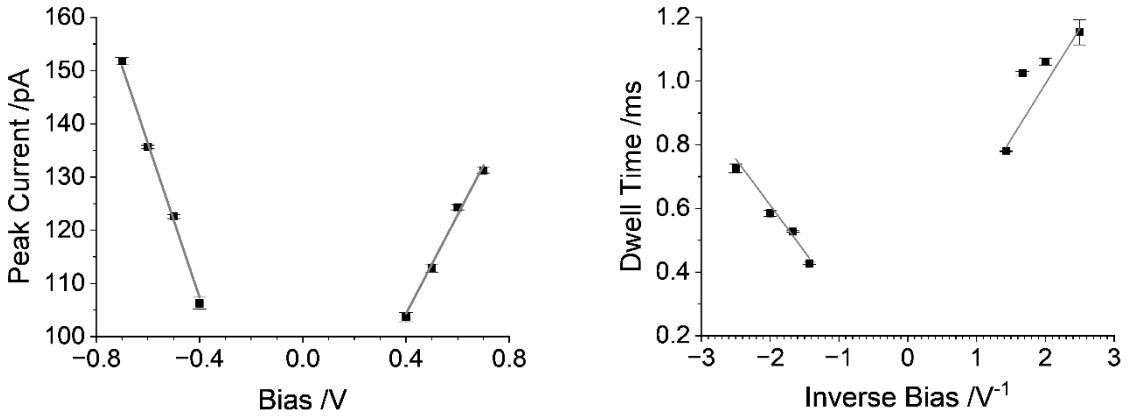


*Figure 4.14: Left; average peak current of linear translocation events at each bias voltage. Right; average dwell time for linear translocation events as a function of 1/bias voltage. Linear fits are represented in grey.*

For each positive bias, the peak current is smaller compared to the corresponding negative bias, in line with literature findings. It has been suggested that that DNA undergoing reverse translocation experiences greater hydrodynamic drag, compacting the DNA strand and reducing the number of blocked ions, thereby giving a smaller peak current signal. Conversely, during forward translocation, the DNA's rapid movement and strong negative charge may accelerate ions in its electric double layer, enhancing the current blockade.[16]

The dwell time of DNA translocation was found to be inversely proportional to the applied bias, as demonstrated in Figure 4.14.[33,43] At high bias with long DNA, as used in this experiment, the dwell time can be estimated at the Smoluchowski limit according to Equation 4.4, where $v = \mu E$ and $E = V_{bias}/L_P$. $\tau$ is dwell time of long DNA, $L$ is DNA contour length, $\mu$ the electrophoretic mobility of DNA in the pore, $E$ the local electric field, $L_P$ the channel length of the pore and $V_{bias}$ the applied bias.

$$\tau \approx \frac{L}{\mu E} \approx \frac{L L_P}{\mu V_{bias}} \tag{4.4}$$

This inverse relationship between dwell time and bias voltage is well reported experimentally and is a hallmark of electrophoretically driven transport.[4,19,20,33,42] The dependence of dwell time on the DNA contour length is less straight forward and often not linear.[42] The geometry of the nanopore also has an impact on the dwell time, further underscoring the need for precise characterization of the nanopipettes used in these experiments.

**Comparison of Forward and Reverse Translocation**

Reverse translocation events at positive bias were found to have a longer dwell time than the equivalent forward translocation events. A DNA buckling theory has been suggested to explain the discrepancy.[13] In forward translocation, there is an asymmetric electric field distribution. At first, there is a strong electric field driving the DNA through the pore. As such, DNA experiences less electric force as it moves further through the nanopore, and the molecule starts to buckle once it has entered the pore. This results in a shorter effective molecule length and reduced drag force, thereby reducing translocation time. This is similar to the concept of DNA recoiling during passive translocation.[11] The difference between this and the buckling theory is the underlying translocation regimes and force profiles. In the buckling theory, additional external forces act on the DNA, even when it is no longer translocating through the pore, such as electrophoretic forces and hydrodynamic drag.[12, 13]

In the reverse direction, the DNA molecule has a longer effective length and experiences greater hydrodynamic drag and increased resistance. As the electric field strength increases moving towards the tip of the nanopipette, the molecule is stretched, leading to longer translocation times. Zheng & Han report a threefold increase in dwell time for reverse translocation.[16] In this experiment, the increase in dwell time is just less than two-fold. This can again be explained by nanopore geometry. As the underlying mechanism for reverse translocation is greatly

influenced by the nanopore diameter and nanopipette channel length, differences in nanopore geometry will affect the translocation characteristics. The experiment in this study used a larger nanopore, which would reduce the resistance experienced by the DNA, resulting in a smaller difference in dwell time between forward and reverse translocation.

### 4.4.3 Impact of Baseline Noise on Subevent Detection

Finally, data for the linear events in the forward direction was further analysed with a subevent detection algorithm, to determine any impact of background noise on the event traces themselves. The relative frequency of the detected 'subevents' by their normalised position on the DNA strand is shown in Figure 4.15.

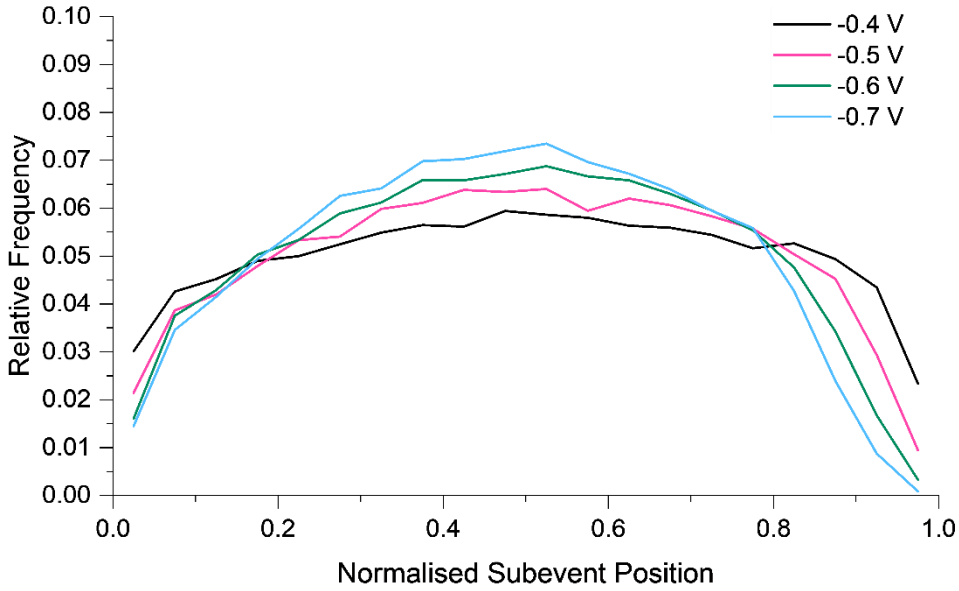


*Figure 4.15: Histogram showing the relative frequency of detected subevents at normalised positions along the DNA length, for each negative bias.*

For a linear DNA strand with no structural features, any subevents detected would reasonably be attributed to noise in the signal. As noise is generated randomly, the histogram would be expected to show minimal deviations between detected subevent positions. This is seen to be the case, and consistent between different biases. Overall, between different subevent positions and different biases, there is a very low relative frequency of detected subevents. This would not be expected to impact significantly on subevent detection in future experiments, when structural features on the DNA would be present.

### 4.4.4 SIGNAL-TO-NOISE RATIO

Calculated signal-to-noise ratios (SNR) for this translocation experiment range from 1.2 – 1.9 (Figure 4.16). Compared to the relevant literature, these values are quite low, as SNRs of up to 20 have been reported in highly optimised nanopore set-ups.[26-32] These results show a general trend of improving SNR with increasing voltage bias, for both forward and reverse translocations.

This trend is expected; the background noise resulting from the experimental set-up is largely the same for different bias voltages. However, at increasing positive or negative bias, the size of the DNA-induced current modulation also increases, resulting in better SNR. In these experiments, the major noise sources are input capacitance and amplifier noise, with additional contributions from parasitic capacitance in the liquid sample cell. Further optimisation of the liquid sample cell may be required to further reduce noise levels, particularly if higher filter frequencies need to be used.

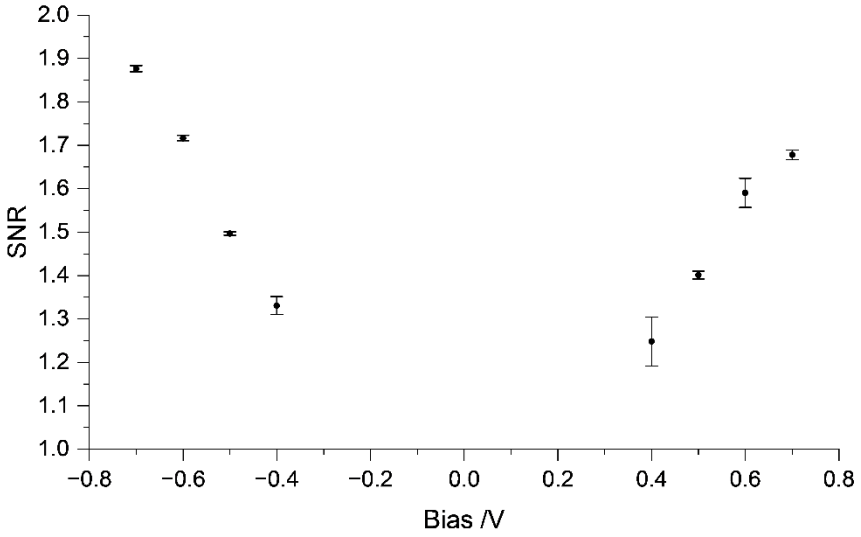


*Figure 4.16: Signal-to-noise ratio (SNR) for each applied bias in the DNA translocation experiment. The SNR was calculated by dividing the average peak current of linear events by the average RMS noise for each bias. The graph shows an increasing SNR with increasing bias (both positive and negative directions).*

### 4.4.5 SUITABILITY OF EXPERIMENTAL SETUP FOR COMPLEX STRUCTURES

The results from this baseline study of 4 kbp dsDNA translocation suggest that, despite a relatively low SNR, the optimized setup provides adequate resolution for detecting and

analysing linear DNA events. Furthermore, subevent detection was minimally impacted by baseline noise, providing confidence in the system's suitability for experiments involving more complex DNA structures, such as DNA-antibody conjugates. In addition, populations of DNA translocation conformations were able to be distinguished and separated for data analysis. At 10 kHz, this event clustering was not resolved owing to lower resolution. These experiments at 100 kHz represent a step forward for the group in terms of data quality and analysis potential.

## 4.5 CONCLUSIONS & FUTURE WORK

The aim of this work was to establish a comprehensive reference dataset with the translocation of 4 kbp linear dsDNA, to determine the suitability of the optimised set-up and 100 kHz low-pass filter, and to evaluate the suitability of the data analysis methods for complex analytes.

**Conclusions**

1. **Signal-to-Noise Ratio (SNR):** SNR ranged from 1.2 to 1.9, lower than values reported in the literature for highly optimised systems. However, the data analysis shows that the translocation events can be temporally separated from noise clusters, allowing for accurate event identification, even with the low SNR.
2. **Characterisation of Forward and Reverse Translocation Events:** Noise signals and translocation events, for both forward and reverse translocation, presented as distinct data clusters. Additionally, linear and folded translocation events in both directions were able to be clustered further. A consistent 40/60 split between linear and folded events was observed for forward translocation across all negative biases, likely due to the high lithium-ion concentration used. During reverse translocation, 60–70% of events were found to be linear. This could be attributed to differing force profiles; notably the increased resistance and higher energy barrier associated with translocation in this direction.
3. **Translocation Characteristics:** The calculated current modulation and dwell time of translocation events are in line with established literature. Current blockade scaled linearly with applied bias; dwell time was inversely proportional to bias, consistent with theoretical models of DNA translocation. The smaller current enhancement and longer dwell time that was observed for reverse translocation can be explained steric hindrance experienced by the DNA, resulting in greater hydrodynamic drag and a more compact conformation.

4. **Impact of Baseline Noise on Subevent Detection:** The subevent detection algorithm found no features or anomalies in the event traces. This suggests that the baseline noise of this experiment did not have a detrimental effect on subevent detection (of which there were none expected for linear DNA). For all biases, the relative frequency of detected subevents followed a smooth curve. Noise contributions effectively averaged out over the entire dataset.
5. **Suitability for Complex Analytes:** Even with low SNR, the analysis workflow was able to detect and cluster translocation events by conformation. Combined with as-expected results from subevent analysis, the translocation set-up and data analysis in conjunction seems suitable for future translocation of more complex analytes.

**Future Work**

The next logical step is to apply this optimised setup to the translocation of more complex analytes. A suitable analyte would be a structure of similar length to the 4 kbp dsDNA studied here, but with a single, distinguishable probe located off-centre along the strand. This would simplify initial analysis, while testing the ability to detect and analyse more complex structures. Beyond this, further optimisation of the liquid sample cell alongside improved characterisation of nanopipette geometry may improve SNR and sensing resolution.

## 4.6 REFERENCES


1. W. H. Pitchford, H. J. Kim, A. P. Ivanov, H. M. Kim, J. S. Yu, R. J. Leatherbarrow, T. Albrecht, K. B. Kim and J. B. Edel, *ACS Nano*, 2015, **9**, 1740-1748.
2. B. N. Anderson, O. N. Assad, T. Gilboa, A. H. Squires, D. Bar and A. Meller, *ACS Nano*, 2014, **8**, 11836–11845.
3. A. P. Ivanov, E. Instuli, C. M. McGilvery, G. Baldwin, D. W. McComb, T. Albrecht and J. B. Edel, *Nano Letters*, 2011, **11**, 279-285.
4. T. Albrecht, *Annu. Rev. Anal. Chem.*, 2019, **12**, 371–387.
5. N. A. W. Bell and U. F. Keyser, *J. Am. Chem. Soc.*, 2015, **137**, 2035-2041.
6. N. A. W. Bell and U. F. Keyser, *Nat. Nanotechnol.*, 2016, **11**, 645-651.

7. J. Kong, N. A. W. Bell and U. F. Keyser, *Nano Lett.*, 2016, **16**, 3557–3562.
8. J. Kong, J. Zhu, K. Chen, and U. F. Keyser, *Adv. Funct. Mater*., 2019, **29**, 1–6.
9. N. E. Weckman, N. Ermann, R. Gutierrez, K. Chen, J. Graham, R. Tivony, A. Heron, and U. F. Keyser, *ACS Sens*., 2019, **4**, 2065–2072.
10. A. Y. Y. Loh, C. H. Burgess, D. A. Tanase, G. Ferrari, M. A. McLachlan, A. E. G. Cass, and T. Albrecht, *Anal. Chem*., 2018, **90**, 14063–14071.
11. F. Meng, M. Li, X. Zhou and Z. Ouyang, *Chem. Phys. Lett.*, 2013, **565**, 116–121.
12. O. Otto and U. F. Keyser, in *Engineered Nanopores for Bioanalytical Applications*, ed. J. B. Edel and T. Albrecht, Elsevier, MA USA, 2013, Chapter 2 'DNA Translocation'.
13. N. A. Bell, K. Chen, S. Ghosal, M. Ricci and U. F. Keyser, *Nat. Commun*., 2017, **8**, 1–8.
14. F. Zheng, M. Alawami, J. Zhu, C. M. Platnich, J. Sha, U. F. Keyser and K. Chen, *Nano Lett*., 2023, **23**, 11145–11151.
15. K. Chen, N. A. Bell, J. Kong, Y. Tian and U. F. Keyser, *Biophys. J*., 2017, **112**, 674–682.
16. F. Zheng and Q. Han, *Analyst*, 2024, **149**, 5131-5138.
17. V. Sharma, N. Farajpour, L. S. Lastra and K. J. Freedman, *Small*, 2022, **18**, 2106803.
18. N. Ermann, N. Hanikel, V. Wang, K. Chen, N. E. Weckman and U. F. Keyser, *J. Chem. Phys.*, 2018, **149**, 163311.
19. Engineered Nanopores for Bioanalytical Applications. (2013). In *Engineered Nanopores for Bioanalytical Applications*. https://doi.org/10.1016/c2010-0-66941-0
20. D. Y. Ling and X. S. Ling, *J. Phys.: Condens.Matter*, 2013, **25**, 375102.

21. I. M. Fujinami Tanimoto, J. Zhang, B. Cressiot, B. Le Pioufle, L. Bacri and J. Pelta, *Chem.- Asian J.*, 2022, **17**, e202200888.

22. S. Confederat, I. Sandei, G. Mohanan, C. Wälti and P. Actis, *Biophys. J.*, 2022, **121**, 4882–4891.

23. X. Liu, P. Zimny, Y. Zhang, A. Rana, R. Nagel, W. Reisner and W. B. Dunbar, *Small*, 2020, **16**, 1905379.

24. H. Ma, R. J. Yu, Y. L. Ying, Y. T. Long, *J. Electroanal. Chem.*, 2022, **908**, 116086.

25. O. J. Irving, L. Matthews, S. Coulthard, R. K. Neely, M. M. Grant, T. Albrecht, *ChemBioChem*, 2023, **24**, e202300361.

26. V. Tabard-Cossa, D. Trivedi, M. Wiggin, N. N. Jetha and A. Marziali, *Nanotechnology*, 2007, **21**, 305505.

27. V. Dimitrov, U. Mirsaidov, D. Wang, T. Sorsch, W. Mansfield, J. Miner, F. Klemens, R. Cirelli, S. Yemenicioglu and G. Timp, *Nanotechnology*, 2010, **21**, 065502.

28. J. K. Rosenstein, M. Wanunu, C. A. Merchant, M. Drndic and K. L. Shepard, *Nat. Methods*, 2012, **9**, 487-492.

29. M. H. Lee, A. Kumar, K. B. Park, S. Y. Cho, H. M. Kim, M. C. Lim, Y. R. Kim and K. B. Kim, *Sci. Rep.*, 2014, **4**, 7448.

30. A. Balan, B. Machielse, D. Niedzwiecki, J. Lin, P. Ong, R. Engelke, K. L. Shepard and M. Drndić, *Nano Lett.*, 2014, **14**, 7215-7220.

31. W. Choi, E. S. Jeon, K. Y. Chun, Y. R. Kim, K. B. Park, K. B. Kim and C. S. Han, *PLoS One*, 2018, **13**, e0200831.

32. X. J. A. Janssen, M. P. Jonsson, C. Plesa, G. V. Soni, C. Dekker and N. H. Dekker, *Nanotechnology*, 2012, **23**, 475302.

33. L. Liu, X. Xie, J. Kong, H. Wu and Q. Liu, *Sci. Adv. Mater.*, 2013, **5**, 2032-2038.

34. J. Li, M. Gershow, D. Stein, E. Brandin and J. A. Golovchenko, *Nat. Mater*., 2003, **2**, 611-615.

35. L. J. Steinbock, O. Otto, C. Chimerel, J. Gornall and U. F. Keyser, *Nano Lett*., 2010, **10**, 2493-2497.

36. D. Fologea, E. Brandin, J. Uplinger, D. Branton and J. Li, *Electrophoresis*, 2007, **28**, 3186–3192.

37. P. Chen, J. Gu, E. Brandin, Y. R. Kim, Q. Wang and D. Branton, *Nano Lett*., 2004, **4**, 2293-2298.

38. S. Ghosal, *Phys. Rev. E: Stat., Nonlinear, Soft Matter Phys.*, 2006, **74**, 041901.

39. S. Ghosal, *Phys. Rev. Lett*., 2007, **98**, 238104.

40. M. Wanunu, W. Morrison, Y. Rabin, A. Y. Grosberg and A. Meller, *Nat. Nanotechnol*., 2010, **5**, 160-165.

41. B. Lu, F. Albertorio, D. P. Hoogerheide and J. A. Golovchenko, *Biophys. J*., 2011, **101**, 70-79.

42. M. Wanunu, J. Sutin, B. McNally, A. Chow and A. Meller, *Biophys J*., 2008, **95**, 4716-4725.

# 5 NANOPIPETTE SAMPLE PREPARATION AND CHEMICAL ANALYSIS

## CONTENTS

# 5.1 INTRODUCTION

Nanopipettes have several advantageous characteristics that distinguish them from other nanopores, particularly when fabricated from quartz. This is due to their needle-like geometry, the ability to achieve ultra-small pore diameters (down to 10 nm),[1,2] high mechanical strength and durability,[3] low dielectric constant,[4] low dissipation factor,[4] and relatively straightforward fabrication methods.[1,2] These properties make them ideal for diverse applications such as imaging,[5–7] sensing,[8–10] diagnostics,[11] and as microinjectors.[12–14] In all such applications, the nanopipette's performance (its precision, stability, and response) is highly reliant on the exact size, geometry, and chemical properties of its sensing region.[2]

To optimise nanopipette sensors for specific applications, the selectivity and sensitivity can be substantially improved through inner surface modifications.[15–26] Simple chemical functionalisation adjusts the ion current rectification by changing surface charges,[22,27,28] while more sophisticated modifications, such as incorporating proteins,[29] aptamers,[30,31] or nanoparticles,[32] enhance selectivity for target analytes. Integrating advancements in materials science with nanopore technology could further expand the versatility of nanopipettes. However, to realise tuneable, application-specific sensors, a deeper understanding of the surface chemistry within the nanopipette, particularly how these properties affect analyte translocation, is essential. Therefore, optimising methods to characterise the interior surface of the nanopipette's sensing region is important for advancing nanopipette-based sensor development.

## 5.1.1 CHALLENGES OF NANOPIPETTE CHARACTERISATION

Whilst the ultrasmall size, needle-like geometry and insulating materials of nanopipettes are beneficial and well-suited to their many applications, they are particularly ill-suited to chemical characterisation and pose considerable challenges. With pipette walls only tens of nanometres thick at the sensing region and tapers a few millimetres in length, exposing the nanopipette interior at the sensing region is impossible with simple, mechanical means. Such approaches often shatter the sample and destroy the area of interest, due to the brittleness of the material and nanoscale dimensions. Highly precise and specialist techniques are required to access these specific regions without compromising chemical and structural integrity.[33–35]

### 5.1.2 Focused Ion Beam Milling

Focused ion beam (FIB) milling is a technique typically used to thin and prepare bulk samples for TEM, using a finely focused beam of accelerated gallium ions. Although less common, other ion beams are available, such as plasma or helium, but gallium is most suitable for sputtering or milling applications. Regarding nanopipettes, application in the literature is usually limited to conductive nanopipette-based nanoelectrodes, where FIB milling has been used to expose the inner electrode surface and achieve precise dimensions.[19,32,36,37]

Electron beam techniques, such as SEM and TEM, are required for chemical analysis and to probe morphology at the nanoscale. However, they are usually incompatible with insulating materials, due to excessive sample charging, beam drift, and potentially sample damage.[38] As such, direct interior analysis of nanopipettes would be impossible with these techniques, highlighting the need for dedicated, optimised sample preparation methods to achieve precise chemical mapping within the inner channel.

### 5.1.3 Characterisation Techniques

Several surface-sensitive analytical techniques were evaluated for suitability, with the intended application of exploring the morphology and chemistry of nanopipette interiors. The techniques were chosen for their ability to inspect samples with sub-µm down to nm spatial resolution. These techniques were: scanning electron microscopy (SEM) with energy dispersive X-ray spectroscopy (EDX or EDS), Auger electron spectroscopy (AES), and time-of-flight secondary ion mass spectrometry (ToF-SIMS).

**Scanning Electron Microscopy/Energy Dispersive X-Ray Spectroscopy**

SEM, when combined with EDX, offers both morphological imaging and elemental analysis. In SEM, the primary electron (PE) beam generates multiple signals from the interaction volume within the specimen, that reveal various material properties. The interaction volume is the volume in which electrons from the PE beam interact with the atoms of the sample. The size of the interaction volume is primarily affected by the energy of the PE beam and the atomic number of the specimen, and further by the diameter of the primary beam (Figure 5.1).[39]

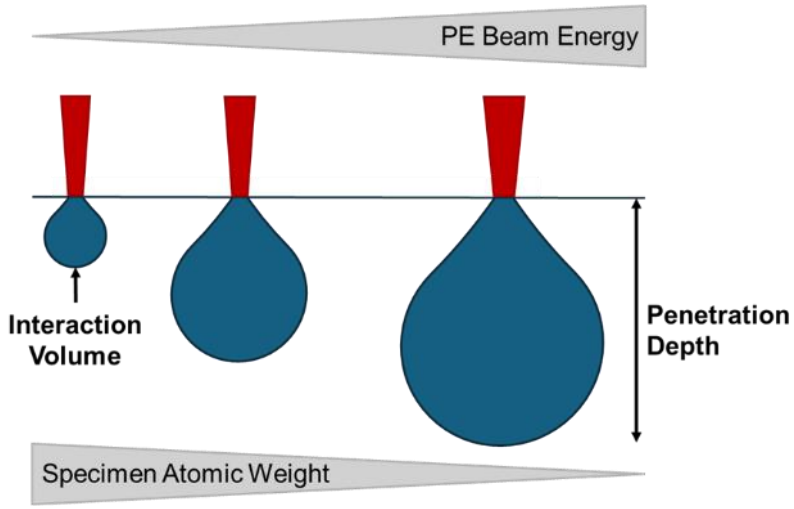


*Figure 5.1: The interaction volume is shown in blue, and the PE beam shown in red. The interaction volume and penetration depth of the PE beam is affected by the energy of the beam and the atomic weight of the specimen.*

Backscattered electrons (BSE) provide contrast based on atomic number differences, while secondary electrons (SE) yield detailed topographic information (Figure 5.2). Due to differences in energy and hence escape depth, lower energy SE capture near-surface (nm) details, whereas higher energy BSE have greater escape depths and provide bulk information with µm spatial resolution. Typical SEM operating conditions range from 1 to 30 keV, with lateral resolutions between 0.5 and 10 nm, and depth resolution from approximately 10 nm at low voltage to 1 µm at higher voltage, depending on the material.[38,39]

The process that allows for EDX has multiple steps. First, the PE beam displaces electrons from the inner shell of an atom, creating an electron vacancy. An electron from an outer shell (more weakly bound to the core) then fills this vacancy, releasing characteristic X-rays in the process (Figure 5.2). Their exact energies are determined by the specific binding energies of the electron shells of elements. These X-rays, having a larger escape depth than electrons, provide qualitative and quantitative elemental analysis and mapping. The information volume of X-rays is larger than that of SE and BSE, resulting in lateral resolutions between 30 nm and 1 µm, with micrometre-scale depth resolution under typical operating conditions. EDX can measure elemental spectra as point-analysis, line scans, and image maps or arbitrary areas, proving a versatile option for visualising chemical composition.[40]

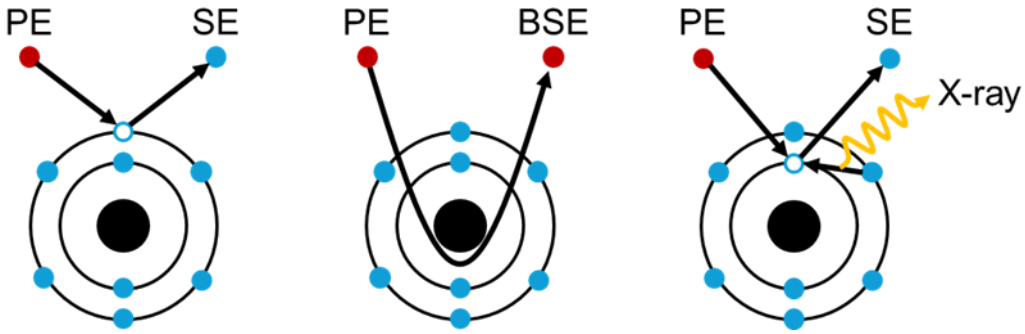


*Figure 5.2: Origin of signals in SEM/EDX. SEs originate from inelastic interactions between the PE beam and the atoms of the sample and possess low energies. BSEs are reflected back after elastic interactions between the PE beam and the sample and possess high energies. Following the emission of a SE from an atom, the resulting vacancy can be filled by a higher excitation energy electron, releasing characteristic X-rays that can be measured with EDX.*

As a technique, SEM/EDX is typically rapid and non-destructive, requiring limited sample preparation. It is frequently used for initial material characterisation, allowing for efficient assessment of material properties prior to using more surface-sensitive, specialised analytical methods.

**Auger Electron Spectroscopy**

AES is an extremely surface-sensitive technique with superior lateral resolution, where a focused primary electron (PE) beam is used to induce Auger electron emission (Figure 5.3). During this process, the PE beam displaces an electron from an inner shell of an atom, generating an electron vacancy, similar to the process for X-ray excitation (see previous section). An electron from an outer shell then drops to the lower energy shell to fill the vacancy, releasing energy that can either emit as an X-ray or transfer to a third electron, called an Auger electron. The emitted Auger electrons have kinetic energies unique to each element, allowing for elemental identification. Due to their relatively low energy, Auger electrons can escape only from the top 2–10 atomic layers, making AES highly surface-specific.[41] Furthermore, this very small escape depth induces emission of electrons only from the neck-region of the pear-like interaction volume (see Figure 5.1), whose diameter is defined by the PE beam (low nm-range). This makes AES a surface-sensitive method with excellent lateral resolution, down to 10 – 20 nm.[42,43]

AES operating conditions are typically between 3–25 keV excitation energy, with an achievable lateral resolution of 10–20 nm and a depth resolution of 1–5 nm. This high spatial resolution

makes AES suitable for detailed surface analysis and elemental mapping at the nanoscale. Additionally, AES can be combined with SEM imaging to provide simultaneous chemical and structural information. [44]

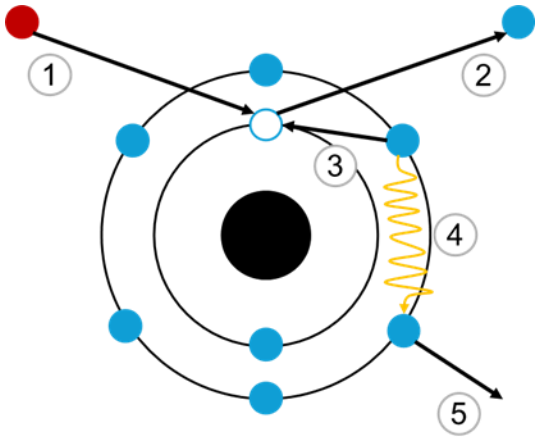


*Figure 5.3: Process of Auger electron emission. The PE beam irradiates the sample (1) and following inelastic scattering a SE electron is emitted (2). An electronic transition occurs from the outer shells of the atom to fill the vacancy (3) and as a result the atom undergoes energetic relaxation (4), giving rise to Auger electron emission (5).*

**Time-of-Flight – Secondary Ion Mass Spectrometry**

ToF-SIMS uses a pulsed primary ion beam, such as $Bi^+$ or $Cs^+$, to sputter secondary ions from the top few monolayers of a sample surface (Figure 5.4). These sputtered ions are then accelerated into a 'flight tube', where their mass is determined based on the time taken to reach the detector. In the same electrical field, lighter masses will reach the detector quicker, heavier masses more slowly, and as such this time-resolved detection can be converted into a mass spectrum. This technique offers high mass resolution and enables the simultaneous detection of ions of different masses, allowing for detailed compositional analysis.[45,46]

Operating between 25–30 keV, ToF-SIMS is also well-suited for non-conductive samples, as secondary ion or low-energy electron sources can be applied to prevent charge accumulation on insulating materials. ToF-SIMS achieves a depth resolution of approximately 1 nm and a lateral resolution between 100–500 nm, depending on instrumental settings and sample characteristics. Both ion and molecular spectra, as well as line scans, depth profiles, surface maps and even 3D sample volumes can be obtained, making ToF-SIMS highly versatile for micro- and nanoscale chemical characterisation and mapping with highest sensitivity.[46]

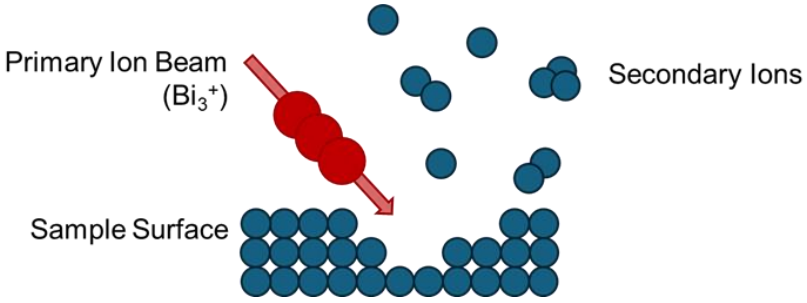


*Figure 5.4: Origin of ToF-SIMS signal. A pulsed primary ion beam sputters the outermost layers of the sample surface, releasing secondary ions and molecular fragments, to be collected by the time-of-flight analyser.*

### 5.1.4 Characterisation at the Nanoscale

SEM/EDX, AES, and ToF-SIMS each present challenges when applied to the analysis of quartz nanopipettes, particularly in terms of their depth and lateral resolution, surface and chemical sensitivity, and adaptability to nanoscale geometries. Researchers are typically most interested in the nanoscale sensing region,[47,48] which adds further complexity due to the fine spatial resolution required for accurate chemical characterization. As shown in Figure 5.5, while both ToF-SIMS and EDX may lack the sufficient nanometre-lateral resolution for the intended application, AES offers the lateral resolution necessary for detailed imaging of the sensing region.

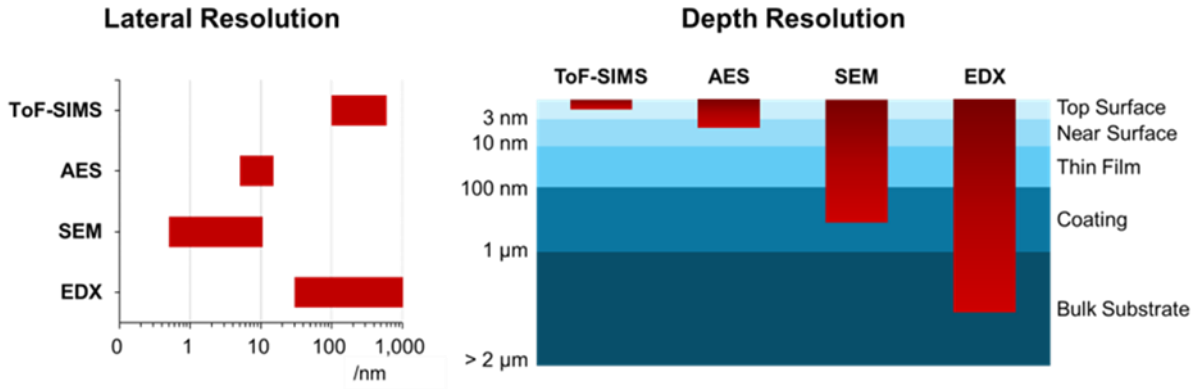


*Figure 5.5: Comparison of the resolution typically achieved for the characterisation techniques ToF-SIMS, AES, SEM and EDX. Left, the lateral resolution range and right, the depth resolution.*

When considering depth resolution, SEM and EDX are capable of probing depths up to micrometre scales, though beam condition optimization can reduce the interaction volume for more surface-sensitive analysis.[49] ToF-SIMS provides the best depth resolution for surface

analysis, with its ability to achieve atomic layer depth resolution, but it is limited by relatively poor lateral resolution, making it less suitable for imaging fine features well below 100 nm. In comparison, AES stands out as having a balanced combination of both lateral and depth resolution at the nanoscale, making it the most promising technique for characterising the interior of nanopipette sensing regions. However, the quality of the Auger signals may be limited for insulating materials, particularly for incredibly insulating materials such as quartz, and hence the achievable resolution with AES limited. It should be noted that, owing to its high sensitivity and excellent resolution, charge mitigation strategies are most crucial for AES. AES is able to detect incredibly small, low energy signals from a nanometre-scale area, and these signals are quickly obscured by high noise levels in the spectral background.

### 5.1.5 Approaches to Analysing Insulators

With electron-based techniques such as SEM/EDX and AES, insulating materials can accumulate significant charge, leading to image and spectral distortion, deflection of emitted electrons, and even sample damage.[38,39,41,50] Effective charge management is essential to obtain clear, undistorted images and accurate spectra, but achieving this can often involve a trade-off with spatial resolution, imaging conditions, sample preparation and, eventually, even with the quality of the information obtained.[38,39,49,50]

Techniques to manage charging in SEM/EDX and AES include enhancing the conductivity path, enhancing SE yield, and gentle excitation conditions, but these can reduce spatial resolution.[44] For detailed imaging of features like the nanopipette's sensing region, additional measures such as conductive coatings or modifications may be necessary, as reduced voltages and lower magnification compromise resolution.[39]

## 5.2 Aims and Objectives

The aim of this work was to obtain surface chemical and morphological analysis of the inner channel sensing region of modified quartz nanopipettes, with the following research objectives:

1. Develop a sample preparation method to minimise charging effects and enable high-resolution imaging of nanopipettes using SEM.
2. Test FIB techniques for accessing the inner channel of nanopipettes and evaluate the effectiveness of this approach with SEM.

3. Test and compare the suitability of analytical techniques EDX, AES, and ToF-SIMS, on model systems of silanised quartz slides, in order to identify the most effective methods for surface analysis of quartz.
4. Integrate the optimised sample preparation and analysis techniques to examine nanopipette samples, to develop a routine methodology (such as an SOP).

## 5.3 MATERIALS AND METHODS

### 5.3.1 PIPETTE FABRICATION

**Quartz Nanopipettes**

Quartz nanopipettes were produced from quartz glass capillaries with filaments (outer diameter: 1.0 mm, internal diameter: 0.5 mm, length: 7.5 cm, Sutter Instrument Co., USA) using a P2000 laser-based micropipette puller (Sutter Instruments Co., USA). A two-step pulling program was used to produce nanopipettes with pore sizes in the range of 50 – 100 nm, with the following parameters: (Step 1) Heat 700, Filament 5, Velocity 35, Delay 150, Pull 75; (Step 2) Heat 700, Filament 0, Velocity 15, Delay 128, Pull 175.

**Glass Micropipettes**

Glass micropipettes were produced from borosilicate glass capillaries (outer diameter: 1.0 mm, internal diameter: 0.58 mm, length: 8 cm, Science Products, Germany) using a PC-10 dual-stage glass micropipette puller (Narishige Group, Japan). A one-step heating program and dual-weight loading was used to produce micropipettes with pore sizes in the range of 150 – 300 nm.

### 5.3.2 SAMPLE PREPARATION

**Carbon Coating**

Samples were coated with a 5 nm layer of carbon using a Leica EM ACE2000 carbon thread evaporation coater (Leica Microsystems, Germany) with a pre-programmed double pulse method.

**SEM Imaging**

Images were obtained using a ZEISS Supra 40VP scanning electron microscope (Carl Zeiss AG, Oberkochen, Germany). Samples were mounted to aluminium plates with carbon adhesive

pads. Typical imaging conditions used a working distance of 2 mm, 3 kV beam energy, 30 µm aperture and SE InLens detector.

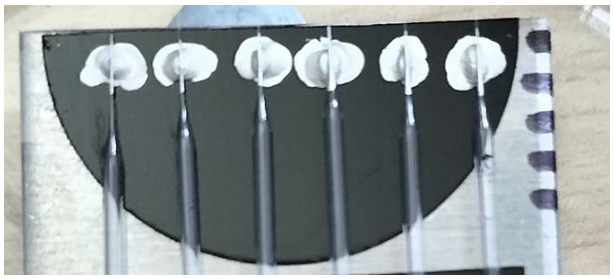

*Figure 5.6: Photograph of nanopipettes mounted on an aluminium plate, with cardon adhesive pads, silver paste bridging the nanopipette tip, and 5 nm carbon coating.*

### 5.3.3 FIB Manipulation

Pipettes were transferred to FIB sample stubs and fixed with carbon adhesive pads. With a Quanta 3D FEG dual-beam FIB-SEM (Thermo Fisher Scientific, USA), a gallium ion beam was used to mill away regions of the pipette channel wall and expose the inner surface of the pipette sensing region (Figure 5.7). Typical optimised beam conditions used were 16 kV beam energy and 0.1 nA beam current.

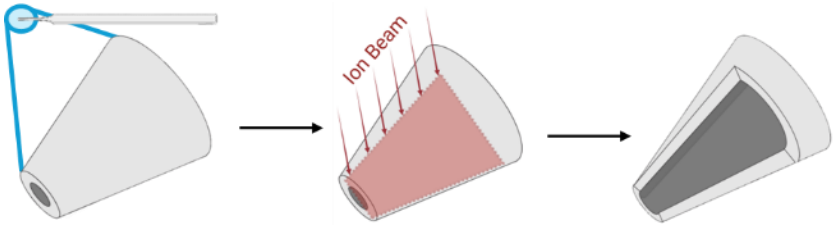


*Figure 5.7: Workflow of FIB milling a nanopipette sample. The ion beam is directed, from above, along one half of the nanopipette channel. This is then milled away, leaving the other half of the channel intact. Following FIB milling, the sample is rotated 90 º, so the exposed inner channel is facing up, perpendicular to the SEM/EDX and AES electron beam.*

### 5.3.4 Surface Silanisation

Quartz slide and nanopipette samples were first $O_2$ plasma cleaned for twenty minutes. A vial of 0.5 mL 3-(trimethoxysilyl)-1-propanethiol (Sigma-Aldrich, Merck Group, USA) was introduced to the vacuum chamber, and the vacuum held for thirty minutes.

To determine if silanisation had successfully taken place, the contact angle of water on the surface of the quartz slides was measured with the sessile drop method (Figure 5.8). A droplet of MilliQ water was placed on the quartz slide surface, either plasma cleaned or silanised, and a photograph taken. The contact angle was determined from the photograph using ImageJ software.[51]

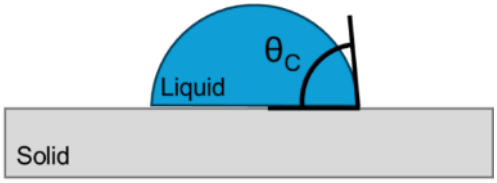


*Figure 5.8: Diagram showing the contact angle, $\Theta_C$, of a droplet on a solid surface.*

### 5.3.5 Characterisation Techniques

**EDX Measurements**

EDX spectra and elemental maps were obtained using a Zeiss Supra 40VP scanning electron microscope with a Thermo Scientific EDS spectrometer with an UltraDry silicon-drift detector (SDD) (Thermo Fisher Scientific, USA). Data analysis was performed with Thermo Scientific Pathfinder X-ray Microanalysis software (Thermo Fisher Scientific, USA). Typical operating conditions were 13 mm working distance, 5 – 10 kV beam energy, 30 µm aperture and a minimum of 3 minutes acquisition time per spectra.

**ToF-SIMS Measurements**

Measurements were obtained with an M6 ToF-SIMS (IONTOF, Germany) at the SupraFAB Surface Analytics Unit, Freie Universität Berlin. Nanopipette samples and quartz slide samples were affixed to the ToF-SIMS sample plate with copper tape.

**AES Measurements**

Measurements were obtained with a PHI 700 Scanning Auger Nanoprobe (Physical Electronics/ULVAC-PHI, Germany).

## 5.4 RESULTS AND DISCUSSION

### 5.4.1 NANOPIPETTE SAMPLE PREPARATION

To reduce charging effects and prevent beam-related artifacts during SEM imaging, several methods were explored to improve the electrical conductivity of the nanopipette samples. Initially, untreated glass micropipettes were imaged as a baseline. As shown in Figure 5.9(A), the glass micropipette was mounted on an aluminium-tilted sample stub with carbon tape. It was found that the imaging quality was poor, owing to charging of the insulating material (the glass of the pipette). The geometry of the nanopipette proved a fundamental inconvenience for sample mounting. The sample region of interest, the nanopipette tip, is 'floating' and does not benefit from the electrical contact between the pipette bulk and the substrate. Furthermore, owing to the sample's mechanical fragility, bringing the floating tip into contact with the substrate is incredibly difficult.

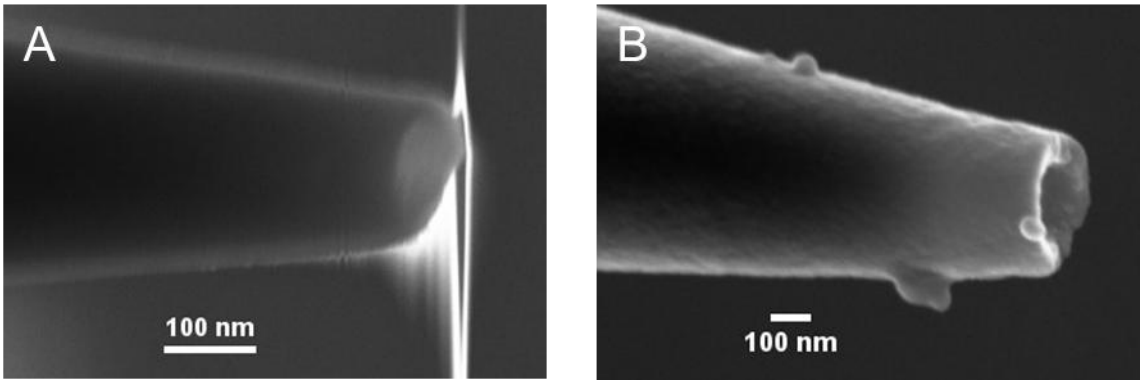


*Figure 5.9: A) SEM image of a glass micropipette with no modification, mounted only on a sample stub and adhered with carbon tape. B) SEM image of the same glass micropipette after application of silver paste and carbon coating. Scale bars read 100 nm, both images were obtained with the following imaging conditions: 3 keV, 30 µm lens aperture, SE InLens detector, 3 mm working distance. Note, image (A) obtained with 120,000 x magnification, and image (B) with 100,000 x magnification, hence discrepancy between scale bar sizes.*

To address this, the conductivity was enhanced by bridging the floating pipette tip to the carbon tape using silver paste, followed by a 5 nm carbon coating over the sample surface. This combination effectively minimised charging, improving image stability and detail resolution. The results, shown in Figure 5.9(B), made higher magnification imaging possible. This allowed

for a more detailed examination of surface features, including the jagged edges at the nanopore opening and minor contamination seen on the outer surface.

However, the initial method of mounting the nanopipette with silver paste, though effective in securing the sample and improving conductivity, introduced limitations. Silver paste, in fixing the sample in place, prevents flexibility in sample handling and further preparation. In addition to this, the manual application of silver paste had previously damaged nanopipette tips during mounting.

To address this, a 5 nm carbon coating was applied directly to the quartz nanopipettes, without the use of silver paste. The SEM images obtained after carbon coating (but without silver paste) showed an improvement in levels of charging and imaging stability when compared to uncoated samples (see Figure 5.10). However, a minor reduction in image detail compared to the silver-pasted samples was noticeable. The absence of silver paste slightly limited conductivity enhancement but offered a practical advantage by preserving the nanopipette's structure and flexibility in handling.

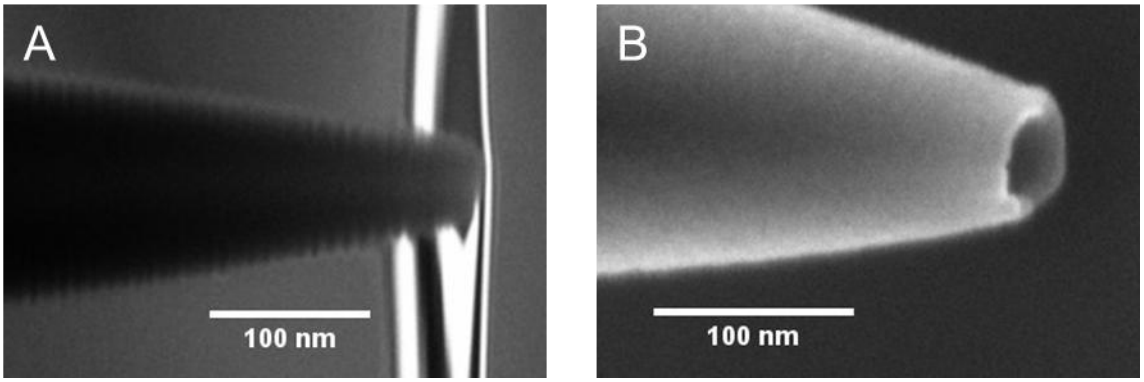


*Figure 5.10: A) SEM image of a quartz nanopipette with no modification, mounted only on a sample stub and adhered with carbon tape. B) SEM image of the same quartz nanopipette after carbon coating, demonstrating improved resolution (tip diameter is approximately 25 nm, with pore walls approximately 10 nm thick). Scale bars read 100 nm, both images were obtained with the following imaging conditions: 3 keV, 30 µm lens aperture, SE InLens detector, 3 mm working distance.*

Following optimisation, the most suitable SEM imaging parameters were identified as a 3 keV acceleration voltage, a 30 µm aperture, and the use of an SE InLens detector. An acceleration voltage of 3 keV was chosen as this provided enough energy to resolve surface features, whilst minimising the risk of beam-induced charging and potential sample damage. The 30 µm

aperture allowed for a focused beam with reduced current density, when combined with quick scan speeds and integration of frames, which is better suited to observing delicate samples. Finally, the SE InLens detector is surface sensitive and suitable for low voltage operation. This combination of parameters gave the best results for imaging nanopipette tips, achieving a balance between charge suppression and sufficient detail resolution to allow further analysis.

### 5.4.2 Focused Ion Beam (FIB) Milling

To gain access to the nanopipette's inner channel, focused ion beam (FIB) milling was used to remove half of the channel and create a 'window' to the interior. After testing different beam parameters, the most effective gallium ion beam settings were determined to be 16 kV with a 0.1 nA current. This combination allowed for rapid and controlled milling to reduce beam drift issues, while preventing excessive beam exposure times. However, attempting to mill the sensing region closest to the nanopore proved difficult. Despite the optimised settings, the thinness of the walls often led to deformation and melting. This rendered it difficult to create a precise opening into the sensing region.

To avoid damaging the sample, FIB milling was performed further up the nanopipette taper, where the pore walls are thicker (upwards of 100 nm). This allowed for greater control over the final result and a more effective milling process. The gallium ion was used to mill away one half of the nanopipette channel wall along its axis, creating a 'window' approximately 2 μm in length. This was able to provide a clear view of the interior surface, yet also maintained the overall structural integrity of the nanopipette. This is shown in Figure 5.11, where Figure 5.11(A) shows the initial carbon-coated nanopipette, Figure 5.11(B) displays the milled channel wall, and Figure 5.11(C) shows the exposed interior of the nanopipette after sample rotation.

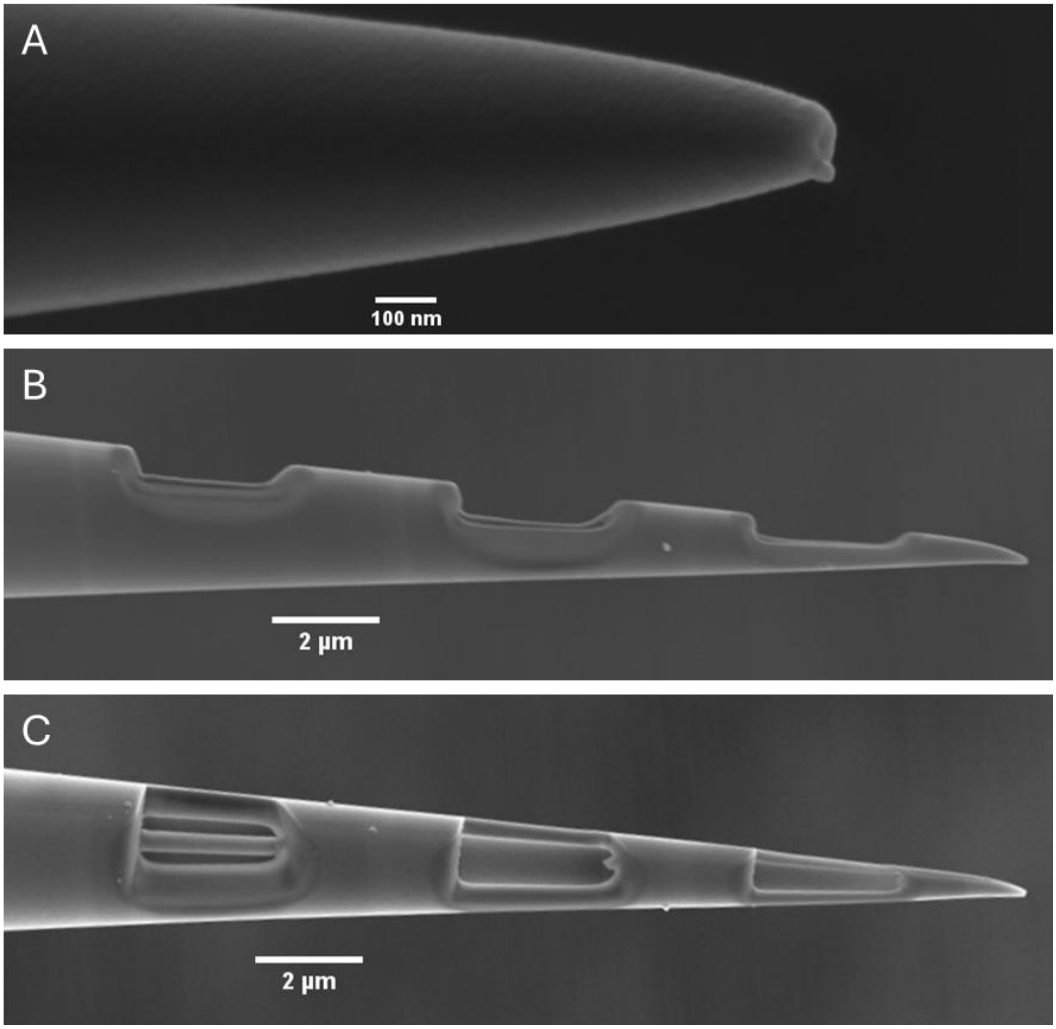


*Figure 5.11: SEM images of, A) carbon coated quartz nanopipette prior to FIB milling, B) nanopipette with three milled 'windows', C) milled nanopipette rotated 90 º to expose inner channel to the SEM beam and top SE In Lens detector. In the left window, the internal quartz filament remained intact. Images obtained with the following imaging conditions: 3 keV, 30 µm lens aperture, SE InLens detector, 3 mm working distance.*

### 5.4.3 Chemical Analysis of Model Samples

To reduce the complexity that would be introduced by nanopipette size, geometry and fragility, flat quartz slides were first adopted as a model system for study. This was designed to help simplify initial testing and optimisation of analytical techniques.

**Surface Silanisation and Contact Angle Measurements**

To create a flat quartz surface that was chemically comparable to a modified quartz nanopipette, the surface was exposed to a thiol-terminated organosilane (Figure 5.12) with a vacuum-

deposition method. The resulting organosilane monolayer provided a thin, chemically distinct layer for further chemical analysis. The contact angle of water droplets on both clean and modified quartz slides was measured and used to confirm the presence of the monolayer (Figure 5.13). Measuring contact angles is a simple and effective method for assessing changes to surface hydrophilicity or hydrophobicity as a result of surface modification.

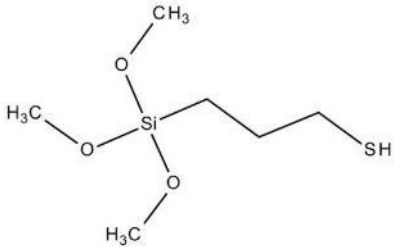


*Figure 5.12: Chemical structure of 3-(trimethoxysilyl)-1-propanethiol.*

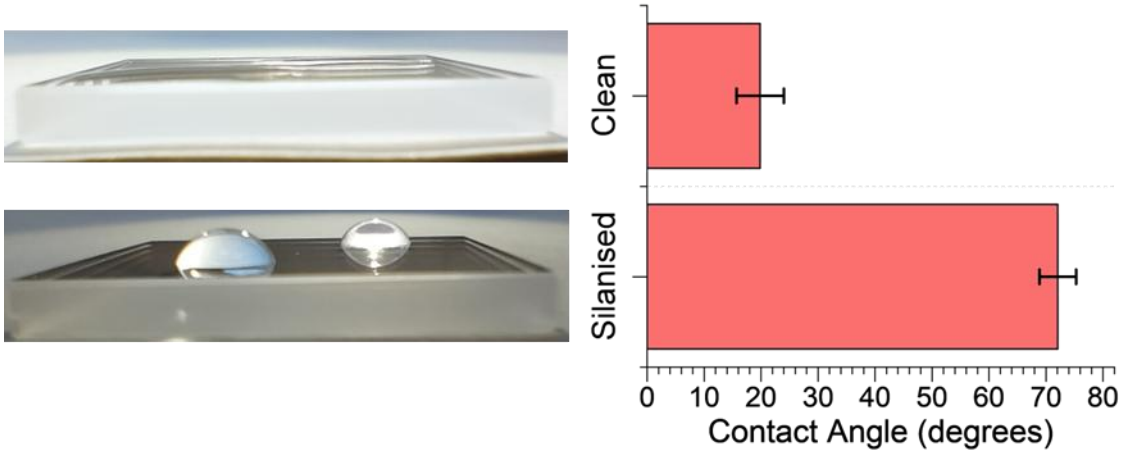


*Figure 5.13: Images of water droplets on a plasma-cleaned quartz slide and a silanised quartz slide, with contact angle measurements.*

For the clean quartz slide, the measured contact angle of the water droplet was 19.8 ± 4.2º. this is indicative of a hydrophilic surface, as expected due to the presence of exposed siloxane groups on the sample surface. Following modification with the hydrophobic organosilane monolayer, the contact angle increased to 72.0 ± 3.2º. Again, this is an expected result as the hydrocarbon chain reduces the interaction between the surface and the water droplet. These measurements confirmed the presence of the organosilane layer.

The vapour-phase deposition method has better reproducibility than liquid-phase and typically produces more homogenous monolayer surfaces with greater stability.[52] It must be noted, however, that the surface chemistry of organosilanes is complicated and a monolayer formation

cannot be guaranteed. Many factors can affect the uniformity and thickness of organosilane layers, such as silane concentration, tail groups, humidity and desorption from the surface over time.[52] As such, full surface monolayer coverage cannot be guaranteed, as gaps in surface coverage or dense, multilayered regions may be present. For simplicity and to aid in analysis, the organosilane coverage is referred to as and considered to be a monolayer, but note that this description better represents the 'average' of the organosilane coverage over the whole surface.

**EDX Spectroscopy**

The first chemical characterisation technique to be tested was EDX. The technique was chosen for initial study because of its ability to operate at low electron beam voltages, which allows for sensitive probing of the sample surface. Furthermore, these conditions were intended to minimise surface charging and prevent potential damage to the insulating quartz sample. The EDX spectrum acquired for a clean quartz slide is shown in Figure 5.14. As expected, the spectrum displays the elemental composition of quartz, showing prominent peaks for silicon and oxygen. However, the signal yield was relatively low due to the reduced electron beam energy used in this analysis, only 5 keV.

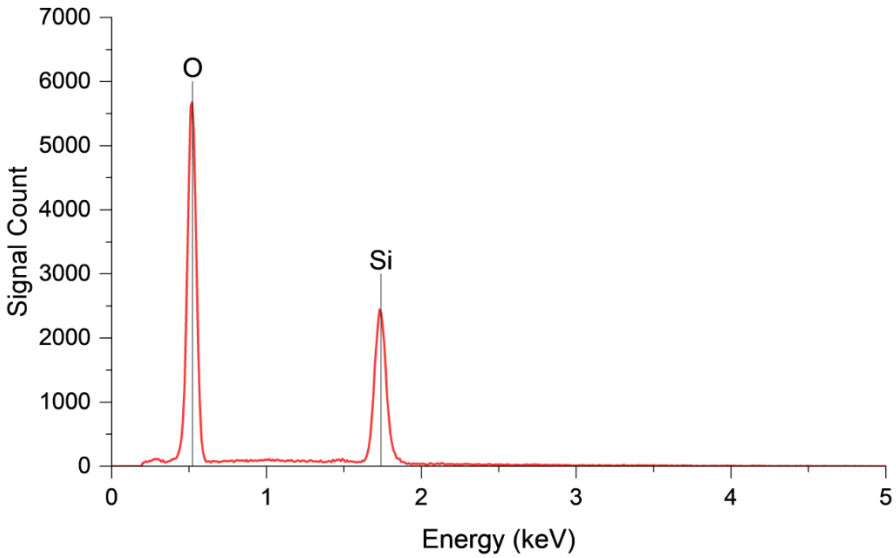


*Figure 5.14: EDX spectrum of a clean quartz slide at 5 keV, data acquisition time 2 minutes.*

When the EDX spectrum was obtained at higher voltages, an increase in signal count was observed. However, this improvement in signal intensity came at the expense of increased surface charging effects, which affected the stability of acquisition and limited the duration of

point scans. To balance these factors, a relatively low voltage (5 kV) was selected as the optimal setting, as it allowed for longer acquisition times to increase signal count, with reduced levels of charging. A further decrease in beam energy was not possible, as the PE beam energy would not be high enough to excite the necessary X-ray emissions for chemical elements of interest.

To further investigate the surface sensitivity of EDX, the same analysis conditions were applied to a silanised quartz slide, this time with an extended acquisition period of 1 hour (Figure 5.15). Based on the chemical structure of the organosilane, an increase in the oxygen peak was anticipated, along with detectable signals for carbon and sulphur as a marker element. The spectrum does display a small carbon peak and an enhanced oxygen signal, as well as a slight aluminium peak attributed to the sample mount surrounding the quartz slide. However, the sulphur peak, while expected based on the thiol-terminated silane layer, is not readily visible at this scale.

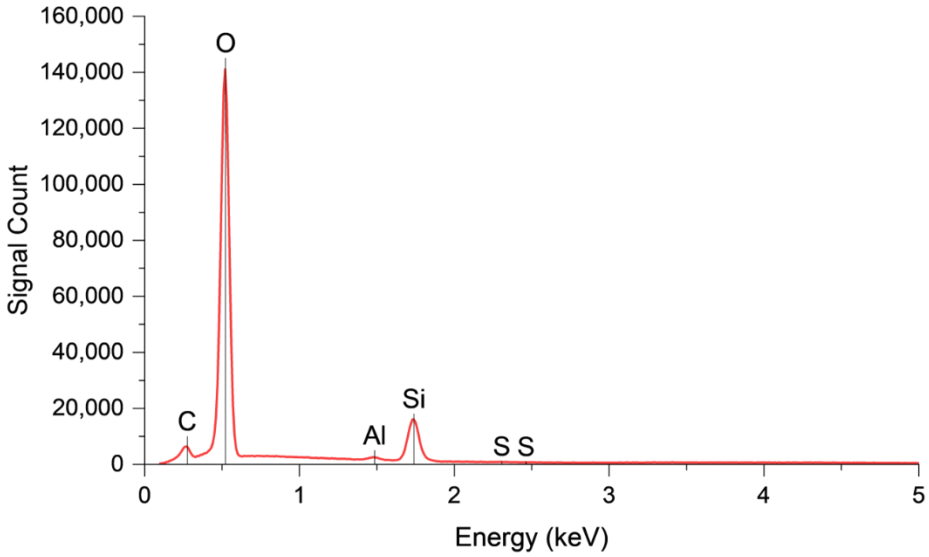


*Figure 5.15: EDX spectrum of a silanised quartz slide at 5 keV, data acquisition time 1 hour.*

A more focused analysis of the EDX signal in the region where sulphur peaks are expected is provided in Figure 5.16, which shows both the raw signal and a five-point moving average. A very slight sulphur peak is observed above the Bremsstrahlung background, with a more pronounced signal around the 2.307 keV peak than the 2.464 keV peak, as expected for S Kα and S Kβ characteristic lines, with an intensity ratio of roughly 5:1. These findings indicate that a sulphur monolayer, or thin multilayer, particularly on an insulating surface prone to high background noise, lies at the detection threshold for EDX.

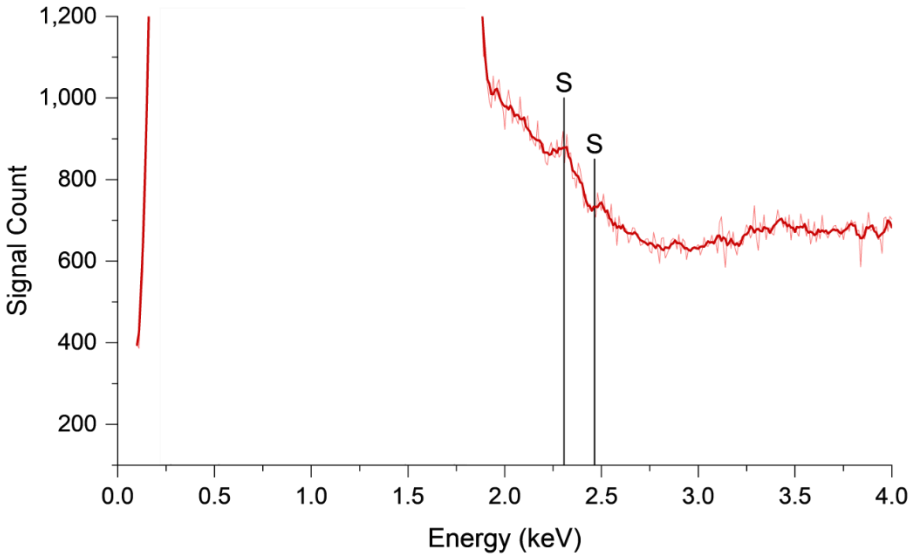


*Figure 5.16: EDX spectrum of a silanised quartz slide, focusing on the sulphur peak region, with the more pronounced S Kα signal at lower energy, and the S Kβ signal (which was not observed) at higher energy. Acquired at 5 keV, 1 hour acquisition time.*

This result is in agreement with the known limitations of EDX. At low PE beam voltages, the penetration depth is significantly reduced, thereby limiting primary excitation to the sample's surface and sub-surface region. While this lowers the overall signal yield, it confines the excitation region from the surface to tens of nanometres in depth, making it possible to detect signals from a monolayer of sulphur, albeit at the technique's sensitivity limit. Operating at higher voltages would have increased signal count but with a higher contribution from the bulk, obscuring the subtle sulphur signal. Thus, the low-voltage approach (5 keV) was the best compromise available, balancing depth resolution with signal yield.

**ToF-SIMS**

ToF-SIMS, in contrast to a microbeam analysis technique such as SEM/EDX, offers highly surface-specific analysis, ideal for detecting thin surface layers and trace elements. Figure 5.17 displays element maps for oxygen and sulphur ions obtained through ToF-SIMS, in the negative ion detection mode, from both clean and silanised quartz slide samples.

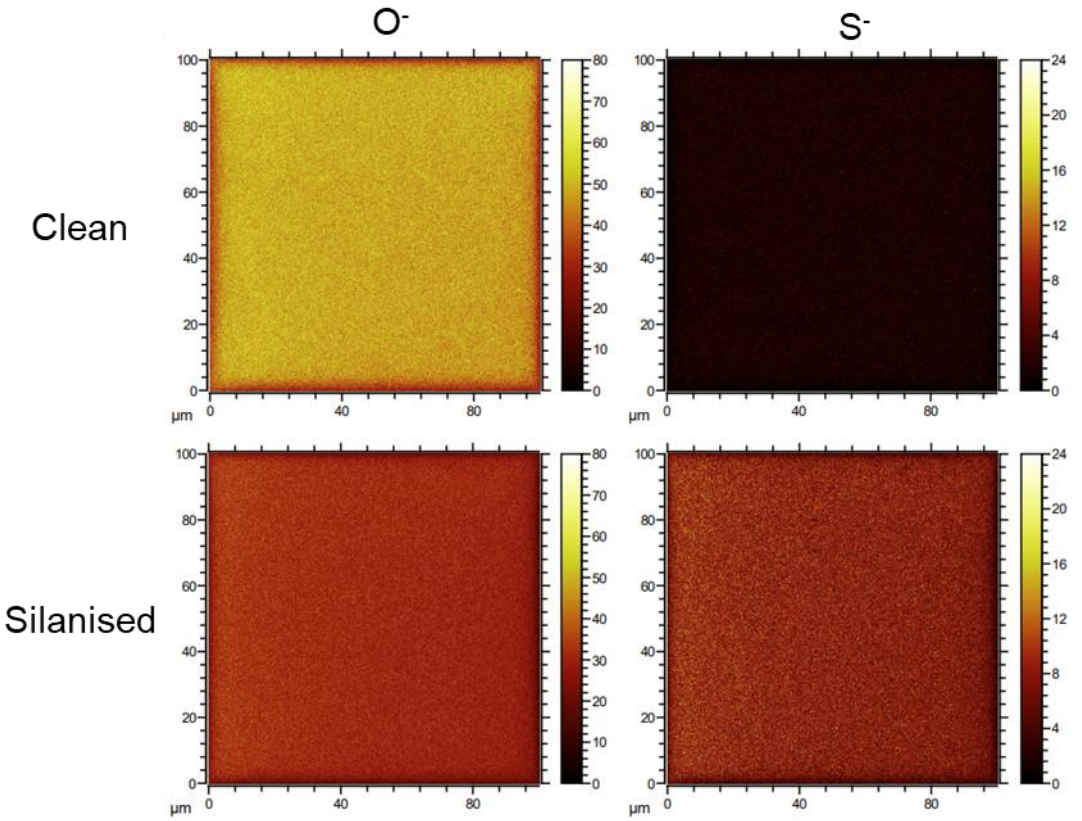


*Figure 5.17: Elemental maps of oxygen and sulphur ions on both a clean and silanised quartz slide.*

As anticipated, the clean quartz slide shows only oxygen, with no sulphur detected, consistent with EDX results. For the silanised quartz sample, ToF-SIMS confirms the presence of sulphur from the organosilane monolayer, with a distinct sulphur signal that was difficult to detect with EDX. This distinction highlights ToF-SIMS's superior surface sensitivity, allowing for more conclusive identification of surface-modifications, even when present in trace amounts as a monolayer at the sample surface.

Additionally, ToF-SIMS includes in situ charge-neutralization capabilities, which helps mitigate surface charging during analysis—a notable advantage over both EDX and AES. While sulphur signal counts were relatively low with both EDX and ToF-SIMS, the latter's charge compensation feature contributed to reduce background noise and increase the signal-to-noise ratio. This ability to neutralize charge during acquisition further supports ToF-SIMS as a more effective technique for surface-specific analysis of monolayer modifications on insulating substrates.

**AES**

AES offers high lateral and depth resolution but is susceptible to charging effects when applied to insulating materials, particularly quartz. To address this, various sample preparation techniques and beam conditions were tested to mitigate charging, with conditions and experimental outcomes summarised in Table 5.1.

| **Sample Preparation** | **Beam Conditions** | **Outcome** |
|---|---|---|
| Steel grid | 5 keV, 1 nA | High levels of charging; spectra not repeatable |
| Copper conducting tape | 5 keV, 1 nA;<br>10 keV, 10 nA | Poor conductivity; spectra not repeatable |
| 2 nm platinum coating | 5 keV, 1 nA;<br>10 keV, 10 nA;<br>10 keV, 10 nA with Ar sputtering | High noise; low signal-to-noise ratio |
| 2 nm platinum coating & 2 nm carbon coating | 5 keV, 1 nA;<br>10 keV, 10 nA | Peak shifts due to charging; high background noise |

*Table 5.1: Summary of sample preparation and beam conditions tested for AES analysis of unmodified quartz slides.*

The results of these tests highlight the challenges associated with achieving high-quality spectra for chemical analysis of insulating materials. The primary reason these approaches failed was due to insufficient charge dissipation, resulting in charging artifacts and poor spectrum quality.

Varying beam conditions (5 kV, 1 nA and 10 kV, 10 nA) had minimal impact on signal quality. It was noted that at higher beam energies, a slight improvement in signal-to-noise ratio was observed, but only when combined with sample coatings. However, even with coatings, baseline noise levels remained too high for sensitive chemical analysis.

The choice of widely available preparation techniques that are easy to apply, such as steel grids and copper conducting tape, proved largely ineffective for charge mitigation. Coating the samples with 2 nm of platinum, or a combination of platinum and carbon, resulted in a small improvement in spectrum quality, while argon sputtering demonstrated the most improvement

of all methods tested. Despite this, none of the conditions tested produced usable spectra of sufficient quality for chemical analysis.

### 5.4.4 Application to Quartz Nanopipettes

Following the preliminary chemical characterisation of flat quartz slides, these techniques were integrated with nanopipette sample preparation in order to obtain chemical spectra and maps of the nanopipette's inner channel.

**EDX Spectroscopy**

The sample preparation process involved mounting the nanopipette on an aluminium plate, adhered with carbon tape. The sample was then plasma cleaned, followed by vacuum deposition of organosilanes. To prepare the nanopipette for morphological imaging and chemical analysis, it was coated with a 5 nm layer of carbon, after which gallium ion FIB milling was used to expose the inner channel. The analysis area was selected on the ‘window’ created by the FIB, as highlighted in red in Figure 5.18, to capture elemental and spectra and maps of the region.

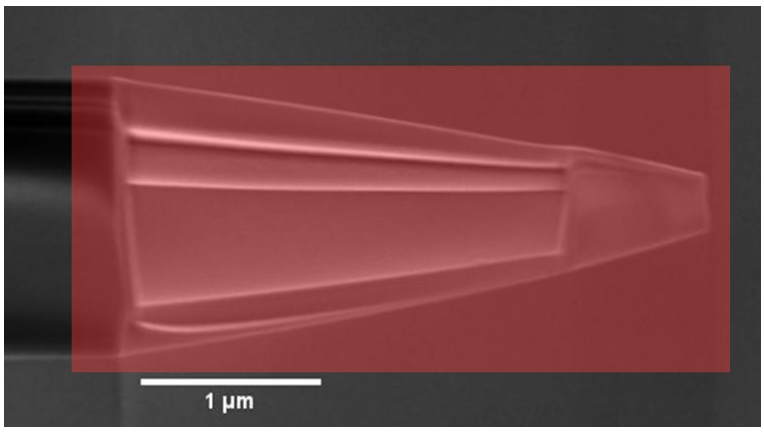


*Figure 5.18: SEM image of a silanised and milled quartz nanopipette, with the EDX analysis region highlighted in red. Visible below the upper cut-edge of the ‘window’ is the internal quartz filament.*

The region selected for analysis by EDX encompassed the 'window' to the inner channel, the milled portion of the nanopipette walls, the outer surface of the nanopipette on either side of the ‘window’, and a portion of the aluminium plate beneath the sample. The goal was to obtain a chemical overview of the sample, identifying elements such as carbon, oxygen, silicon, sulphur, and potentially gallium from the FIB ion beam. The resulting EDX spectrum of the entire scanned area is shown in Figure 5.19.

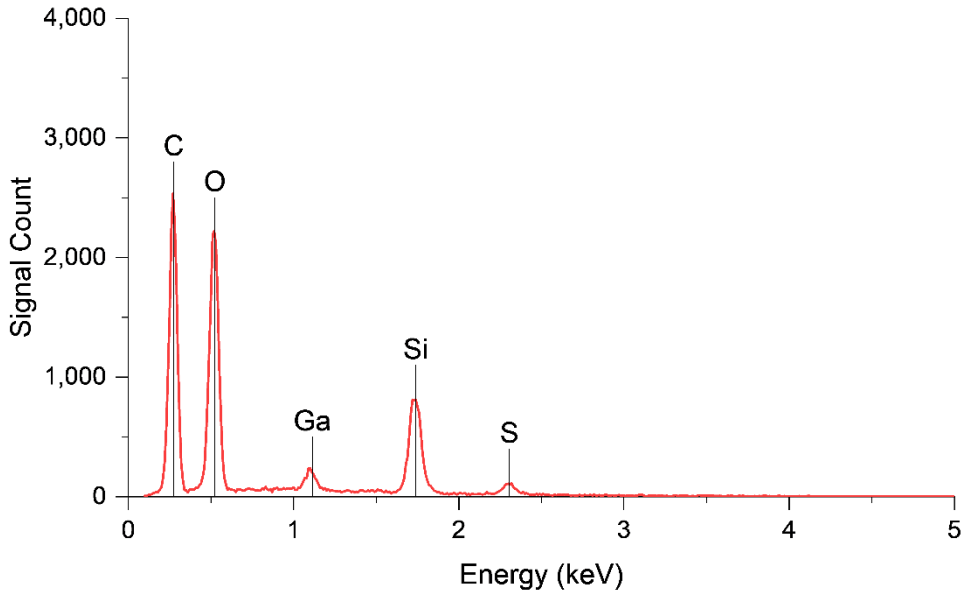


*Figure 5.19: EDX spectrum of the analysis region (highlighted in red, Figure 5.18) of a silanised nanopipette. Acquired at 5 keV, 5-minute acquisition time.*

As expected, the EDX analysis detected the presence of oxygen and silicon, consistent with the material composition of the quartz nanopipette. Interestingly, the sulphur signal was notably higher than expected from a monolayer of organosilane, especially when compared to the previous EDX spectrum of silanised quartz slides (Figures 5.15 and 5.16). This suggested that the organosilane deposition process may have led to some unintended deposition on the surrounding carbon tape.

The corresponding EDX elemental map, shown in Figure 5.20, highlights key features of the EDX analysis. The carbon signal was predominantly localized to the region surrounding the nanopipette, corresponding to the carbon tape beneath the sample. The oxygen signal was denser in regions containing more quartz, such as the uncut regions of the nanopipette and the exposed edges of the quartz wall. As expected, the gallium signal, although low in intensity and prone to noise, was localized to the cut edge of the nanopipette where the FIB milling occurred, suggesting gallium implantation from the ion beam, a well-known FIB artifact. This contamination is limited to the milled edge and is not expected to significantly affect the accuracy of chemical characterization in the interior regions of the nanopipette. Lastly, the sulphur signal was more prominent in the regions surrounding the nanopipette, likely originating from the carbon tape beneath, rather than from the nanopipette itself. This

observation suggests that during the vacuum deposition process, the organosilane may have been deposited onto the carbon tape, contributing to the elevated sulphur signal in these regions.

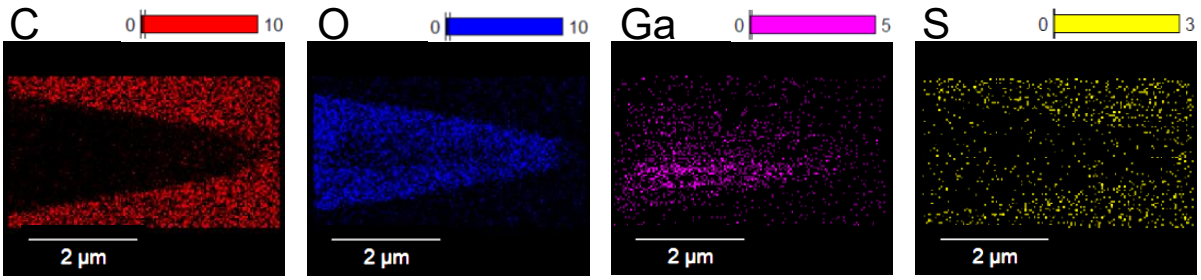


*Figure 5.20: Elemental maps of C K, O K, Ga L and S K X-ray lines.*

The unexpected sulphur signal in regions outside the nanopipette indicated the need for further refinement of sample preparation. To solve the issue of contamination observed in the initial EDX analysis, the nanopipette sample was transferred from the contaminated aluminium plate to a clean one. The nanopipette was mounted on this new plate using carbon tape, with additional copper tape placed beneath the floating nanopipette tip. A 'point' analysis was then performed on the inner channel of the nanopipette, with the point of analysis highlighted in red in Figure 5.21.

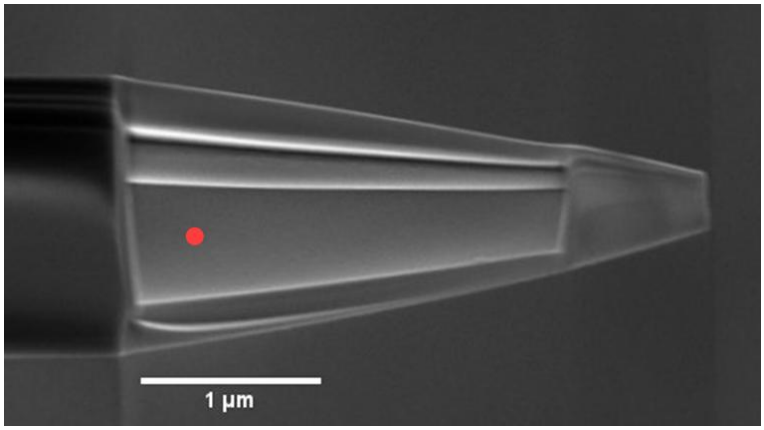


*Figure 5.21: SEM image of a silanised and milled quartz nanopipette, with the EDX point of analysis highlighted in red.*

The resulting EDX spectrum from the point analysis is shown in Figure 5.22. The detected carbon signal could have originated from different sources: the organosilane monolayer on the nanopipette surface, the 5 nm carbon coating on the nanopipette's outer surface, and contamination (accumulated between plasma cleaning the sample, transfer to the FIB, followed by transfer to the SEM, and further sample handling). The oxygen and silicon signals are, again, attributed to the quartz material of the nanopipette. The copper signal was detected from the

copper tape placed underneath the nanopipette, though its intensity was relatively low. Importantly, no sulphur peak was observed above the spectra background, as highlighted in Figure 5.22.

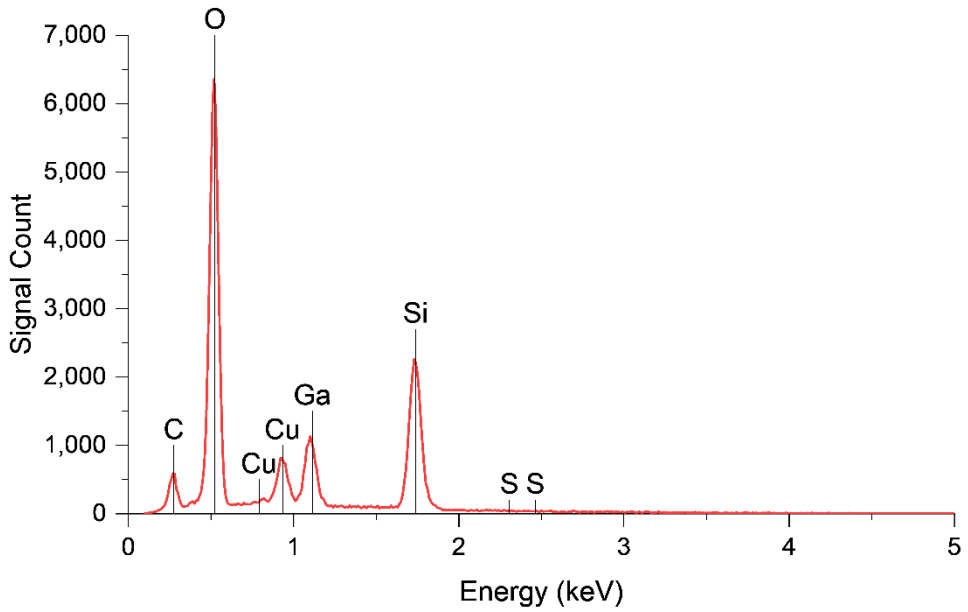


*Figure 5.22: EDX point analysis (highlighted in red, Figure 5.21) of a silanised nanopipette. Acquired at 5 keV, 5-minute acquisition time.*

This absence of a sulphur signal, which was similarly noted for the modified quartz slide, is further examined in Figure 5.23, which focuses on the sulphur region of the spectrum. To reduce the effect of background noise, a five-point moving average was applied to the as-recorded spectrum. Despite this, no sulphur was detected in the spectrum, likely due to the reduced surface area of the nanopipette sample. This challenge is compounded by factors such as the sample's surface geometry and size. For comparison, the EDX scan of the quartz slide was conducted over a much larger region (512 µm by 384 µm) with signal collection for 1 hour. Even under these conditions, the sulphur peak was weak and difficult to distinguish from background noise.

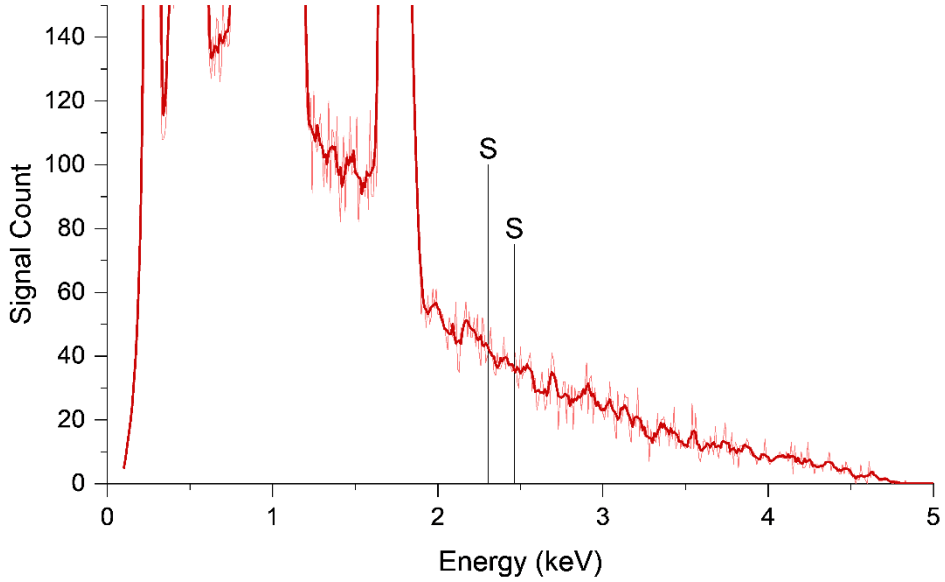


*Figure 5.23: EDX spectrum of the silanised nanopipette, focusing on the sulphur peak region. Acquired at 5 keV, 5-minute acquisition time.*

In contrast, the spectrum shown in Figures 5.22 and 5.23 was obtained from a point analysis, with a beam width in the range of 100 nm to 1 µm, and signal collection was limited to only 5 minutes due to beam drift. This highlights the limitations of EDX for detecting a monolayer of sulphur on a sample with such a small surface area. The interaction volume and depth resolution of the 5 keV electron beam relative to specimen dimensions, combined with the reduced data collection time due to charging effects lowering the signal-to-noise ratio, made it challenging to detect sulphur at the desired sensitivity. As such, EDX was found unsuitable for accurate surface sulphur quantification on such small, thin samples, confirming that it was not appropriate for this application.

**ToF-SIMS**

ToF-SIMS was also tested with nanopipette samples. However, the poorer lateral resolution (100 – 200 nm) combined with the nanopipette geometry and size posed a problem. To evaluate the resolution achievable for such a sample, the molecular signal was monitored as the incident ion beam was moved along the length of the nanopipette. The sample stage height was gradually adjusted to keep the beam focused on the sample surface as it moved along the taper. The total ion signal and $HS^-$ maps are shown in Figure 5.24.

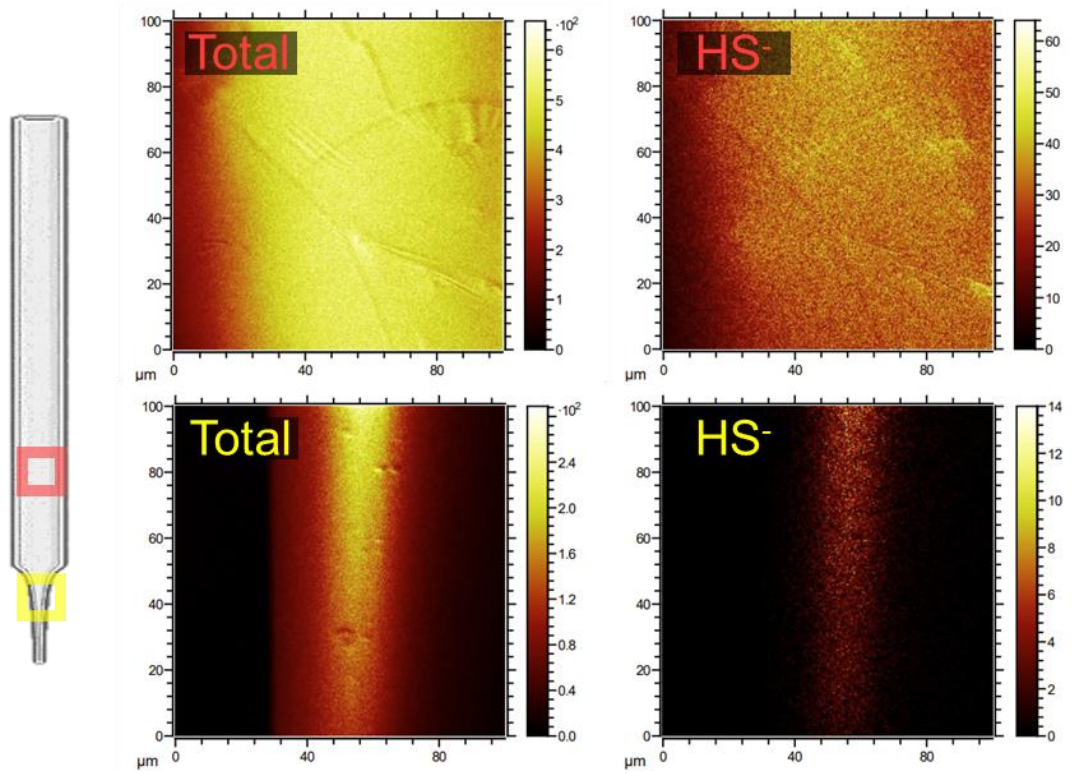


*Figure 5.24: ToF-SIMS maps of total ion count and $HS^-$, for the bulk capillary portion of the nanopipette (highlighted with a red box) and the taper region (highlighted with a yellow box). For both, signal acquisition and analysis regions were the same size, on the outer surface of the nanopipette.*

The red box in Figure 5.24 highlights the region where the molecular ion map was collected from the nanopipette's bulk region on the outer surface. The total ion signal map exhibits a relatively good signal count, but some shadowing effects are visible due to the strong curvature of the nanopipette surface. The $HS^-$ signal map confirms the successful deposition of the organosilane on the nanopipette surface. The apparent slight inhomogeneity in the organosilane layer aligns with the surface features seen in the total signal map. These are likely due to overlapping and 'bunching' of the carbon layer from the coating, after the silanisation process.

The yellow box in Figure 5.24 marks the region where the molecular ion map was collected from the taper region of the nanopipette, approximately 80 µm wide. As expected, the increased curvature at this point results in a decreased total ion signal and $HS^-$ signal, which is confined to the highest point of the outer surface. This decrease in signal was particularly evident as the ion beam was moved closer to the sensing region and the 'window' cut into the sample, with the molecular signal eventually disappearing. Despite adjusting the sample stage height to try

to compensate for the tapering, the signal intensity decreased too much to obtain meaningful data.

Furthermore, ToF-SIMS lacks the ability to perform SEM imaging, which would have been useful for aligning the sample relative to the ion beam, as is possible with EDX and AES. Only an optical microscope is available with the ToF-SIMS system, which does not offer sufficient resolution to align the sample with the ion beam accurately for the region of interest.

**AES**

It was initially hypothesized that the relatively thin walls of the nanopipette sensing region (<100 nm) would allow the primary electron (PE) beam to pass through the material at higher voltages (e.g., 10 keV), preventing excessive charge accumulation. However, throughout the experiments there were persistent charging issues that complicated both imaging and AES analysis. More importantly, the higher energy beam induced sample melting and deformation, as evident in Figure 5.25(B). This thermal damage highlights the limitations of the approaches tested, as reducing the beam energy to avoid such effects would limit the excitation of Auger electron emission necessary for analysis.

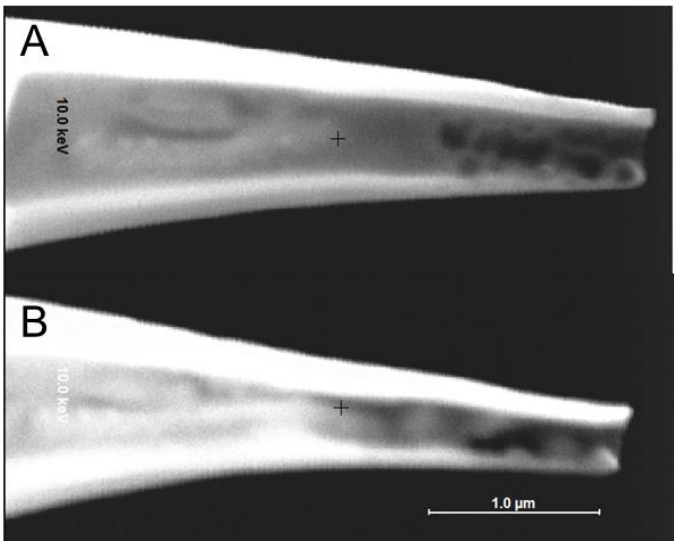


*Figure 5.25: In situ SEM images obtained during AES experiments. A) nanopipette sample prior to AES and B) after AES, demonstrating damage to the sample. Beam energy: 10 keV.*

To address these challenges, further research into advanced sample preparation methods is required to improve compatibility of nanopipettes with AES.

## 5.5 CONCLUSIONS AND FUTURE WORK

The chemical and physical properties of the nanopipette sensing region are poorly understood, and within the field of nanopore sensing there is a need to develop analytical techniques that would allow for these fundamental studies into effects of modification and impact on sensor response. This chapter presented an investigation into the preparation, chemical characterisation and morphological characterisation of quartz nanopipettes using several surface-sensitive techniques. The analytical methods EDX, ToF-SIMS, and AES, were employed to analyse model surfaces (flat quartz slides) and subsequently applied to the nanopipette samples. The results highlight the challenges associated with working at the nanoscale, especially with insulating materials and complex geometries. Despite difficulties with both sample preparation and technique limitations, useful insights were gained regarding the strengths and weaknesses of each technique for nanopipette surface characterization.

**Conclusions**

1. **Nanopipette Sample Preparation**: The goal was to optimise sample mounting and preparation methods to minimise charging effects and enable successful SEM imaging of the nanopipettes. The best results were achieved by improving the charge dissipation of the sample through connection of the floating nanopipette tip to the carbon tape/aluminium stub with silver paste and applying a 5 nm carbon coating. However, the use of silver paste limited the ability to transfer samples between stubs. It was determined that carbon coating alone, without silver paste, was sufficient for imaging, particularly when combined with the following SEM parameters: 3 keV acceleration voltage, 30 µm aperture, and an SE InLens detector.

2. **FIB Techniques**: FIB milling was employed to access the inner channel of the nanopipette, as close to the nanopore opening as possible. Despite optimisation of the milling conditions (16 kV, 0.1 nA), attempting to mill too close to the nanopipette tip, where the channel walls are extremely thin, consistently led to deformation and beam damage. Therefore, the milling of ‘windows’ was carried out at a thicker region of the nanopipette taper, ensuring the structural integrity of the sample was maintained.

3. **Chemical Analysis of Model Samples**: To reduce the challenges associated with nanopipette samples, flat quartz slides were used as model systems for initial testing of each

characterisation technique. Water droplet contact angle measurements confirmed the successful deposition of the organosilane layer. Three chemical characterization methods were tested: EDX, ToF-SIMS, and AES.

- **EDX**: A very slight sulphur peak (2.307 keV) was observed. However, achieving this result required a low beam voltage (5 kV), a long acquisition time (1 hour), and a large scanning area (512 µm × 384 µm), highlighting that sulphur detection was at the limit of EDX's sensitivity for surface analysis.
- **ToF-SIMS**: As a highly surface-sensitive technique with in situ charge neutralization, ToF-SIMS was more effective in conclusively detecting sulphur on the organosilane-modified surface.
- **AES**: None of the tested sample preparation methods or beam conditions effectively mitigated charging or produced high-quality spectra suitable for chemical analysis of the quartz slides. While coatings and sputtering slightly improved signal quality, spectral background noise and charging effects remained significant obstacles, highlighting the many challenges of this technique and the need for further optimisation.

4. **Application to Quartz Nanopipettes**: The optimised techniques were then applied to the modified and prepared nanopipette samples to analyse the inner surface.
    - **EDX**: Initial contamination of organosilane on the carbon tape beneath the nanopipette caused a false-positive sulphur signal. After transferring the sample to a clean mount, point scans showed that the small surface area and reduced acquisition time (5 minutes, due to beam drift) were insufficient to detect the sulphur monolayer on the nanopipette surface.
    - **ToF-SIMS**: ToF-SIMS could detect $HS^-$ ions on the outer surface of the nanopipette, confirming the successful silanisation reaction. However, as the analysis moved towards the nanopipette tip and the ‘window’ exposing the inner channel, signal intensity diminished significantly. Optimisation efforts were further limited by method constraints, such as insufficient lateral resolution and the inability to accurately locate and manoeuvre the sample for further analysis. Therefore, ToF-

SIMS was considered unsuitable for this application without more complex optimisation specific to such particular samples.

- **AES**: The higher PE beam energy required for AES caused the nanopipette to melt. Owing to limited flexibility regarding optimisation of operating conditions, further work is needed to improve the conductivity of the sample.

**Future Work**

1. **Nanopipette Sample Preparation:** Further work is needed to find a preparation method that can bring the nanopipette tip into contact with a conductive substrate, ideally without the need for coating. The current technique leaves the tip unsupported and floating above the substrate. For example, a TEM copper grid with carbon layer has been used previously in the literature, to prepare nanopipette tips for TEM.[53] Shigyou *et al*. used water droplets on carbon coated TEM grids to act as a cushion, preventing the nanopipette tip from shattering when cut away from the capillary bulk and gently dropping the tip onto the grid surface. However, this method doesn't adhere the tips to the surface, meaning the necessary manoeuvring and sample tilting required for FIB wouldn't be possible. Furthermore, the nanopipette tips retained water, even after heating, which is damaging to high-vacuum analysis techniques.[53] As such, a method that can consistently adhere the nanopipette tip to a TEM grid without damage or the use of water would be necessary.

2. **FIB Milling of the Sensing Region:** To allow for milling of the sensing region, the charging effects and beam drift would need to be further minimised. As mentioned above, establishing electrical contact between the milling region and a conductive substrate remains a practical and promising approach. In addition, more specialised adaptations could be made, such as the introduction of $XeF_2$ during milling.[35] When used for nanopipette milling, $XeF_2$ was found to reduce the milled material redeposition, increase milling rate and reduce drift, when used in conjunction with a large beam current. However, the capacity to introduce additional gases to the FIB vacuum chamber is not available for all equipment and as such, the method may not be widely applicable.

3. **Chemical Analysis of Quartz Nanopipettes:** Additional techniques to minimise charging effects and increase lateral resolution are typically more involved than those previously tested, requiring greater expertise, operator time and specialised equipment. For example,

if FIB milling is sufficiently optimised, samples can be thinned prior to analysis.[54] Other work in the literature has coated the underside of thin samples with gold to improve conductivity.[50] They have also coated the entire sample with gold, then sputtered a small region for analysis with an argon beam, but this technique requires high precision to prevent sputtering of the sample surface.[55]

Nanopipettes represent a very particular challenge for any nanoprobe characterisation method. These samples are small, with nanoscale interior regions of analytical interest, made of an insulating material, mechanically very fragile, with unusual geometry and monolayer modifications. Overall, the optimisation process is an iterative process, requiring further advancement in all of the above areas in order to realise chemical analysis of sensing region interiors.

## 5.6 REFERENCES


1 T. Albrecht, *Annu. Rev. Anal. Chem.*, 2019, **12**, 371–387.

2 C. A. Morris, A. K. Friedman and L. A. Baker, *Analyst*, 2010, **135**, 2190–2202.

3 J.-L. Munoz and J. A. Coles, *J Neurosci Methods*, 1987, **22**, 57–64.

4 R. A. Levis and J. L. Rae, *Biophys J*, 1993, **65**, 1666–1677.

5 K. McKelvey, S. L. Kinnear, D. Perry, D. Momotenko and P. R. Unwin, *J Am Chem Soc*, 2014, **136**, 13735–13744.

6 Y. Yu, V. Sundaresan, S. Bandyopadhyay, Y. Zhang, M. A. Edwards, K. McKelvey, H. S. White and K. A. Willets, *ACS Nano*, 2017, **11**, 10529–10538.

7 Y. Takahashi, Y. Sasaki, T. Yoshida, K. Honda, Y. Zhou, T. Miyamoto, T. Motoo, H. Higashi, A. Shevchuk, Y. Korchev, H. Ida, R. Hanayama and T. Fukuma, *Anal Chem*, 2023, **95**, 12664–12672.

8 R.-J. Yu, Y.-L. Ying, R. Gao and Y.-T. Long, *Angewandte Chemie International Edition*, 2019, **58**, 3706–3714.

9 K. Kececi, A. Dinler and D. Kaya, *J Electrochem Soc*, 2022, **169**, 027502.

10 W. Yi, X. Li, X. He, F. Yue and T. Wang, *Journal of Electroanalytical Chemistry*, 2022, **909**, 116106.

11 Z. Wang, Y. Liu, L. Yu, Y. Li, G. Qian and S. Chang, *Analyst*, 2019, **144**, 5037–5047.

12 J. Lv, R.-C. Qian, Y.-X. Hu, S.-C. Liu, Y. Cao, Y.-J. Zheng and Y.-T. Long, *Chemical Communications*, 2016, **52**, 13909–13911.

13 F. O. Laforge, J. Carpino, S. A. Rotenberg and M. V Mirkin, *Proceedings of the National Academy of Sciences*, 2007, **104**, 11895–11900.

14 L. Ying, A. Bruckbauer, D. Zhou, J. Gorelik, A. Shevchuk, M. Lab, Y. Korchev and D. Klenerman, *Physical Chemistry Chemical Physics*, 2005, **7**, 2859–2866.

15 A. E. P. Schibel and E. N. Ervin, *Langmuir*, 2014, **30**, 11248–11256.

16 J. Feng, J. Liu, B. Wu and G. Wang, *Anal Chem*, 2010, **82**, 4520–4528.

17 G. Wang, B. Zhang, J. R. Wayment, J. M. Harris and H. S. White, *J Am Chem Soc*, 2006, **128**, 7679–7686.

18 Y. Yu, J.-M. Noël, M. V Mirkin, Y. Gao, O. Mashtalir, G. Friedman and Y. Gogotsi, *Anal Chem*, 2014, **86**, 3365–3372.

19 X. Xu, H. He and Y. Jin, *Anal Chem*, 2015, **87**, 3216–3221.

20 H. R. Rees, S. E. Anderson, E. Privman, H. H. Bau and B. J. Venton, *Anal Chem*, 2015, **87**, 3849–3855.

21 M. Michalak, M. Kurel, J. Jedraszko, D. Toczydlowska, G. Wittstock, M. Opallo and W. Nogala, *Anal Chem*, 2015, **87**, 11641–11645.

22 S. Liu, Y. Dong, W. Zhao, X. Xie, T. Ji, X. Yin, Y. Liu, Z. Liang, D. Momotenko, D. Liang, H. H. Girault and Y. Shao, *Anal Chem*, 2012, **84**, 5565–5573.

23 X. Yin, S. Zhang, Y. Dong, S. Liu, J. Gu, Y. Chen, X. Zhang, X. Zhang and Y. Shao, *Anal Chem*, 2015, **87**, 9070–9077.

24 K. J. Freedman, L. M. Otto, A. P. Ivanov, A. Barik, S.-H. Oh and J. B. Edel, *Nat Commun*, 2016, **7**, 10217.

25 P. K. Jal, S. Patel and B. K. Mishra, *Talanta*, 2004, **62**, 1005–1028.

26 M. G. Schrlau, N. J. Dun and H. H. Bau, *ACS Nano*, 2009, **3**, 563–568.

27 S. Umehara, N. Pourmand, C. D. Webb, R. W. Davis, K. Yasuda and M. Karhanek, *Nano Lett*, 2006, **6**, 2486–2492.

28 G.-C. Liu, M.-J. Gao, W. Chen, X.-Y. Hu, L.-B. Song, B. Liu and Y.-D. Zhao, *Electrochem commun*, 2018, **97**, 6–10.

29 S. Umehara, M. Karhanek, R. W. Davis and N. Pourmand, *Proceedings of the National Academy of Sciences*, 2009, **106**, 4611–4616.

30 S. Ding, C. Gao and L.-Q. Gu, *Anal Chem*, 2009, **81**, 6649–6655.

31 P. Actis, A. Rogers, J. Nivala, B. Vilozny, R. A. Seger, O. Jejelowo and N. Pourmand, *Biosens Bioelectron*, 2011, **26**, 4503–4507.

32 E. A. Vitol, Z. Orynbayeva, M. J. Bouchard, J. Azizkhan-Clifford, G. Friedman and Y. Gogotsi, *ACS Nano*, 2009, **3**, 3529–3536.

33 R. Pan, M. Xu, J. D. Burgess, D. Jiang and H.-Y. Chen, *Proceedings of the National Academy of Sciences*, 2018, **115**, 4087–4092.

34 R. Gao, Y.-L. Ying, Y.-J. Li, Y.-X. Hu, R.-J. Yu, Y. Lin and Y.-T. Long, *Angewandte Chemie International Edition*, 2018, **57**, 1011–1015.

35 C. G. Gunderson, S. T. Barlow and B. Zhang, *Journal of Electroanalytical Chemistry*, 2019, **833**, 181–188.

36 R. Chen, K. Hu, Y. Yu, M. V Mirkin and S. Amemiya, *J Electrochem Soc*, 2016, **163**, H3032.

37 R. Hao and B. Zhang, *Anal Chem*, 2016, **88**, 614–620.

38 R. F. Egerton, P. Li and M. Malac, *Micron*, 2004, **35**, 399–409.

39 D. C. Joy and C. S. Joy, *Micron*, 1996, **27**, 247–263.

40 G. Strugaj, A. Herrmann and E. Rädlein, *J Non Cryst Solids*, 2021, **572**, 121083.

41 J. M. Fontaine, J. P. Duraud and C. Le Gressus, *Surface and Interface Analysis*, 1979, **1**, 196–203.

42 W. E. S. Unger, T. Wirth and V.-D. Hodoroaba, in *Characterization of Nanoparticles*, eds. V.-D. Hodoroaba, W. E. S. Unger and A. G. Shard, Elsevier, 2020, pp. 373–395.

43 M. Senoner, A. Maaßdorf, H. Rooch, W. Österle, M. Malcher, M. Schmidt, F. Kollmer, D. Paul, V.-D. Hodoroaba, S. Rades and W. E. S. Unger, *Anal Bioanal Chem*, 2015, **407**, 3211–3217.

44 C. G. PANTANO, D. B. DOVE and G. Y. ONODA, in *Glass Surfaces*, ed. D. E. DAY, Elsevier, 1975, pp. 41–53.

45 A. Rossi, B. Elsener, G. Hähner, M. Textor and N. D. Spencer, *Surface and Interface Analysis*, 2000, **29**, 460–467.

46 B. Hagenhoff, *Microchimica Acta*, 2000, **132**, 259–271.

47 S. Zhang, M. Li, B. Su and Y. Shao, *Annu. Rev. Anal. Chem.*, 2018, **11**, 265-286.

48 Y. Wang, D. Wang and M. V. Mirkin, *Proc. R.Soc. A*, 2017, **473**, 2199.

49 R. F. Egerton, *Physical principles of electron microscopy: An introduction to TEM, SEM, and AEM*, Springer US, 2005.

50 D. R. Baer, A. S. Lea, J. D. Geller, J. S. Hammond, L. Kover, C. J. Powell, M. P. Seah, M. Suzuki, J. F. Watts and J. Wolstenholme, *J Electron Spectros Relat Phenomena*, 2010, **176**, 80–94.

51 C. A. Schneider, W. S. Rasband and K. W. Eliceiri, *Nat Methods*, 2012, **9**, 671–675.

52 D. Duleba, S. Denuga and R. P. Johnson, *Phys. Chem. Chem. Phys.*, 2024, **26**, 15452–15460.

53 K. Shigyou, L. Sun, R. Yajima, S. Takigaura, M. Tajima, H. Furusho, Y. Kikuchi, K. Miyazawa, T. Fukuma, A. Taoka, T. Ando and S. Watanabe, *Anal Chem*, 2020, **92**, 15388–15393.

54 M. Sato, S. Shirai, Y. Seyama and T. Itakura, *Analysis of Insulating Materials and Deep Interfaces by Auger Electron Spectroscopy*, 2010, vol. 46.

55 C. Carrière, F. Mercier, M. Bouttemy, E. Foy, X. Crozes, A. Etcheberry, D. Neff, I. Monnet and P. Dillmann, *J Electron Spectros Relat Phenomena*, 2019, **235**, 51–59.

# 6 CONCLUSIONS AND OUTLOOK

## CONTENTS

This thesis aimed to progress work towards developing a multiplexed assay diagnosis technique, utilising nanopore sensing, periodontitis biomarkers, DNA carriers, and nanopipettes. The objectives to do this broadly covered: noise reduction of nanopore sensing equipment, identification of suitable biomarkers for the sensing technique and development of antibody-DNA probe structures, high-bandwidth measurements of linear DNA translocation and full dataset characterisation, and finally, developing and testing sample preparation and analytical methods for the morphological and chemical characterisation of the inner surface of nanopipettes. Each of these objectives will be discussed in more detail below.

## 6.1 Noise Optimisation of Nanopore Sensing Equipment

The results of this work demonstrated an 83% reduction in baseline noise when making a number of changes to the sensing set-up, and this marked reduction in noise was seen when increasing the bandwidth from 10 kHz to 100 kHz. The following factors were investigated: filtering the mains power source, swapping an active for a passive filter, replacing mains powered equipment with battery-powered equipment, testing different grounding sources, and comparing different data transmission cables.

The noise contribution from the mains power was determined to be the largest and most detrimental source of noise, so the investigated factors pertaining to filtering and avoiding mains power where possible had the most beneficial effect. In particular, filtering the mains power source to all equipment with the use of a filtered extension lead was a simple but effective solution. Whilst removing all mains-powered equipment or mains power sources and replacing with battery equivalents was effective, in the long-term it was not a practical solution. A compromise had to be made between noise performance and feasible experimental run-times.

Studies in the literature increasingly focus on more technical solutions to reduce noise contributions, such as highly optimised nanopore substrates with modifications,[1–3] optimising precision methods of production[2,4,5] and developing bespoke electronic equipment.[6,7] Whilst these techniques are effective, they require high levels of expertise, time and cost. By contrast, the optimisation work undertaken in this thesis was much simpler, largely relying on off-the-shelf products to replace equipment that is mostly used in the field as standard practice. Often perceived as inevitable sources of noise, this work demonstrated significant reductions in

baseline noise without the need for costly, specialized modifications. Here, it has been demonstrated that other commercially available alternatives can have a large impact on noise reduction, such as swapping an active low-pass filter for a passive filter or replacing the data transmission cable with a higher-quality, better performing alternative.

However, noise optimisation is an iterative/cumulative process, and more work needs to be done to allow for further increases in measurement bandwidth. For example, focussing on optimisation of the liquid sample cell to reduce baseline noise further would be the next step in this 'simple' approach. Reducing the volume of our liquid sample cell from a 2 mL electrolyte reservoir down to a microfluidic device could offer further improvement in performance.

In summary, the aim of this work was achieved with a relatively straightforward approach, and these findings could be easily and cheaply applied to other experimental set-ups. However, it must be noted that, to approach bandwidth measurements approaching 1 MHz, the aforementioned technical solutions and nanopore modifications are typically necessary, in order to address capacitance and dielectric noise.

## 6.2 Developing a DNA-Antibody Conjugate with the SCoNE DNA Assembly Method

This work first determined which antibody-protein pair, from a shortlist of periodontitis biomarkers, was most suitable for the intended application of nanopore sensing. Due to a range of considerations, HGF was found to be most suitable for initial further study. The impact of antibody conjugation to DNA on the dissociation constant was then investigated, and the impact found to be small and not detrimental for further use. Furthermore, the impact of SCoNE DNA assembly conditions were tested on antibody stock solutions, to determine if optimisation of the assembly process was required. Although the conditions tested did have a negative impact, it was deemed acceptable for further testing. A 3 kbp DNA construct containing two HGF antibodies was built with the unmodified SCoNE DNA assembly method, and the expected size of the structure was confirmed with gel electrophoresis. Finally, attempts were made to isolate the antibody-DNA structure, with none of the methods tested (ethanol extraction, adapted PCR clean-up, molecular weight cut-off filters, streptavidin beads) able to isolate the structure and maintain antibody functionality.

Typical antibody-conjugation studies report the experimental yield as determined by HPLC, and don't report changes in the dissociation constant.[8] As such, studies in literature provide useful benchmarks for conjugation reaction yields, but not conjugated antibody performance. Furthermore, antibody conjugation relies on exposed and easily accessible free amines in the antibody structure of which there are many such sites, some of which are more susceptible to hydrolysis than others. Therefore, there was a possibility that antibody conjugation could result in binding at the sensing region and negatively impact binding ability. In this study, it was found that the dissociation constant of a conjugated antibody increased from 78.2 ± 5.6 pM to 97.6 ± 1.2 pM, indicating a slight decrease in binding ability. This demonstrates that potential antibody denaturation, if due to a small percentage of conjugation reactions occurring at binding sites, is not significantly detrimental to the binding ability.

The aim of this study was to demonstrate the feasibility of an antibody-DNA probe carrier for nanopore sensing applications, specifically for periodontitis biomarker detection. Unfortunately, several challenges arose that prevented the work from progressing to fully complete this aim. Most detrimentally, antibody functionality was not able to be maintained after the full SCoNE DNA assembly procedure.

It is possible that SCoNE DNA assembly is not a suitable method for incorporating antibodies on a DNA structure. When compared to other commonly used methods, such as DNA self-assembly and enzymatic modification, SCoNE is unique in that it offers the ability to incorporate different probes onto the same DNA strand to allow for multiplexed assay, something not possible with the other techniques. However, it does this by first reacting the DNA fragments with the probe before undergoing DNA assembly. The other techniques first assemble the DNA strand or conjugate linkers to the DNA strand before reacting with the probe, which is why these techniques are limited to one target analyte per DNA strand. This distinction likely explains the success of these alternative methods in incorporating antibodies, as they avoid exposing the antibodies to harsh conditions such as elevated temperatures or enzymatic digestion. In contrast, SCoNE DNA assembly inherently requires such conditions, as the probes (aptamers or antibodies) sterically block digestion enzymes during the final assembly step. This mechanism ensures the synthesis of the complete DNA construct, as confirmed by gel electrophoresis, but may compromise antibody functionality.

On the other hand, it may be that functionality was lost during attempts to isolate the structure. To fully test this and determine whether the SCoNE method is compatible with antibody probes, an aliquot of antibody stock would need to be subjected to Gibson Assembly MasterMix (GAMM) enzymes, and an ELISA performed to determine if any binding ability of the antibodies remained. If there was no ELISA signal, then it would confirm that the GAMM enzymes denature the antibodies, and alternative target probes would need to be explored. If, however, there is an ELISA signal, this would prove that it is the isolation methods that are detrimental, and other techniques proven to be suitable in the literature, such as HPLC, would need to be tested.

Overall, progress was made in identifying periodontitis biomarkers suitable for nanopore sensing and furthering studies of antibody conjugation. However, some challenges were highlighted, and work remains to be done to develop a diagnostic technique utilising a one-strand DNA multiplexed assay.

## 6.3 Characterisation of DNA Translocation as a Reference for Complex Analytes

In this chapter, 4 kbp linear dsDNA translocation was studied, in order to fully characterise results obtained with the optimised experimental set-up at 100 kHz recording bandwidth. It was found that, although SNR was quite low compared to other results reported in the literature,[1,6,9] the data showed temporally distinct noise and translocation event clusters that could be separated with simple clustering algorithms. Translocation characteristics, such as average current blockade, average dwell time and translocation frequency, were determined and evaluated against the literature and existing theoretical models. Subevent analysis also shows that, at higher bandwidth and a low measured SNR, the background noise is not detrimental, and no false positive subevents are detected.

This dataset provides a good example of translocation of linear DNA in an unmodified quartz nanopipette at high salt concentration, intended as a benchmark for equipment performance and translocation experiments at high bandwidth. It also serves as a baseline and a reference point when analysing translocation data of more complex analytes (DNA carriers) of comparable length. Overall, this aligns with the overarching aim of this thesis by laying the groundwork for

reliable analysis of designed DNA-carrier structures, which are essential for multiplexed diagnostic applications.

The aim of this work was to establish a high-quality reference dataset to aid in future work and data analysis, but also to test the current data analysis methods/workflow used within the group and their suitability for intended applications. This study demonstrated the ability of our analysis algorithms to effectively differentiate event clusters and produce expected subevent analyses at high bandwidths. However, future efforts should focus on further improving data analysis for DNA-carrier translocation, where the added molecular complexity can give unexpected translocation results.

## 6.4 Nanopipette Sample Preparation and Chemical Analysis

A successful sample preparation method was developed to enable high-resolution SEM imaging of quartz nanopipettes. Additionally, focused ion beam (FIB) milling of the nanopipette taper was achieved at the submicron scale, creating 'windows' in the nanopipette wall that exposed the inner surface of the channel. As a model system, quartz slides were chemically modified with a thiol-terminated organosilane monolayer, and the suitability of analytical techniques, including energy-dispersive X-ray spectroscopy (EDX) with SEM, time-of-flight secondary ion mass spectrometry (ToF-SIMS), and Auger electron spectroscopy (AES), for monolayer detection on an insulating substrate was investigated. Findings from these studies are summarized in Table 6.1.

These techniques were subsequently applied to chemically modified nanopipettes, with the results summarised in Table 6.2. Under the conditions tested, none of the techniques proved suitable for detecting monolayer modification of quartz nanopipettes on their inner surface.

| Method | Sample Preparation | Experimental Conditions | Findings |
|---|---|---|---|
| SEM/EDX | Plasma cleaning, silanisation | 5 kV | Sulphur signal at the limit of detection |
| ToF-SIMS | Plasma cleaning, silanisation | Additional charge neutralisation | Sulphur monolayer signal detected |
| AES | Plasma cleaning, silanisation; Steel grid, Cu tape, Pt coating, C coating, | 5 kV, 1 nA<br>10 kV, 10 nA<br>Ar sputtering | No combination of preparation or beam conditions yielded usable data due to charging effects |

*Table 6.1: Summary of results from chemical characterisation of silane-modified quartz slides, detailing method, sample preparation and experimental conditions tested.*

This work demonstrates progress in developing a sample preparation method suitable for sub-20 nm SEM imaging of nanopipette pores, a resolution rarely achieved in comparable studies with nanopipette samples.[10,11] The preparation method also enabled FIB milling to expose the nanopipette's inner surface while preserving structural integrity, advancing the application of FIB milling over prior studies, which have primarily focused on nanopipettes modified with conductive coatings, such as carbon or gold, for use as nanoelectrodes.[10] Although the samples required conductive outer coatings, the inner surface remained free from contamination.

However, it was not possible to mill directly adjacent to the nanopore in the sensing region; the challenge of preventing beam damage at this region remains unsolved. To overcome this, further optimisation of the sample preparation method is necessary. For example, bringing the floating nanopipette tip into contact with a conductive substrate could mitigate sample damage from charging, but may pose additional challenges due to sample fragility.

| Method | Sample Preparation | Experimental Conditions | Findings |
|---|---|---|---|
| EDX | Silanisation,<br>C coating,<br>FIB milling;<br>C substrate,<br>Cu substrate | 5 kV | Sulphur detected from contamination of the C substrate; sulphur monolayer on nanopipette below detection limit |
| ToF-SIMS | Silanisation,<br>C coating,<br>FIB milling | Additional charge neutralisation | Sample surface area too small; no signal detected |
| AES | Silanisation,<br>C coating,<br>FIB milling | 5 kV, 1 nA<br>10 kV, 10 nA | Sample deformation observed; sulphur signal not detected |

*Table 6.2: Summary of results from chemical characterisation of silane modified quartz nanopipettes, detailing method, sample preparation and experimental conditions tested.*

The analytical techniques SEM/EDX and ToF-SIMS were concluded as unsuitable for this application. For EDX, the depth resolution was too poor to detect a monolayer, particularly on such small, insulating samples. For ToF-SIMS, the lateral resolution was insufficient; when approaching sample analysis regions below a certain size threshold, the signal was lost entirely. AES, despite consistently poor results due to charging effects, showed the greatest potential due to its nanometre-scale lateral and depth resolution, which are critical for analysing the nanopipette's inner sensing region. However, persistent technical challenges with the AES equipment, resulting in frequent downtime, limited the scope of testing and development of suitable sample preparation techniques.

The objective of characterising the inner surface of a quartz nanopipette was not fully achieved, as the insulating nature of quartz, the nano-scale dimensions of the region of interest, and the fragility of the samples presented significant challenges to electron-beam probe techniques. This work highlighted potential areas for further work; in particular sample preparation remains a technical challenge that needs to be addressed. Increasing the electrical contact of the floating nanopipette tip, without causing damage to the sensing region, is essential for further progress.

AES has the most potential for successful chemical characterisation of the nanopipette sensing region but must be combined with an optimised preparation method.

## 6.5 PROJECT PROGRESSION AND BROADER APPLICABILITY

This work has advanced the overarching project by addressing some fundamental challenges in nanopore sensing, DNA carrier engineering, and nanopipette morphological-chemical characterisation. The effectiveness of the straightforward noise reduction strategies investigated here highlights how relatively simple adjustments can yield substantial improvements in background noise. This simple approach provides a pragmatic alternative to more technical solutions.

Due to current synthesis limitations, the potential for multiplexing antibody-DNA carriers remains unproven. However, the work presented in this thesis has identified avenues of future work. For example, alternative probe molecules may need to be considered to realise multiplexed assay with one DNA strand. In addition, translocation experiments of DNA-carriers would be necessary for further validation of current data processing methods. Finally, integrating new techniques, such as machine learning algorithms, could allow for improved event-classifications.

For nanopipette characterisation, the groundwork has been laid for sample preparation and high-resolution SEM imaging. However, for characterisation of the inner surface, further improvements to sample preparation and sample mounting are required. Achieving chemical characterisation of monolayer modifications to nanopipettes would open up avenues of further research. For example, fundamental research is required to understand transport properties in nanopipettes, with implications for diagnostic applications.

In terms of research, there is still a way to go in order to achieve a rapid, multiplexed diagnostic technique. This work establishes a solid foundation for some of the key techniques and methods that underlie the project as a whole, with suggested focusses for further development identified. These findings are not just specific to periodontitis biomarker detection, but also have a broader relevance amongst other diagnostic applications, nanopore sensing techniques and advanced chemical analysis applications.

## 6.6 REFERENCES


1 L. J. Steinbock, R. D. Bulushev, S. Krishnan, C. Raillon and A. Radenovic, *ACS Nano*, 2013, **7**, 11255–11262.

2 P. Chen, T. Mitsui, D. B. Farmer, J. Golovchenko, R. G. Gordon and D. Branton, *Nano Lett*, 2004, **4**, 1333–1337.

3 P. Waduge, I. Bilgin, J. Larkin, R. Y. Henley, K. Goodfellow, A. C. Graham, D. C. Bell, N. Vamivakas, S. Kar and M. Wanunu, *ACS Nano*, 2015, **9**, 7352–7359.

4 L. J. de Vreede, C. Ying, J. Houghtaling, J. Figueiredo Da Silva, A. R. Hall, A. Lovera and M. Mayer, *Nanotechnology*, 2019, **30**, 265301.

5 J. K. Rosenstein, M. Wanunu, C. A. Merchant, M. Drndic and K. L. Shepard, *Nat Methods*, 2012, **9**, 487–492.

6 Z. Gu, H. Wang, Y.-L. Ying and Y.-T. Long, *Sci Bull (Beijing)*, 2017, **62**, 1245–1250.

7 J. K. Rosenstein, M. Wanunu, C. A. Merchant, M. Drndic and K. L. Shepard, *Nat Methods*, 2012, **9**, 487–492.

8 D. Shrestha, A. Bagosi, J. Szöllősi and A. Jenei, *Anal Bioanal Chem*, 2012, **404**, 1449–1463.

9 V. Tabard-Cossa, D. Trivedi, M. Wiggin, N. N. Jetha and A. Marziali, *Nanotechnology*, 2007, **18**, 305505.

10 C. G. Gunderson, S. T. Barlow and B. Zhang, *Journal of Electroanalytical Chemistry*, 2019, **833**, 181–188.

11 S. Zhang, M. Li, B. Su and Y. Shao, *Annu. Rev. Anal. Chem.*, 2018, **11**, 265-286.